

Compact Gamma-ray Sources Based on Laser- Plasma Wakefield Accelerator

By Silvia Cipiccia

A thesis presented for the partial fulfilment of the requirements for the degree
of Doctor in Philosophy

Department of Physics
University of Strathclyde
John Anderson Building
107 Rottenrow
G4 0NG

Supervisor: Prof. D. A. Jaroszynski

November 2011

'This thesis is the result of the author's original research. It has been composed by the author and has not been previously submitted for examination which has led to the award of a degree.'

'The copyright of this thesis belongs to the author under the terms of the United Kingdom Copyright Acts as qualified by University of Strathclyde Regulation 3.50. Due acknowledgement must always be made of the use of any material contained in, or derived from, this thesis.'

Signed:

Date:

Abstract

Laser-plasma wakefield accelerator (LWFA) is a promising novel technology that is introducing miniaturization to the accelerator world: the unprecedented gradient of acceleration shrinks the accelerator down to table-top size. Moreover, the LWFA comes with an embedded light source: electrons, while accelerating, undergo betatron oscillatory motion that results in synchrotron radiation emitted in a narrow cone along the direction of propagation. In this thesis we study theoretically and we prove experimentally a new regime of betatron oscillation that occurs when electrons experience the electromagnetic field of the laser during acceleration and oscillate resonantly at the laser frequency or its sub-harmonics. The signature of the harmonically resonant betatron (HRB) regime is a large oscillation amplitude and consequently prolific emission of high energy photons up to the MeV range. The HRB source has unique properties: very short pulse length (~ 10 fs), small source size (few microns), high peak brightness of the order of 10^{23} photons/s mm² mrad² 0.1% B.W., which is comparable with a third generation light source. These properties make the source particularly appealing for the life sciences and medical and security applications. As a part of a future applications project, we give the scaling of the photon energy as a function of laser intensity and plasma density, which could extend toward tens of MeV.

The thesis also investigates another gamma-ray source that utilises beams from the LWFA: bremsstrahlung radiation from high energy electrons interacting with metal targets. We study the electron beam and target parameters to optimize the emission

process and the gamma-ray beam properties to match potential application requirements, such as radioisotope generation via photonuclear process. The results of a proof of concept experiment are presented and compared with simulations.

Finally, we investigate numerically the possibility of generating a converging gamma-ray beam based on the bremsstrahlung process. The results are encouraging, and the potential impact of a compact converging gamma-ray beam source is discussed with particular attention to medical applications in cancer treatment.

Acknowledgements

This thesis would not have happened without the help, support and work of lots of people. Particular thanks goes to my supervisor Prof. Dino Jaroszynski, for the support, suggestions and incentive. Thanks to the whole ALPHA-X group and in particular to Mark Wiggins, Constantin Aniculaesei, Grace Manahan, Gregory Vieux, Xue Yang, David Grant, Anna Subiel, Enrico Brunetti who shared with me the hard but also cheerful times. A particular thanks also to Gregor Welsh and Riju Issac for their help and patience during hard days in the lab, to Ranaul Islam and Bernard Ersfeld for their theoretical advice and to David Clark and Tom McCanny for their technical support. Thanks to the RAL staff who helped us during the experiments and provided the laser pulses we asked for. Thanks also to the people from Instituto Superior Técnico, Glasgow University and Oxford University who worked with us during the experimental runs.

And on a personal level I would like to thank John for these intense four years of exchange of sagacious and hilarious ideas, Marcello, even though far away, to be always present. I would like to deeply thank MP with whom I shared a flat and office, and the many long jazz nights we spent in the Beer Café speculating about the future. And thanks to Sergio who makes me laugh and encourages me also when I am tired and grumpy.

Finally thanks to my Mum, my Dad and my sisters for always supporting me.

The role of the author

Experiments on high power laser systems necessarily involve a large team of people. This section outlines the role of the author in the work presented in this thesis. In Chapter 2 the theoretical analytical work was done by Prof. Dino Jaroszynski and Bernard Ersfeld. Osiris PIC simulations were performed by Ranaul Islam. The data presented in Chapter 3 and Chapter 4 were the results of two experimental campaigns on the Astra Gemini laser PW laser. The author was involved in the planning and setup and running of both experiments. The author was responsible of the x- and gamma-ray and electron diagnostics including calibration, alignment, data acquisition and all the analysis. For the experiment described in Chapter 3 the capillary used as accelerator was laser micro-machined by Mark Wiggins. Gregory Vieux was the major expert in running the capillary as a LWFA. The Compton side scattering configuration was developed by the author from an initial idea by David Hamilton. Timepix detector was calibrated in collaboration with Dzmitry Maneuski. In Chapter 4 the capillary accelerator was run by Nicolas Bourgeois and Tom Ibbotson. The initial idea of converging gamma-ray beam has been formulated by Riju Issac, Prof. Dino Jaroszynski and the author. The GEANT4 simulations modelling for both experiments and the detectors were performed by the author. Technical support during the experiment was provided by the staff at RAL, and David Clark and Tom McCanny at Strathclyde.

Contents

Chapter 1	15
1.1 The X-ray: a Powerful Versatile Tool in Science and Everyday Life	15
1.2 Discovery of Synchrotron Radiation.....	17
1.3 Overview: Past, Present and Future Generations of Light Sources	18
1.4 Novel Concept of Light Source: Laser-Wakefield Driven Light Sources	24
Chapter 2	37
2.1 Introduction.....	37
2.2 Laser-Plasma Wakefield Accelerators	39
2.2.1 LPWA Basic Concepts.....	41
2.2.2 Guiding of High-Intensity Laser Pulses	45
2.2.3 Laser Plasma Accelerator Configurations.....	47
2.3 Laser-Plasma Wakefield Acceleration.....	50
2.3.1 Theory of the LWFA.....	50
2.3.2 Wave-Breaking	52
2.4 The Bubble Regime.....	54
2.4.1 The Broken-Wave Regime.....	54
2.4.2 Electron Injection	57
2.4.3 Electron Acceleration in the Bubble Regime.....	59
2.4.4 Beam loading	60
2.5 Betatron Oscillations.....	62
2.6 Harmonically Resonant Betatron Motion	69
2.7 Conclusions	74
Chapter 3	81
3.1 Introduction.....	81
3.2 Broadband high flux single shot measurements of betatron radiation	83
3.2.1 Compton Scattering.....	84
3.2.2 A Pixel Matrix Semiconductor as an X-ray Spectrometer.....	88
3.2.3 Medipix and Timepix.....	89

3.3	Experimental Setup	99
3.3.1	Highly Damped Regime.....	101
3.3.2	Weakly and Strongly Resonant Regime	103
3.3.3	Phase Contrast Experiment	106
3.4	Conclusion	111
Chapter 4	117
4.1	Introduction.....	117
4.2	Bremsstrahlung Radiation Overview	119
4.3	Laser-Plasma Wakefield Accelerator Driven Bremsstrahlung Source	123
4.4	Laser-Plasma Wakefield Accelerator Bremsstrahlung Source: Scaling	126
4.5	Experimental Setup	131
4.6	Scaling for Potential Applications: Radioisotope Production.....	137
4.7	Towards a Converging Gamma-Ray Beam	139
4.8	Converging Gamma-Ray Beam and Radiosurgery: a Possible Application..	149
4.8.1	Overview of Radiosurgery Techniques.....	152
4.9	The Converging Gamma-Ray Beam as a Novel Generation of Gamma-Knife	155
4.10	Conclusions.....	160
Chapter 5	165
5.1	Discussion of Synchrotron Radiation from Betatron Oscillation of LWFA	
	Electrons.....	165
5.2	Next Challenges for HBR Sources.....	168
5.3	Summary of Bremsstrahlung Radiation Produced by LWFA Electrons	171
5.4	Understanding the Potential Market and Impact.....	172
Appendix:	177
	Osiris:	177
	Geant4:	178

List of Figures

Figure 1-1: The first radiograph: the hand of Bertha Roentgen [4].	17
Figure 1-2: Comparison between a) dipole magnet, b) wiggler and c) undulators design. The horizontal emission angle is reduced by a factor $N^{1/2}$ (N is number of periods) for undulators. Images modified from Ref. [4]).	20
Figure 1-3: Peak brightness for third generation and fourth generation light sources, from Ref. [4].	23
Figure 1-4: Peak brightness vs pulse duration for past and future synchrotron light sources. Image from Ref. [18]	23
Figure 1-5: 4 cm long laser-plasma accelerator (at Strathclyde) equivalent to a 30 m long conventional accelerator.	26
Figure 1-6: Nature cover of the issue of 2004 where three letters on first observation of high quality electron beams were published [22-24].	27
Figure 2-1: Schematic of the LWFA mechanism: the ponderomotive force of the laser excites plasma waves and electrons surfing the wave are accelerated.	45
Figure 2-2: Bubble picture obtained from OSIRIS [41] simulation showing the three different density regions that identify the bubble: the ion cavity behind the laser pulse, the high density electron sheath and the trapped electrons forming a stem.	55
Figure 2-3: Evolution of the electron trajectory (l.h.s.) and of the electron Lorentz factor (r.h.s.) in the bubble regime as calculated analytically assuming a spherical bubble and a plasma density of $2 \times 10^{18} \text{ cm}^{-3}$. The oscillation amplitude (see l.h.s.) evolves as $\gamma^{1/4}$ as expected from (2.52).	68
Figure 2-4: OSIRIS simulations of laser-driven betatron oscillations: l.h.s.: a) snapshot of electron distribution, and electron beam trajectories for the non resonant (b), weakly resonant (c) and strongly resonant case (c). R.h.s.: trajectories of one electron showing (e) evolution of γ , (f) a_β , (g) r_β , and (h) frequencies	72
Figure 3-1: Compton scattering scheme.	85

Figure 3-2: a) Compton side scattered photon energy plotted as a function of the energy of the incoming radiation, for different incident angles: $\pi/4$ (blue line), $\pi/2$ (red line), $3\pi/4$ (green line). The inset graph shows a zoom up to 300 keV. b) angular cross section vs angle for different incoming photon energies: 1 keV (black line), 100 keV (red line), 200 keV (blue line), 400 keV (green line) 800 keV (grey line), 1000 keV (pink line).87

Figure 3-3: Schematic diagram of a Medipix pixel. The detector material, in this case silicon, is connected by a solder bump-bond to the underlying electronic chip pad. In this scheme the incoming photon interacts with the semiconductor layer via photoelectric effect generating a photo-electron which in turn deposits energy in the form of electron-hole pairs.90

Figure 3-4: Laboratory source Am-241 spectrum and k-alpha from copper (Cu) recorded with the 300 μm Si Timepix detector.....93

Figure 3-5: a) Laboratory source Cs-137, Na-22 and Co-60 spectra recorded with the 300 μm Si Timepix detector. b) GEANT4 simulation results obtained for the simple monolayer model under Co-60 and Na-22 irradiation. For the Co-60, the results are obtained by summing the contribution from two different photon energies, 1332 keV and 1172 keV to reproduce the double emission line of the source.94

Figure 3-6:a) Simulated signal shape dependence on the atomic number of the material. For increasing Z a bump at 200 keV appears. The inset shows the signal contribution from the back layer. The simulations have been carried out for 1300 keV photons and a 100 μm thick back layer. b) Signal shape dependence on the thickness of the back layer (1300 keV photon energy and Z = 100). c) Signal shape dependence on the energy of the incoming radiation (100 μm thickness and Z = 100). d) Experimental spectra (dots) for Co-60 and Ni-22 reproduced from Figure 3-5a and best-fit GEANT4 simulations results (solid lines) obtained from modelling the detector with 100 μm back layer thickness and Z = 100.97

Figure 3-7: Experimental setup: A F/16 spherical mirror focuses the laser pulse (5 J, 55 ± 5 fs, 800 nm) to a 40 ± 5 μm diameter spot at the entrance of 4 cm long, 300 μm

diameter, pre-formed plasma capillary waveguide [20] with an on-axis density of $n_p \approx 2 \times 10^{18} \text{ cm}^{-3}$. The laser beam initially has an intensity of $9 \times 10^{18} \text{ Wcm}^{-2}$ that corresponds to $a_0 = 2$ and bubble radius $R = 10 \text{ }\mu\text{m}$. A $600 \text{ }\mu\text{m}$ thick Al foil blocks laser light from x-ray detectors. At the end of the interaction chamber Lanex 1 and image plate 1 is used to detect the electron beam deflected by the bending magnet. The energy resolution of the electron spectrometer estimated with the code General Particle Tracer [21] is $\sim 2\%$. On the r.h.s.: the x-ray detectors; image plate 2 placed on axis and the CdTe detector screened behind lead bricks to measure the radiation side-scattered by the aluminium post via the Compton effect. 100

Figure 3-8: X-ray beam and electrons spectrum recorded using an image plate at the end of the vacuum chamber. a) X-ray image as transmitted through metallic filters (0.3 (top left) and 1 mm (bottom left) tungsten foil, 0.5 (top right) and 1 mm (bottom right) copper foil). Calibrated filter attenuation gives a spectral peak at 20 keV (critical energy of $60 \pm 15 \text{ keV}$). b) X-ray beam profile with a divergence of 14 mrad measured simultaneously with $700 \pm 10 \text{ MeV}$ electron beam shown in c)..... 103

Figure 3-9: Two of the single shot x-ray spectra, from 90° Compton side scattered radiation from a 12 mm Al rod measured with a CdTe semiconductor detector, are overlapped with the predicted synchrotron spectra corresponding to the measured critical photon energies. l.h.s: a spectrum peaking at 50 keV, corresponding to a critical energy of 150 keV, identifies the weakly resonant case II. r.h.s. a spectrum peaking at 150 keV, corresponding to a critical energy of 450 keV, identifies as the strongly resonant case III. During the experiment we recorded in total ~ 20 single shot spectra corresponding to the harmonically resonant regime. The measured electron energy is $633 \pm 70 \text{ MeV}$ for both cases. The energy has been estimated from the average over the previous 10 electron spectra being the lanex removed during the single shot x-ray measurement. The uncertainty on the measure is given by the r.m.s. 105

Figure 3-10: Phase contrast imaging simplified scheme. 107

Figure 3-11: a) Phase contrast image recorded on an image-plate placed close to the bunker wall, showing four copper wires of 100, 75, 50 and $40 \text{ }\mu\text{m}$ thickness respectively from left to right. Lineout b) is image profiles where the faint shadow of a fifth $25 \text{ }\mu\text{m}$

thick wire is barely visible at position 3 cm. From calculations the expected attenuation without refraction would give a signal about the 70% weaker. 109

Figure 3-12: Plots of the shadows cast by the wires (solid squares) compared with data fits (solid lines) consistent with a 15 μm diameter x-ray source size for 40 (a), 50 (b), 75 (c) and 100 μm (d). The calculations have been done assuming an x-ray spectrum distributed over 10 to 100 keV, corresponding to the weakly resonant case. The error bars are given by the standard deviation of the background obtained in the region of the IP alongside the image. 110

Figure 4-1: The graph shows the dependence of the bremsstrahlung cross section integrated over emission angle on photon and electron energy. k is the energy of the emitted bremsstrahlung photon, Z is the atomic number of the target material. The graph refers to platinum with $Z = 78$ and the calculations have been performed using formula 3BS(e) in Ref. [5]. 122

Figure 4-2: The graph shows the relative intensity of the emitted photons depending on the reduced photon angle ($E_0 \cdot \vartheta$) with E_0 the initial electron energy and ϑ the observation angle. The calculations have been performed for $Z = 78$ using formula 2BS in Ref. [5]. 122

Figure 4-3: Scaling of the photon efficiency with (a) target material Z for thickness 0.5 mm and (b) target thickness (Al target). The green points represent the efficiency for all photons and the red points that for photons > 1 MeV. The efficiency is independent of the electron energy (> 100 MeV), divergence and electron source-target distance. 128

Figure 4-4. Scaling of the photon source size with (a) electron beam divergence for source-target distance = 5 cm and, (b) electron source-target distance for a e-beam divergence = 1 mrad. The photon source size was independent of the electron energy, target material Z and thickness. 128

Figure 4-5. Scaling of the photon divergence with (a) electron energy for a 0.5 mm thick Cu target placed 5 cm from the electron source, (b) target material Z for a 250 MeV electron beam, 0.5 mm thick target placed 5 cm from the source and, (c) target thickness, for a target placed at 1 m from the source for 250 a MeV electron beam with a 1 mrad

divergence. The divergence of the γ -ray beam is independent of the electron divergence and electron source-target distance.	129
Figure 4-6. Scaling of the photon pulse length with target thickness for aluminium (black points), copper (red points) and Tungsten (green points). The pulse length dependence on the target thickness varies strongly with Z, which determines the integrated length and evolution of the electron path.....	130
Figure 4-7: (a) Experimental setup and (b) typical electron energy spectrum with a central energy of 330 MeV, measured r.m.s. relative energy spread of 20% and charge of 14 pC.	132
Figure 4-8: (a) Imaging plate image (lower) and corresponding transverse profile (upper). The electron beam is the bright region on the left hand side and the gamma-ray beam produced by the electrons going through the Al and steel target is the bright region on-axis. The experimental profile (red curve) overlaps with the expected profile obtained from GEANT4 simulations (black points) for a 220 MeV electron beam. The centre of the image shows the shadow of the aperture of the main vacuum chamber of the electron spectrometer, (b) calculated energy spectrum of the bremsstrahlung radiation. The green box on the bottom of (a) marks the edges of a 5 cm thick lead brick placed in front of the image plate.	134
Figure 4-9: Bremsstrahlung beam profile imaged within the lead shadow. The radiation is transmitted through 5 cm of lead and recorded on the image plate. The bottom of the figure is a magnification of Figure 4-8a. The green box marks the corresponding area in Figure 4-8a.	135
Figure 4-10: Example of the active area screen shot of the Timepix x-ray detector upon irradiation with bremsstrahlung photons. The number of detected counts for this shot is 768.....	137
Figure 4-11: Simplified scheme to set-up to produce a converging gamma-ray beam.	140
Figure 4-12: Energy scan for 50-250 MeV electron beam with 10 cm focal length.	142
Figure 4-13: GEANT4 simulation results obtained for a 250 MeV electron beam passing through a 1 mm thick solid target placed 5 cm from the source. The electron r.m.s. beam size is 1 mm. a) Bremsstrahlung gamma-ray beam (r.m.s) profile vs distance from	

electron source obtained for an Al target changing the electron beam focal length: 10 cm (red dots), 15 cm (light blue dots), 20 cm (black dots) and 30 cm (green dots). b) Bremsstrahlung gamma-ray r.m.s beam profile for different target material Al (red dots), Cu (black dots), In (green dots) and W (grey dots) for 10 cm focal length.	143
Figure 4-14: The graph shows the simulation results for a 250 MeV electron beam passing through a 1 mm thick Al foil placed at different distances from the source, for a fixed focal length of 10 cm. Both the focal length and the spot size at focus depend on the position of the target.	144
Figure 4-15: Gamma-ray beam profile for different target thickness. The simulations are carried out for an Al target placed 5 cm from the source with FL = 10 cm and an electron energy of 250 MeV.	145
Figure 4-16: FP dependence on different parameters: a) target atomic number, b) electron beam FL, c) target thickness.	146
Figure 4-17: Simulation scheme: the red tracks are electrons and green tracks are gamma-rays. The magnetic field deflects the electrons after the Al while the converging γ -ray beam propagates through the water phantom.	148
Figure 4-18: Simulations with magnetic field and water.	148
Figure 4-19: Profile of the energy deposition in tissue for electrons, photons and carbon ions. Image source Ref.[25].	150
Figure 4-20: Bragg position as function of the ion energy calculated for ^{12}C . Image from Ref. [24]	150
Figure 4-21: Gamma knife image from Ref. [27].	153
Figure 4-22: Cyberknife from Ref. [29].	154
Figure 4-23: Deposited energy distribution in a 20 cm water phantom by gamma-rays produced via bremsstrahlung from 250 MeV electrons passing through a 1 mm Al target a) for 1 mrad divergence and b) for a focused beam. The beam propagates from the left side.	156
Figure 4-24: Electron spectrum evolution while interacting with phantom water.	159
Figure 4-25: LWFA electron bunch length evolution as a function of the propagation depth in a water phantom.	159

Figure 5-1: Peak brilliance as a function of the photon energy of third and fourth generation light sources. The stars represent the peak brilliance of the betatron source: green for the highly damped regime, red for the HBR regime and yellow the possible brilliance when scaling up in energy. Image taken from Ref. [4] and modified..... 167

Figure 5-2: Peak brilliance as a function of the pulse duration for second, third and future generation synchrotron light sources compared with a LWFA-driven betatron source (red star). Image taken from Ref. [5] and modified..... 168

List of Tables

Table 1-1: Summary of the performances of fourth generation light sources.	24
Table 3-1: Laboratory sources used for calibration of the Timepix detectors	92
Table 3-2: Summary of the betatron experiment results. Parameters with * in the simulations column are direct output of OSIRIS, in the experiment column are directly measured. The parameters with ** are calculated from other parameters of the same regime. The values for the simulations parameters are all extracted from Figure 2.3....	112
Table 4-1: Electron and target parameters scanned in the simulations.....	126
Table 4-2: Summary of the effects of increasing the parameters listed in the first column on the Bremsstrahlung based gamma-ray source properties given in the heading. Symbols \uparrow , \downarrow and = indicate increasing, decreasing and no effect, respectively.	130
Table 4-3: Simulation parameters used in the converging gamma ray beam studies.	141

Chapter 1

1.1 The X-ray: a Powerful Versatile Tool in Science and Everyday Life

The history of x-rays started in 1895 when Roentgen discovered, three days before Christmas, a new ray that penetrates the body and photographs the bones. He appeared with a photograph of the bones of his wife's hand (Figure 1-1) and immediately the picture and news of these incredible rays that make visible the invisible spread around the world attracting attention of both scientists and the general public: "The realism of this weird picture", reported Popular Science Monthly, "simply fascinated all who beheld it." "hidden solids revealed," proclaimed the New York Times; "a photographic discovery which seems almost uncanny," announced the St. Louis Post-Dispatch [1]. The discovery of x-rays started a real revolution: a new amazing tool was available to explore and understanding matter. Its potential appeared immediately clear: the first medical use was carried out just one month after Roentgen's announcement, when a fracture of the left wrist of a young skater was imaged [2]. A prolific and frantic research activity on x-rays has lead to important breakthroughs in physics, chemistry, biology and

medicine, 15 of which were awarded the Nobel Prize [3]. With the x-ray it was possible for the first time to peep into the micro-world and consequently the idea of acting on the microscopic to control the macroscopic grew. With x-rays the microscopic world has started suggesting and partially revealing its Matryoshka doll-like structure. The insight into the microscopic: molecules, atoms, nucleons, quarks, nanometres, picometres. While the sizes of the objects of study decrease, the required wavelength of the probes decreases. High energy photons reveal a microscopic world and to investigate it even higher energy photons are required. Furthermore, reduced spatial scales are associated with reduced temporal scales of physical processes involving small objects. Exploring the physics at small spatial and temporal scales, drives the quest for further insight and therefore for higher energy and shorter x-ray pulses, which becomes more and more demanding. Currently, x-rays are used to look at atomic and molecular structures while nuclear and sub-nuclear scale processes are studied with large accelerators such as the LHC. However, x-ray technology is now entering the energy and time domain appropriate for nuclear studies. Investigating the ultimate components of matter, sub picometre, sub femtosecond x-ray sources are required and probes for time resolved studies: atto- and zepto-second snapshot of femto- and atto-metres elementary particle (as electrons and quarks). In this progression toward high energy short wavelength photon beams, from 1947, the history of x-rays progressed side by side with synchrotron light sources.



Figure 1-1: The first radiograph: the hand of Bertha Roentgen [4].

1.2 Discovery of Synchrotron Radiation

Between the end of the 19th century and the beginning of the 20th century, Liénard-[5] and Wiechert [6] independently studied and described the electromagnetic field generated by a moving charge, where they understood that any charge experiencing acceleration emits radiation and loses energy. This emission sets a limit to the maximum energy obtainable in particle accelerators, as Ivanenko and Pomeranchuk pointed out in 1944 when they did calculations for betatron accelerators [7]. Attempts to measure the

radiation emitted by electrons in a circular accelerator were carried out in the 100 MeV betatron of General Electric but, although the expected shrinking of the electrons orbit due to the radiative energy loss was observed in 1946 [8], no radiation was measured due to the opaque coating of the tube where the electrons were circulating. The first observation of the new radiation occurred a year later in the General Electric 70 MeV synchrotron accelerator [9], because fortunately, this time, a vacuum tube with a transparent coating was used. The accelerator gave its name to the new radiation that would have a large impact in interdisciplinary science and signalled the beginning of generations of synchrotron light sources.

1.3 Overview: Past, Present and Future Generations of Light Sources

After the discovery of synchrotron radiation, measurements continued to help understanding its potential and the findings stimulated further research. The first generation of synchrotron light sources was in parasitic operation at high-energy physics facilities. Some of the storage rings of the first generation include Tantalus I in Wisconsin, ACO ring in Orsay, SOR in Tokio, DORIS at DESY in Hamburg. It was at DESY, with a 4 GeV electron beam, that x-ray synchrotron radiation was produced in the spectral region down to 0.1 Å. Parasitic operation at high energy facilities limited access to the synchrotron radiation and when important scientific results began to be

produced, there was a demand for dedicated storage rings. Facilities specifically designed for producing synchrotron radiation formed the second generation of light sources. At this point, synchrotron facility users realized how, for many experiments such as spectroscopy or crystallography, the spectral brightness, also called the brilliance, was much more important than flux alone. The brilliance is defined by the National Institute of Standards and Technology as the radiated power per unit solid angle per unit area normal to the direction of propagation of the beam per unit frequency [10]. The current default standard units for this source characteristic are photons $s^{-1} \text{ mm}^{-2} \text{ mrad}^{-2} (0.1\% \text{ bandwidth})^{-1}$. Alternatively, the brilliance is the flux divided by the emittance, which is the distribution of the beam in phase space. The brilliance, as defined, is an invariant quantity so that no optical technique can improve it. Proper design of the ring determines the electron beam characteristic and optimises the radiation properties. Indeed, the photon beam brightness increases as the electron beam emittance decreases. The increase is ultimately limited by diffraction effects. The diffraction-limited emittance is given by $\lambda/4\pi$ where λ is the photon wavelength [11]. The quest for lower emittance beams has therefore been central to the evolution and design of light sources. Undulators and wigglers, sometimes also called insertion devices, placed in the straight sections between bending magnets in the big storage rings, provide a way to take maximum advantage of the intrinsic brightness of a synchrotron. Insertion devices can reduce substantially the angular distribution and, for undulators, approach the diffraction limit. The radiated energy can be increased by a factor N or N^2 for wigglers and undulators, respectively, where N is the number of periods of the

insertion device. A schematic of these three different magnetic structures is shown in Figure 1-2.

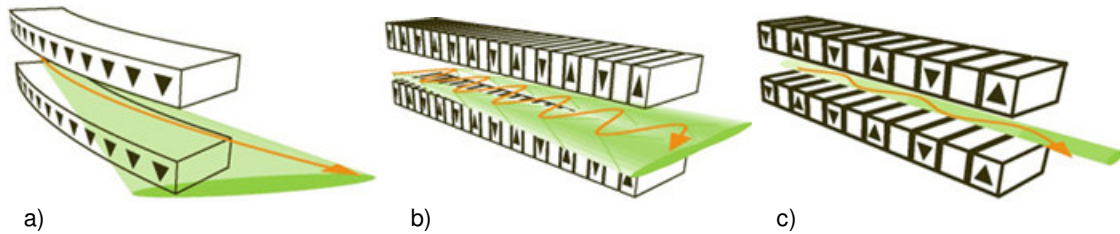


Figure 1-2: Comparison between a) dipole magnet, b) wiggler and c) undulators design. The horizontal emission angle is reduced by a factor $N^{1/2}$ (N is number of periods) for undulators. Images modified from Ref. [4]).

A third generation of synchrotron sources is one optimized for brilliance: having lower emittance and longer straight sections with insertion devices. Some of the last generation of light sources are DIAMOND, ELETTRA, ESRF, BESSY II, PETRA-III and SPring-8. With third generation light sources the peak brilliance (per pulse) is 10^{24} - 10^{25} ph/s/mm²/mrad²/0.1%BW and the average brilliance of 10^{21} ph/s/mm²/mrad²/0.1%BW can be obtained. While new machines will be built, fourth generation light source are planned. Fourth generation performances will be pushed to a much higher level: higher brightness, higher coherence and shorter bunches. An average brilliance of up to five orders of magnitude higher and peak brilliance up to ten orders of magnitude higher than third generation light sources should be achievable. To satisfy the new demands the technology is shifting from storage rings to linear accelerators. The options being considered are: ultra-low emittance storage rings, energy-recovery linacs

(ERLs) and linac-based free-electron lasers (FELs). With the ultimate design for storage rings diffraction-limited emittance, high repetition rate (hundreds of MHz), high transverse coherence and highly stable average flux and brightness should be reached [12]. The pulse length, typically greater than ten picoseconds, limits the maximum peak brilliance achievable. In an ERL source, an injector produces very low emittance bunches, which are then accelerated to high energy in a superconducting linac [13]. These high-energy bunches are passed into a transport system, similar to a section of a third generation storage ring, which includes undulators for the production of synchrotron radiation. Because the beam is not stored in the ring, the very low beam emittance from the linac is approximately preserved in the single turn around the ring. An ERL can work in different modes: high coherence, high charge, high flux, high repetition rate or short bunch modes, down to femtosecond bunch lengths. The disadvantages of this technology are the low bunch current and stability issues. Examples of ERLs for driving FELs are the JLab IR FEL Upgrade, the Japan Atomic Energy Agency (JAEA) FEL, and the Novosibirsk High Power THz FEL. In future, an ERL with very low emittance and high peak current could drive a SASE FEL. An FEL is a device that uses a relativistic beam of electrons passing through a transverse periodic magnetic field (undulator), to amplify electromagnetic radiation [14], where the electrons in the undulator are the lasing medium. An FEL induces micro-bunching of the electron beam on a wavelength periodicity. The micro-bunches emit coherently which results in a strongly enhanced peak brilliance. The FEL can operate in two modes: the seeded FEL and the SASE FEL. In the first case the FEL amplifies an input electromagnetic radiation seed. The second operation mode, self-amplified spontaneous

emission (SASE) FEL, starts from noise due to the random particle phases [14] and the spontaneous undulator radiation emitted in the first sections of a long undulator seeds the remaining part of the undulator. The SASE process is particularly important in the x-ray region where no lasers to seed the FEL are available, which is why the majority of FELs operate in the SASE mode. Linac-based FELs provide short x-ray pulses with very high peak brightness and power, such as the LCLS at the SLAC National Accelerator Laboratory [15]. The average brilliance and the peak brilliance for several light sources are shown in Figure 1-3 as a function of the emitted photon energy and, in Figure 1-4, as a function of the pulse length. The different expected performances of the three fourth-generation light sources are summarized in Table 1-1. With the fourth-generation light sources, femtosecond x-ray beams become available, which substantially widens the research potential and opens the door to new unexplored fields that can contribute to advances both in science and technology, for example:

- attosecond manipulation of molecular dynamics and electron motion [16];
- novel material design and characterization under extreme conditions (pressure, temperature, electromagnetic fields, radiation);
- time resolved biological imaging;
- control of complex materials and chemical processes;
- real time evolution of chemical reactions, motion of electrons and spin;
- imaging and spectroscopy of individual nano objects;
- statistical laws of complex systems;
- simultaneous ultrashort and ultrafast measurements [17].

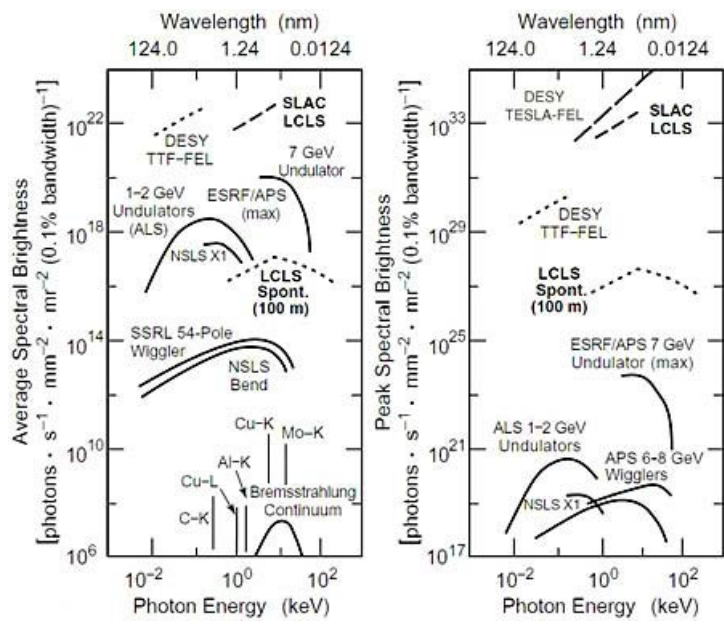


Figure 1-3: Peak brightness for third generation and fourth generation light sources, from Ref. [4].

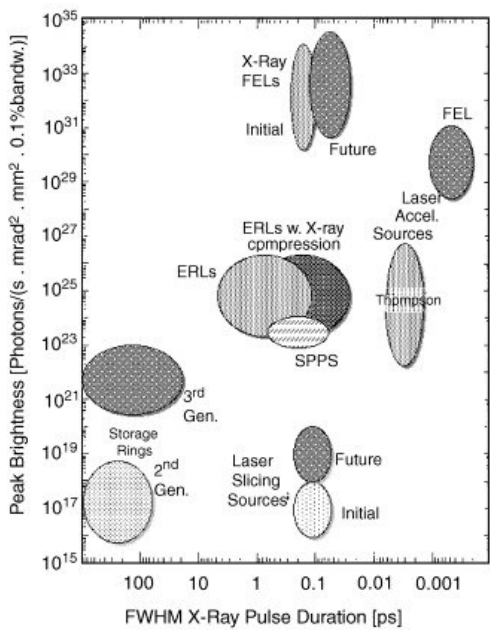


Figure 1-4: Peak brightness vs pulse duration for past and future synchrotron light sources. Image from Ref. [18]

Ultra-low emittance storage rings	
Diffraction limited emittance	High transverse coherence
High average brightness	High frequency (hundreds of MHz)
Picosecond bunch duration	
Energy Recovery Linacs (ERLs)	
Diffraction limited emittance	Full transverse, longitudinal coherence
High average brightness	~10 kHz repetition rate
Femtosecond bunch duration	Low peak current
Linac-based FELs	
Diffraction limited emittance	Full transverse, longitudinal coherence
High average brightness	~100 Hz repetition rate
Femtosecond bunch duration	High peak current
Huge peak brightness	

Table 1-1: Summary of the performance of fourth generation light sources.

1.4 Novel Concept of Light Source: Laser-Wakefield Driven Light Sources

Linacs, synchrotrons and storage rings are well established and reliable technologies, developed after decades of experience. Their advances in performances are facing a limit due to physical restrictions: the acceleration process is based on radio frequency (RF) cavities and RF cavities cannot sustain accelerating gradients greater than 100 MeV/m because of RF cavity breakdown. As a consequence, TeV accelerators

need to be kilometres long; high-energy accelerators are currently the most expensive scientific instruments on earth. To scale down in size and cost higher accelerating gradients are needed. A promising novel technology that potentially could answer this challenge is the laser-plasma wakefield accelerator (LWFA). The LWFA dates back to the late '70s [19]. However, the high power lasers required to demonstrate the LWFA were only available after 1985 [20] when laser technology underwent a critical development. This nascent technology uses a very high power laser focused into plasma. The laser pulse generates plasma waves and electrons that can literally surf the waves. They are accelerated to high energies by the strong electric field of the wave. In this configuration plasma forms the accelerating medium and, being a completely ionised gas, is immune to electrical breakdown and can produce accelerating gradients in excess of 100 GeV/m [21], more than three-orders of magnitude higher than in conventional accelerators. This unprecedented gradient means that the size of accelerators shrinks down by three orders of magnitude: a TeV accelerator based on this technology could in principle be just 10 metres long, if one could keep particles tracking the plasma wave over this distance! Infrastructure costs would consequently be drastically reduced, and thus also the cost.

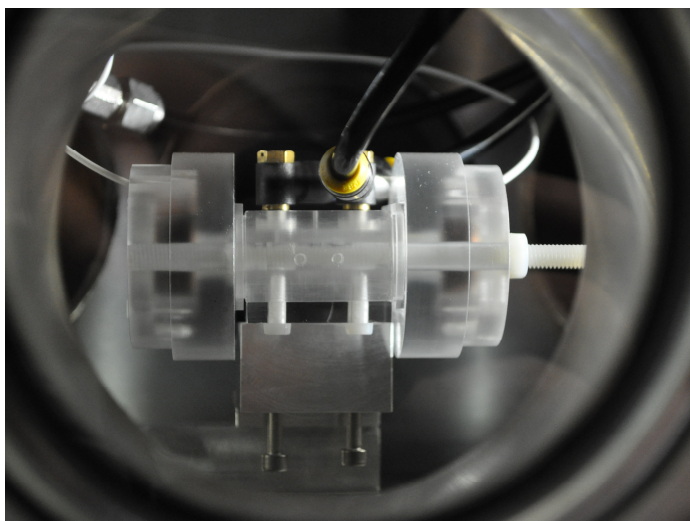


Figure 1-5: 4 cm long laser-plasma accelerator (at Strathclyde) equivalent to a 30 m long conventional accelerator.

The impressive miniaturization in the accelerator size (Figure 1-5) reminds one of the silicon revolution that signalled the passage from valves to transistors and from room size devices to handheld computers. The scientific world, after an initial scepticism, is taking more and more interest in LWFA technology, which has now attracted the nickname: a table-top accelerator.

Laser-plasma wakefield technology is still in its infancy and developing rapidly. Rapid progress has been made over the last few years in understating the physical mechanisms that give rise to acceleration, and the limits of the technology are still not clear: the parallel growth and improvement of laser technology continues to widen its possibilities. It is necessary to point out that, despite the incredible advances, the current performances of laser-plasma accelerators are not comparable yet with highly reliable

conventional accelerators. However, besides having great potential for the future, LWFA are already earning a niche in research and applications. The compactness and low cost should lead to widespread use of the technology in an area where size and cost currently restrict the use of accelerators.



Figure 1-6: Nature cover of the issue of 2004 where three letters on first observation of high quality electron beams were published [22-24].

The first proof-of-principle demonstration of the laser-plasma wakefield was made in 1994 at Osaka University in Japan [25], where electrons were accelerated by only a few MeV. Rapid progress was made in the understanding and control of the acceleration, and in 2004 three groundbreaking papers were published: the “dream beam” papers (Figure 1-6), paper demonstrated a high quality monoenergetic electron beam by laser-plasma acceleration [22-24]. These results included teams led by the University of Strathclyde. However, even before 2004 the LWFA concept started to be associated with the possibility of embedded novel light sources [26] and sources driven by a LWFA

[27, 28]. Soon after in 2004 Rouse et al. [29] demonstrated that a beam of x-ray radiation can be generated simply by focusing a high-intensity laser pulse into a gas jet and a few years later undulator radiation from LWFA electrons was measured [30]. Suddenly the opportunity to dramatically reduce both size and cost of light sources and make them more accessible became realistic.

The current state of the art of LFWA based light sources involves different mechanisms and radiation is produced over the whole spectral region from the infrared to x-rays:

- Transition radiation emitted by LWF accelerated electron bunches passing through a thin metal foil (infrared region [31])

- Laser-driven undulator radiation: electrons accelerated via LWFA are passed through an undulator. The incoherent emitted radiation is tuneable and can range from infrared [30], to VUV [32] to soft x-ray [33] and the pulse duration is sub-100 femtoseconds [30]. The brilliance is of the order of 10^{24} photons/s/mrad²/mm²/0.1% BW, comparable with a third generation light source.

- Thomson backscattering: broad band incoherent x-ray pulses can be produced by backscattering of a laser beam from a relativistic electron bunch [34]. The pulse duration is tens of femtoseconds and the expected peak

brightness, limited by the current performances of Ti:sapphire lasers [30], is around 10^{18} photon/sec/mm²mrad²/0.1%BW

- Synchrotron radiation from electrons during acceleration: electrons while accelerated by the wakefield undergo transverse oscillations in the form of betatron motion and emit synchrotron-like radiation in the energy range from a few keV up to tens of keV [29, 35]. The radiation is spatially coherent as in wiggler radiation and the pulse duration is of the order of ten femtoseconds with a peak brilliance of 10^{22} photons per second per mrad² per mm² per 0.1% BW [35].

- Bremsstrahlung from LWFA electrons: broad spectrum of radiation emitted by electrons decelerated by atomic Coulomb fields while travelling through matter. The pulse length is of the order of picoseconds. The longer light pulse duration compared with other LWFA based light sources is due to the interaction with the matter scattering the electron beam.

These are the light sources that have so far been experimentally demonstrated and with further improvements of the quality of the electron beam, the LWFA may be an optimal driver of an FEL [27]. In this case the peak brilliance is expected to jump by many orders of magnitude up to 10^{32} - 10^{33} photons per second per mrad² per mm² per 0.1% BW (Figure 1-3).

After this brief review of laser-driven light sources it is important to underline two particular features innate in LWFA light sources. First of all, the LWFA electron bunches are as short as a few femtoseconds [31], this means that the current can be extremely high (of the order of kAs) and the corresponding generated light pulse duration is also a few femtoseconds, giving a very high peak brilliance. Producing ultra-short bunches is one of the biggest challenges of conventional light sources and only fourth generation sources will provide such a short bunch duration. Another of the crucial technological challenges for the next generation of light sources is the unprecedented level of synchronization required at femtosecond scale between x-ray, laser, and radio-frequency cavity. This problem is completely overcome with LWFA based light sources because they are intrinsically synchronized with a laser pulse. This is the second unique properties of these novel sources.

The performance of a LWFA driven light source is very promising, even if objectively they are still far away from being a conventional light source, in particular because of their extremely low repetition rate compared with the working frequency of synchrotrons. The advantage of these novel light sources, as described, resides in their ultra short pulse lengths: only future generation synchrotron sources could perhaps achieve this at great cost. Moreover, the margin of improvement is still incredibly large thanks to the rapid development of laser technology and also to the large effort put in by researchers for a deeper understanding of the physics behind the LWFA. The effort is worthwhile because the reward is very high: it could result in a revolution of the concept of accelerators and light sources.

The work of this thesis is mainly focused on understanding and exploring the potential of synchrotron radiation emitted by electrons undergoing betatron oscillations in the LWFA. We investigate in particular the regimes in which accelerated electrons interact with the laser pulse and enter into resonance. We explain theoretically and explore and prove experimentally for the first time how resonance of the laser pulse with harmonics of the electron betatron motion can significantly enhance the synchrotron emission [36] leading to orders of magnitude increase in the photon energy from x-rays to gamma-rays (energy > 100 keV). For ≈ 700 MeV electron beams, we measure 10^8 gamma-ray photons with spectra with critical energy between 60 and 450 keV, and a peak brilliance of $\approx 10^{23}$ photons/(s mrad² mm² 0.1%bandwidth), with 10^7 photons between 1 and 7 MeV, in an energy range where no synchrotron sources exist. We also study the scaling, which shows how with higher power lasers it will be possible to push the emission up to tens of MeV and increase the brightness by orders of magnitude.

The study is extended to investigate a sibling process of synchrotron emission, bremsstrahlung, which for the moment, while waiting for the next generation of lasers, can be used to produce gamma-ray sources above 10 MeV. For the first time, a detailed numerical analysis is done to investigate the tuning knobs for a practical adjustment of the LWFA-bremsstrahlung source properties toward specific applications requirements [36]. These simulations are supported by experimental data.

A further step leads to the investigation of the possibility of producing a converging gamma-ray beam via the bremsstrahlung process. The results are very

encouraging and a proof-of-concept experiment is proposed. A converging gamma-ray beam could have an immediate impact on many fields, from nuclear to imaging to medical applications.

The structure of the thesis is the following:

- In the second Chapter we review the LWFA and basic synchrotron radiation theory. The harmonically resonant betatron regime is then described both analytically and using numerical simulations.

- In the third Chapter the experimental proof of the harmonically resonant betatron regime is described in detail: the challenges of single shot measurements of the radiation are overcome using a pixelated semiconductor detector expressly characterized for the particular energy and flux range by detecting using Compton side scattering [37].

- In the fourth Chapter, bremsstrahlung radiation from LWFA electrons is studied in depth and the dependences on the electron and target properties are correlated with the output radiation. A test experiment shows good agreement with the simulations giving confidence in the possibility of controlling the process for practical applications [38]. The last part of the chapter is dedicated to the study of a new configuration to produce, via bremsstrahlung process, a converging gamma ray beam. Simulations and a

scheme for a proof-of –concept experiment are presented. The impact and possible direct application of this novel “gamma-knife” are also discussed.

- In the fifth and last Chapter results are discussed and future challenges, possible direction for next research step and possible achievements are speculated.

References:

1. Assmus A., "Early History of X Rays", *Stanford Linear Accelerator Center: Beam Line*, **25**(2), 10 (1995)
2. Frost E.B., "Experiments on the X-ray", *Science*, **3**, 235 (1896)
3. "X-rays". Available from: <http://www.nobelprize.org/educational/physics/x-rays/>. (2011)
4. Available from: http://www.nlm.nih.gov/dreamanatomy/da_g_Z-1.html
5. Lienard A., "Champ Electrique et Magnétique Produit par une Charge Electrique", *L'Eclairage Electrique*, **16**, 5 (1898)
6. Wietchert E., "Elektrodynamische Elementargesetze", *Archives Néerlandaises*, **5**(2), 549 (1900)
7. Iwanenko D. and Pomeranchuk I., "On the Maximal Energy Attainable in Betatron", *Phys Rev A*, **65**, 343 (1944)
8. Blewett J.P., "Radiation Losses in the Induction Electron Accelerator", *Physical Review*, **69**(3-4), 87 (1946)
9. Elder F.R., Gurewitsch A.M., Langmuir R.V., and Pollock H.C., "Radiation from Electrons in a Synchrotron", *Physical Review*, **71**(11), 829 (1947)
10. Mills D.M., Helliwell J.R., Kwick A., Ohta T., Robinson I.A., and Authier A., "Brightness, Spectral Brightness or Brilliance - Report of the Working Group on

- Synchrotron Radiation Nomenclature", *Journal of Synchrotron Radiation*, **12**(3), 385 (2005)
11. Winick H., ed. *Synchrotron Radiation Sources : a Primer*. World Scientific Publishing Company, Incorporated Singapore (1994)
 12. Borland M., "A Super-bright Storage Ring Alternative to an Energy Recovery Linac", *Nuclear Instruments and Methods in Physics Research A*, **557**, 230 (2006)
 13. Bilderback D.H., D. B.J., Dale D.S., Finkelstein K.D., Pfeifer M.A., and Gruner S.M., "Energy Recovery Linac (ERL) Coherent Hard X-ray Sources", *New J Phys*, **12**, 035011 (2010)
 14. Bonifacio R., Corsini R., De Salvo L., Pierini P., and Piovela N., "New Effects in the Physics of High-Gain Free-Electron Lasers; a Proposed Experiment and Possible Applications", *La rivista del Nuovo Cimento*, **15**(11) (1992)
 15. Emma P., *et al.*, "First Lasing and Operation of an Angstrom-Wavelength Free-Electron Laser", *Nat Photon*, **4**(9), 641 (2010)
 16. Corkum P.B. and Krausz F., "Attosecond science", *Nat Phys*, **3**, 381 (2007)
 17. *Next-Generation Photon Sources for Grand Challenges in Science and Energy Report of the Workshop on Solving Science and Energy Grand Challenges with Next-Generation Photon Sources*. Available from: http://science.energy.gov/~media/bes/besac/pdf/Ngps_rpt.pdf. (2008)
 18. Miao J., Chapman H.N., Kirz J., Sayre D., and Hodgson K.O., "Taking X-ray Diffraction to the Limit: Macromolecular Structures from Femtosecond X-Ray Pulses and Diffraction Microscopy of Cells with Synchrotron Radiation", *Annual Review of Biophysics and Biomolecular Structure*, **33**, 157 (2004)
 19. Tajima T. and Dawson J.M., "Laser Electron Accelerator", *Phys. Rev. Lett.*, **43**(4), 267 (1979)
 20. Strickland D. and Mourou G., "Compression of Amplified Chirped Optical Pulses", *Opt. Commun*, **56**, 219 (1985)
 21. Leemans W.P. and al. e., "GeV Electron Beams from a Centimetre-Scale Accelerator", *Nat. Phys.*, **2**, 696 (2006)

22. Mangles S.P.D. and al. e., "Electron Acceleration from the Breaking of Relativistic Plasma Waves", *Nature*, **431**, 535 (2004)
23. Geddes C.G.R. and al. e., "High Quality Electron Beams from a Laser Wakefield Accelerator Using Plasma-Channel Guiding", *Nature*, **431**, 538 (2004)
24. Faure J. and al. e., "A Laser-Plasma Accelerator Producing Monoenergetic Electron Beams", *Nature*, **431**, 541 (2004)
25. Nakajima K., *et al.*, "A Proof-of-Principle Experiment of Laser Wakefield Acceleration", *Physica Scripta*, **T52**, 61 (1994)
26. Pukhov A., Sheng Z.M., and Meyer-ter-Vehn J., "Particle Acceleration in Relativistic Laser Channels", *Phys Plasmas*, **6**(7), 2847 (1999)
27. Jaroszynski D.A. and Vieux G., "Coherent Radiation Sources Based on Laser Plasma Accelerators", *American Institute of Physics Conference Proceedings*, **647**, 902 (2002)
28. Jaroszynski D.A., *et al.*, "Radiation Sources Based on Laser-Plasma Interactions", *Philos T Roy Soc A*, **364**(1840), 689 (2006)
29. Rousse A., *et al.*, "Production of a keV X-ray Beam from Synchrotron Radiation in Relativistic Laser-Plasma Interaction", *Phys Rev Lett*, **93**(13), 135005 (2004)
30. Schlenvoigt H.P., *et al.*, "A Compact Synchrotron Radiation Source Driven by a Laser-Plasma Wakefield Accelerator", *Nat Phys*, **4**(2), 130 (2008)
31. Lundh O. and al. e., "Few Femtosecond, Few Kiloampere Electron Bunch Produced by a Laser-Plasma Accelerator", *Nat. Phys.*, **7**, 219 (2011)
32. Anania M., *personal communication* Strathclyde University, (2011)
33. Fuchs M., *et al.*, "Laser-Driven Soft-X-ray Undulator Source", *Nat Phys*, **5**(11), 826 (2009)
34. Schwoerer H., Liesfeld B., Schlenvoigt H.P., Amthor K.U., and Sauerbrey R., "Thomson-Backscattered X Rays From Laser-Accelerated Electrons", *Phys Rev Lett*, **96**(1), 014802 (2006)
35. Kneip S., *et al.*, "Bright Spatially Coherent Synchrotron X-rays from a Table-top Source", *Nat Phys*, **6**(12), 980 (2010)

36. Cipiccia S., *et al.*, "Gamma-Rays from Harmonically Resonant Betatron Oscillations in a Plasma Wake", *Nat Phys*, **7**(11), 867 (2011)
37. Cipiccia S., *et al.*, "A single-shot detector for ultra-fast, high flux, broad energy range X-ray spectroscopy based on Compton scattering", *Journal of Instrumentation*, **submitted** (2011)
38. Cipiccia S., *et al.*, "A tuneable ultra-compact bright gamma-ray source based on bremsstrahlung radiation from laser-plasma accelerated electrons", *J Appl Phys*, **accepted for publication** (2012)

Chapter 2

2.1 Introduction

One of the major milestones in the development of laser technology is the introduction of chirped-pulse amplification (CPA) that has enabled the latest revolution in production of ultra high peak power lasers, amplifying very short pulses to energies above those previously only available for long pulse, high energy lasers [1]. The idea initially came from efforts to overcome the power limitations in radars, and was extended to the optical domain by Strickland and Mourou in 1985 [1]. The principles of the CPA are simple: the laser pulse is stretched from femtoseconds to 100's of picoseconds duration before it is amplified, and then, following amplification, compressed to an ultra-short duration that is close to the initial duration. This prevents catastrophic optical damage to the laser amplifiers due to self-focusing and self-phase modulation, which occur at high intensities. Only robust optical components such as mirrors that can withstand the high power are exposed to the compressed beam. The CPA made possible a leap in peak power from gigawatts to petawatts. There are already

several petawatt laser around the world, such as Nova in Livermore, GEKKO in Osaka, Vulcan at the Rutherford Appleton Laboratory (UK), LULI 2000 in Paris etc.

However, the CPA is also encountering several limitations set by the threshold damage of the diffraction gratings of the compressor, which for higher power are very large extending to over a metre squared, with the related increase in cost. Moreover, pulse compression and the ultimate duration are limited by the bandwidth of the gain medium.

Raman amplification in plasma as an alternative amplification scheme is under study, which could eventually replace or be used with CPA [2]. This technique is based on a long pump laser beam colliding with a short counter-propagating probe beam in plasma, which can tolerate a much higher laser intensity than a solid-state amplifier. The two counter propagating beams differ in frequency by the plasma frequency and interact via stimulated Raman backscattering, and a large fraction of the energy of the pump laser can be transferred to the probe. Recent numerical studies [3] predict the feasibility of a multi-petawatt laser based on Raman amplification within a parameter window that avoids parasitic plasma instabilities. A successful experiment [4] has shown the potential of chirped pulse Raman amplification (CPRA) to serve as a high-efficiency high-fidelity amplifier/compressor stage.

Why is there a thirst for high power? Ultra-short duration, high power laser pulses can widen the possibilities of existing technologies and open up frontiers in new physics:

e.g. electron-positron plasma production from vacuum, lab-scale studies of astrophysical conditions, such as neutron stars, black holes and gamma ray bursts, inertial confinement fusion, table-top ion and electron accelerators based on laser-solid target or laser-gas interactions and new ultra-compact light sources ranging from the infrared to gamma-rays.

2.2 Laser-Plasma Wakefield Accelerators

The laser-plasma wakefield accelerator story starts in 1979 when, six years before the advent of the CPA, Tajima and Dawson proposed a new mechanism to accelerate electrons to relativistic energies in very short distances using high-power lasers propagating in underdense plasma [5]. As the laser pulse propagates it generates a plasma wave and traps electrons which then surf the wave and accelerate. The rapid growth of CPA technology after 1985 gave rise to compact sources of high power, ultrashort laser pulses. Already in 1995 Modena et al. [6] demonstrated an acceleration gradient in laser driven plasma waves of ~ 100 GV/m. The high accelerating gradient was astonishing: plasma as an accelerating medium is fully ionised and is immune to electrical breakdown. Electrical breakdown leading to the formation of plasma is the major limiting factor for the maximum achievable accelerating gradient in conventional RF accelerators, fixed at about 100 MV/m, which is more than three orders of magnitude lower than in a laser-plasma accelerator. These results are opening the way to an incredible reduction in the size of accelerators. However, until recently, the quality of

electron beams was not extraordinary: even for a maximum energy of around 100 MeV and charge ~ 1 nC, the energy spectral distribution was thermal with an exponential decay. A step improvement in the electron beam quality and better control of the laser and electrons parameters was achieved in 2004. Three groups in different laboratories around the world, simultaneously reported the production of quasi-monoenergetic beams using a LWFA in three seminal papers called the "Dream Beam" papers [7-9]. High energy (~ 100 MeV), quasi mono-energetic (few percents energy spread) and significant charge (>100 pC) were produced. Following this initial advance a deeper understanding of the mechanism has led to a better mastering of the accelerating process, which has resulted in large improvements in the quality of the electron beams and extension of the maximum energy achievable to 1 GeV [10] and above. Beam emittances of the order of 1π mm mrad [11], narrow energy spreads less than 1% [12], femtosecond duration bunches [13] and kiloAmpere peak currents have now been demonstrated. The present parameters are still far away from the energy and luminosity required for high energy physics, but it is worthwhile remembering that this is still a very young technology compared with conventional RF accelerators which date back to the first decades of the 20th century. A rapid growth can be forecast over the next few years, which should lead to further increases in energy, peak current, reductions in size, lower costs and higher reliability. Even though they will not replace conventional accelerators for the moment, it is highly likely that laser-plasma accelerators will be employed in niche fields that require compactness e.g. as drivers of table top light sources for imaging or medical applications.

2.2.1 LPWA Basic Concepts

In a LPWA the passage of the laser in underdense plasma generates density waves. Plasma is underdense if its density is below the critical density, n_c , which is the density above which the laser is unable to propagate. This occurs when the plasma frequency, $\omega_p = (n_p e^2 / m_e \epsilon_0)^{1/2}$, equals the incoming laser frequency ω_0 , so that $n_c = \epsilon_0 m_e \omega_0^2 / e^2$, where e and m_e are the charge and rest mass of electrons, ϵ_0 is the vacuum permittivity and n_p the plasma density. Electrons can surf the waves generated by the passage of the laser pulse and be accelerated, quickly acquiring a velocity nearly equal to the speed of light, and higher than the phase velocity of the plasma wave (Figure 2-1). The acceleration lasts until electrons outrun the wave. The distance that the trapped and accelerating electrons travel before they outrun the plasma wave is called the dephasing length, L_{deph} . The plasma wave travels at a phase velocity equal to the group velocity, v_g , of the laser in the plasma and $\beta_\phi = \frac{v_g}{c}$. Assuming that the electrons have a velocity $\beta_e = \frac{v_e}{c} \approx 1$, the electrons overtake the wave after a time $t = \lambda_p / 2c (\beta_e - \beta_\phi)$, where $\lambda_p = 2\pi c / \omega_p$ is the plasma wavelength. Because $\beta_e \rightarrow 1$ and $\beta_\phi = \frac{v_g}{c} = \left(1 - \frac{n_p}{n_c}\right)^{1/2} \approx 1 - \frac{1}{2} \frac{n_p}{n_c}$ in underdense plasma, then $t \approx \frac{n_c \lambda_p}{n_p c}$. The dephasing length is therefore given by:

$$L_{\text{deph}} = \frac{n_c}{n_e} \lambda_p. \quad (2.1)$$

The plasma wave is generated by the light pressure of the laser due to the gradient of the energy density, which gives rise to a ponderomotive force. The ponderomotive force can be derived by considering the electron fluid momentum in the cold fluid limit [14]:

$$\frac{d\vec{p}}{dt} = -e(\vec{E} + \vec{v} \times \vec{B}), \quad (2.2)$$

where $\frac{d}{dt} = \frac{\partial}{\partial t} + v \cdot \nabla$, v is the electron velocity, $\vec{E} = -\frac{\partial \vec{A}}{\partial t}$ and $\vec{B} = \nabla \times \vec{A}$ are the electric and magnetic fields of the laser and A is the laser vector potential. Introducing the normalized vector potential $|a| = \frac{e}{m_e c} |A|$ in the linear limit $|a| \ll 1$, the dominant term in the solution of equation (2.2) is the quiver momentum $\vec{p}_q = m_e c \vec{a}$, from $\frac{\partial \vec{p}_q}{\partial t} = -e\vec{E}$.

Letting $\vec{p} = \vec{p}_q + \delta\vec{p}$ then the equation gives:

$$\frac{d\delta\vec{p}}{dt} = -\vec{p}_q/m_e \cdot \nabla \vec{p}_q - \vec{p}_q \times (c\nabla \times \vec{a}) = -m_e c^2 \nabla a^2 / 2 = -\frac{e^2}{2m_e} \nabla A^2 = \vec{F}_p, \quad (2.3)$$

which is the expression for the ponderomotive force F_p for the non relativistic case. For the relativistic regime we can substitute m_e by γm_e . The validity of this simple

approach is confirmed by more accurate calculations carried out by Quesnel and Mora [15], which give the same result when the following assumptions are made: the pulse length $c\tau$ is much longer than the laser wavelength λ_0 such that $\sigma = \frac{\lambda_0}{c\tau} \ll 1$; the transverse scale of the intensity gradient is much larger than the wavelength such that $\varepsilon = \frac{1}{k_0 w_0} \ll 1$, where k_0 is the laser wave number and w_0 is the beam waist ($1/e^2$ beam intensity radius at focus); the initial electron velocity, normalized to c , is small compared with both ε and σ . The expression for the ponderomotive force, in the relativistic case, becomes:

$$F_p = -\frac{e^2}{2m_e\gamma} \nabla A^2 = -\frac{m_e c^2}{2\gamma} \nabla a^2. \quad (2.4)$$

The ponderomotive force expels electrons from the laser path producing a local reduction in the electron density [16]. This and the relativistic electron mass increase due to the quivering motion of the electron, which in turn depends on the normalized vector potential in the strong electromagnetic field of the laser, results in an increase of the refractive index, which in turn leads to self-focusing. This occurs just above the power threshold when the rate of self-focusing exactly counter-balances the natural diffraction of the laser pulse. This is known as the critical power and is given by the following expression [16]:

$$P_c = 17 \omega_0^2 / \omega_p^2 [\text{PW}]. \quad (2.5)$$

While propagating through the plasma the laser loses energy to the plasma wave. The distance over which the laser pump energy is depleted is called the depletion length, L_{depl} . To estimate the depletion length we can calculate the length over which the energy deposited into the plasma equals the laser energy. If E_p is the electric field associated with the plasma wave, then the energy density of the plasma wave is $U_{\text{plasma}} = \frac{1}{2} \epsilon_0 E_p^2$. Modelling the volume occupied by the plasma column as a cylinder with a length L , equal to that of the column and a base area given by the focal spot size, then $V_{\text{plasma}} = \pi w_0^2 L$ and the total energy deposited inside the plasma is $W_{\text{plasma}} = U_{\text{plasma}} V_{\text{plasma}}$. The laser energy density is $U_{\text{laser}} = \epsilon_0 E_L^2$, where E_L is the electric field of the laser, and the volume occupied by the laser with a pulse length $c\tau$ is $V_{\text{laser}} = \pi w_0^2 c\tau$. The total energy of the laser is therefore $W_{\text{laser}} = U_{\text{laser}} V_{\text{laser}}$. When full depletion occurs, W_{plasma} equals W_{laser} . Therefore, equating the two expressions, it is possible to find the depletion length L_{depl} . The expression for E_p varies depending on the type of mechanism that excites the plasma wave. The precise expression for E_p and L_{depl} in the case of the LWFA will be calculated later in the chapter.

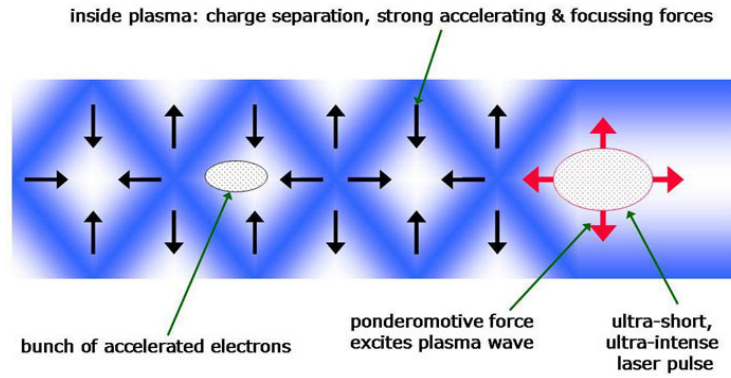


Figure 2-1: Schematic of the LWFA mechanism: the ponderomotive force of the laser excites plasma waves and electrons surfing the wave are accelerated.

2.2.2 Guiding of High-Intensity Laser Pulses

The length over which laser-plasma interactions are strong for a focused beam is limited to the Rayleigh range $z_R = \frac{\pi w_0^2}{\lambda_0}$ [17], which can be further restricted by ionization induced refraction. The Rayleigh length of a laser beam is the distance from the beam waist over which the intensity halves due to diffraction. A particularly promising approach for guiding intense radiation over many Rayleigh lengths is using a preformed plasma waveguide [18, 19]. The ideal plasma waveguide has a parabolic radial electron density profile: $n_e(r) = n_e(0) + \Delta n_e (r/r_{ch})^2$, with $n_e(r)$ the electron density at a distance r from the axis, and Δn_e is the increase in the electron density at $r = r_{ch}$ [17]. In the absence of further ionization by the laser, and when ponderomotive

and relativistic effects can be neglected, the laser can propagate with constant spot radius if the following matching condition is satisfied [20]:

$$r_M = \left[r_{\text{ch}}^2 / (\pi r_e \Delta n_e) \right]^{1/4}. \quad (2.6)$$

with $r_e = \frac{1}{4\pi\epsilon_0} \frac{e^2}{m_e c^2}$, the classical electron radius.

A reliable technique for producing a fully ionised plasma waveguide is using a hydrogen-filled capillary where the plasma is formed by high voltage discharge [17, 21]. The capillary discharge waveguide is usually manufactured out of alumina or sapphire and filled with gas, usually hydrogen, via small holes located a few millimetres from each end of the capillary. A pulsed discharge current of several hundred amperes, and several hundred nanoseconds duration, is driven through the capillary via electrodes placed at each end of the capillary. This waveguide extends by an order of magnitude the distance over which the electron can be accelerated in a laser-plasma accelerator and allows energies in the GeV range to be reached [22]. Measurements [21] that agree with simulations [23] have shown the channel produced with this device is approximately parabolic and the gas is fully ionised. A method of manufacturing capillary discharge waveguides using the femtosecond laser micromachining technique has been pioneered at Strathclyde [24, 25]. A plasma waveguide can alternatively be produced using an igniter-heater method using the two laser pulses [26] in which the first weakly ionises

the plasma channel while the second heats the plasma to form an expanding column which forms a plasma channel.

Making use of the self-focusing properties of high intense laser pulses in plasma is another way to self-guide a laser over many Rayleigh lengths. This has been proved experimentally, which shows that self-guiding allows the wakefield to evolve to the correct shape for production of monoenergetic electron bunches [27]. It has also been found that the length over which an intense pulse can be guided scales with the electron plasma density n_e [28].

2.2.3 Laser Plasma Accelerator Configurations

There are three main configurations: laser-wakefield accelerator (LWFA) [5, 29-31], the plasma beat-wave accelerator (PBWA) [32], and self-modulated laser-wakefield accelerator (SM-LWFA) [33].

Laser-plasma wakefield accelerator: A short duration, high intensity, laser pulse with frequency, ω_0 , much larger than the plasma frequency ω_p , can excite a plasma wake analogous to a boat producing a wake in the sea or lake [5]. If the laser pulse duration is approximately equal to the plasma wavelength then the density wave is efficiently driven. Electrons can surf the plasma wave as a surfer on an ocean wave gains

momentum from the wave and is accelerated. A more detailed description of the mechanism is given in Section 2.3.

The plasma beat-wave accelerator (PBWA): The plasma beat-wave accelerator scheme was first proposed by Dawson and Tajima [5] as an alternative to the LWFA in 1979 because the CPA had not yet been developed and ultra short duration, high power laser pulses were not available. This scheme is based on two long laser pulses with frequencies, ω_1 and ω_2 , adjusted so that the difference frequency equals the plasma frequency i.e. $\Delta\omega = \omega_1 - \omega_2 = \omega_p$. When this condition is satisfied large amplitude plasma density waves are resonantly generated. Electrons that are injected with the correct phase can be trapped in the wave potential and be accelerated. However, several limitations were found, mainly due to plasma density inhomogeneities and instabilities. For example, while the electron plasma wave grows the associated electric field grows and the plasma electrons can acquire relativistic velocities which increases the effective mass resulting in a red-shift of the plasma frequency and a loss of resonance. Other limitations came from laser diffraction and pump depletion. Diffraction sets the maximum interaction length to the Rayleigh length. However, this can be overcome with a plasma waveguide. Pump depletion could be avoided or postponed using a more powerful laser.

Self-modulated laser-plasma wakefield accelerator (SM-LWFA): This mechanism of acceleration is a hybrid scheme combining Raman forward scattering [5] with laser wakefield acceleration. Raman forward scattering is the resonant decay of the

incoming laser wave, with frequency ω_0 into a plasma wave having frequency ω_p and two electromagnetic waves with frequencies $\omega_0 \pm \omega_p$. The plasma wave is resonantly driven by the ponderomotive force associated with the beat of the incident and the scattered waves. The plasma wave results in modulation of the refractive index

$$n = \sqrt{1 - \frac{\omega_p^2}{\omega_0^2}} : \text{ higher density zones correspond to lower refraction index and vice versa.}$$

If the laser pulse is longer than the plasma wavelength then the laser pulse experiences a series of refractive index modulations, which produce focusing and defocusing effects leading to low amplitude modulations. The modulated laser in turn resonantly excites the wakefield, the process continues in an unstable way and the laser is self-modulated [34]. The self-modulation regime depends strongly on the laser power and dramatically increases when the laser power P exceeds the critical power for self-focusing P_c [16].

Summarising, the conditions for self-modulation are a laser pulse longer than the plasma wavelength, $L > \lambda_p$, and a laser power larger than the critical power, $P > P_c$. In SM-LWFA acceleration is enhanced compared with LWFA for fixed laser parameters and the self-modulated regime produces a higher amplitude wake field because of the higher electron density required and because the wakefield is resonantly excited by a series of micro-pulses as opposed to a single pulse as in the LWFA. Moreover, relativistic self-focusing increases the normalized vector potential of the laser a_0 and simulations show that the laser pulse remains guided over a longer length than in the LWFA [14]. In contrast, the disadvantages of the SM-LWFA is the higher electron density and therefore a lower laser group velocity, which results in a shorter dephasing

length and therefore lower electron energy. The quality of the electron beam is another weakness of the self-modulated regime because the electron beam emerges from the acceleration with a broad energy spread and large dark current due to continuous trapping over the short dephasing length [14].

2.3 Laser-Plasma Wakefield Acceleration

2.3.1 Theory of the LWFA

Considering an electromagnetic pulse with a frequency ω_0 and wave number k_0 , travelling inside cold plasma, the dispersion relation is given by $\omega_0^2 = c^2 k_0^2 + \omega_p^2$. Therefore, the electromagnetic wave propagates in plasma with a group velocity $v_g^{EM} = \frac{\partial \omega_0}{\partial k_0} = c(1 - \omega_p^2 / \omega_0^2)^{1/2}$. Let us assume the laser propagates along the z direction and has the electric field oriented along y . Considering the heavy ions as immovable (or stationary), the laser causes the light electrons to undergo transverse oscillations with a mean oscillatory energy $\langle \Delta W_e \rangle = m_e \langle v_y^2 \rangle / 2 = e^2 \langle E_y^2 \rangle / 2m_e \omega_0^2$. If the amplitude of the electromagnetic wave is homogenous, the time averaged force on an electron is zero and the electron returns to its original position once every cycle. This does not occur for a focused laser pulse. The spatial variations in the laser intensity

cause a spatially varying ponderomotive force, expressed by Eqn. (2.4). As a result, electrons are displaced along the z axis by $\Delta z = \langle \Delta v_z \rangle \tau$, where τ is the laser pulse duration. Following passage of the laser pulse electrons are attracted back by the space charge forces produced by the displacement and a plasma oscillation sets in. The excitation of the wave is most efficient when the laser pulse length is about half of the plasma wavelength. Under idealized conditions the excited plasma wave travels with a phase velocity equal to the group velocity of the laser pulse $v_\phi = \frac{\omega_p}{k_p} = v_g^{laser}$. However, as discussed earlier, the laser etches back because of local pump depletion due to energy transfer to plasma electrons. Decker et al. [35] estimated the etching velocity for a short, high intense laser pulse to be:

$$v_{etch} = c \frac{\omega_p^2}{\omega_0^2}. \quad (2.7)$$

From (2.7) the depletion length can be calculated to be

$$L_{depl} = c \frac{\omega_p^2}{\omega_0^2} \tau. \quad (2.8)$$

Therefore the phase velocity of the wake can be expressed as

$$v_\phi = v_g - v_{etch} \approx c \left(1 - \frac{3\omega_p^2}{2\omega_0^2} \right). \quad (2.9)$$

The electric field associated with the wake can be estimated considering a sinusoidal periodic perturbation. The density perturbation can be written as $\delta n = \delta n_e \sin(k_p z - \omega_p t)$ and therefore, from Poisson's law, the associated electric field is

$$\delta E_p = E_0 \frac{\delta n_e}{n_e} \cos(k_p z - \omega_p t), \quad (2.10)$$

where E_0 is the amplitude, which is given by

$$E_0 = \frac{m_e c \omega_p}{e}. \quad (2.11)$$

2.3.2 Wave-Breaking

The plasma oscillation amplitude is limited by the wave-breaking condition. The wave breaks when the electron velocity reaches the phase velocity of the wave. Wave-breaking corresponds to trapping of background plasma electrons. The critical longitudinal field attainable is

$$E_{WB} = E_L \approx E_0, \quad (2.12)$$

with E_0 given by (2.11).

When the limit is reached, the wave steepens and a crest forms and falls into the trough. At this point $\partial E_L / \partial z$ tends to infinity and, from Gauss's law, so does the plasma density. This wave-breaking limit is valid for the cold non-relativistic case. However, the wave breaks when the electrons have a velocity v_e close to the phase velocity v_p of the plasma wave; that is, the electrons are fully relativistic and therefore the relativistic effect must be included. With γ_p the Lorentz factor associated with the plasma wave phase velocity, it has been shown [36, 37] that the maximum amplitude of the plasma wave is given by:

$$E_{WB} = \sqrt{2(\gamma_p - 1)} E_0. \quad (2.13)$$

which is called the relativistic wave-breaking field. These calculations do not take into account thermal effects. However, even a small amount of thermal energy can significantly reduce the wave-breaking field value [38]. Indeed, thermal effects reduce the wave-breaking amplitude for two reasons: firstly, the plasma pressure works against the tendency of the plasma density to increase to infinity and secondly, the thermal velocity of the particles enables trapping at a lower amplitude than if they were initially at rest [39]. In other words, the wave-breaking condition ($v_e \rightarrow v_p$) is more readily

satisfied by the faster electrons within a thermal distribution. Katsouleas and Mori [38] calculated the wave-breaking amplitude in the warm relativistic regime to be

$$E_{WB} = m_e c \omega_p e^{-1} \beta^{-1/4} \left(\ln 2 \gamma_p^{1/2} \beta^{1/4} \right)^{1/2}. \quad (2.14)$$

where $\beta = 3T/m_e v_p^2$, with T the plasma thermal energy.

2.4 The Bubble Regime

2.4.1 The Broken-Wave Regime

In 2002, Pukhov and Meyer-ter-Vehn explored numerically a highly non-linear broken wave regime [40]. For a high intensity laser with a pulse length shorter than the plasma wavelength and a (relativistic) intensity sufficiently high to break the plasma wave on the first oscillation they found a new regime where the laser wake takes the shape of plasma cavities or “bubbles”, which gives rise to the definition of the "bubble regime". The bubble is characterized by three different density regions: the electron-evacuated ion bubble, a high density electron sheath surrounding the ion cavity and the electron beam stem that is formed by the accelerated self-trapped electrons (see Figure 2-2). The electric field required to enter this regime is estimated from the cold-

relativistic model that holds for low temperature plasma. Wave breaking gives rise to abundant self-trapped electrons in the bubble. The bubble structure that follows the laser pulse appears to be very stable and not affected by the depletion of laser energy due to energy transferred to electrons.

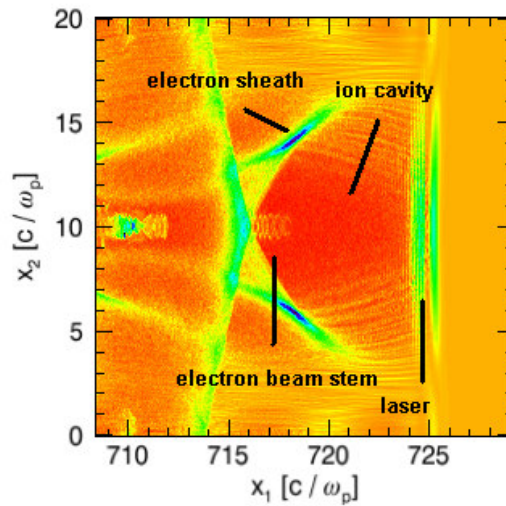


Figure 2-2: Bubble picture obtained from OSIRIS [41] simulation showing the three different density regions that identify the bubble: the ion cavity behind the laser pulse, the high density electron sheath and the trapped electrons forming a stem.

The bubble radius can be estimated by requiring that the electrostatic restoring force is balanced by the ponderomotive force at the surface of the bubble

$$k_p R \approx F_p \propto k_p \nabla a_0^2 / \gamma \approx a_0 / (k_p R). \quad (2.15)$$

Through 3D particle in cell (PIC) simulations Lu *et al.* [42] found a refined condition to limit the laser spot size variation over the self-guided distance

$$k_p R \approx 2\sqrt{a_0}. \quad (2.16)$$

To calculate the electric field experienced by electrons trapped inside the cavity, the bubble can be modelled as a sphere moving along z with velocity v_g on a background of stationary positively charged ions. Using Gauss' law the electric potential inside the bubble can be written as:

$$\Phi = \frac{en_e}{\epsilon_0} \left(\frac{R^2}{6} - \frac{r^2}{6} \right), \quad (2.17)$$

Where $r^2 = x^2 + y^2 + \xi^2$ and $\xi = z - v_g t$ is the co-moving coordinate along the direction of propagation of the pulse [43]. Therefore the contribution given by the electrostatic field of the bubble is

$$\vec{F}_b = -e\nabla\Phi = -\frac{e^2 n_e}{\epsilon_0} \nabla \left(\frac{x^2 + y^2 + \xi^2}{6} \right) = -\frac{\omega_p^2}{3} m_e \vec{r}. \quad (2.18)$$

Part of the bubble is filled by the laser pulse and when electrons, while accelerated, enter in the region occupied by the laser they experience its field. If A is the laser vector potential, the Lorentz force due to the laser field is

$$\vec{F}_L = -e \left(-\frac{\partial \bar{A}}{\partial t} + \vec{v} \times (\nabla \times \bar{A}) \right), \quad (2.19)$$

The total force acting on the electrons can therefore be expressed as

$$\vec{F} = -e \left(\nabla\Phi - \frac{\partial \bar{A}}{\partial t} + \vec{v} \times \nabla \times \bar{A} \right) = \vec{F}_b + \vec{F}_L, \quad (2.20)$$

2.4.2 Electron Injection

The condition for an electron to be trapped in the wake potential is that its speed approaches the speed of the bubble and the bubble moves at the group velocity of the laser in plasma. If γ_e , γ_g and ϕ are respectively the electron Lorentz factor, the laser Lorentz factor and the bubble potential in the laboratory frame and γ'_e and ϕ' in the

frame co-moving with the bubble, then the condition for an electron to be trapped is that the potential is greater or equal to the kinetic energy of the electron

$$e\phi' \geq (\gamma_e' - 1)m_e c^2. \quad (2.21)$$

In the lab frame, the plasma wave is purely electrostatic and the magnetic vector potential is zero, therefore $\phi' = \gamma_g \phi$. The Lorentz transformation for the particle energy is $E' = \gamma_g E - \beta_g \gamma_g p_z$ [44] that, normalised by the electron rest mass, gives $\gamma_e' = \gamma_g \gamma_e (1 - \beta_g \beta_e)$, therefore the condition (2.21) becomes

$$\phi \geq \left(\gamma_e (1 - \beta_g \beta_e) - \frac{1}{\gamma_g} \right) \frac{m_e c^2}{e}. \quad (2.22)$$

For $\beta_g \rightarrow 1$, $\beta_e \ll 1$ and assuming a sinusoidal potential with wave number $k_p = \frac{\omega_p}{c}$, the corresponding trapping electric field is given by

$$E_{trapping} = k_p \phi \approx \frac{\omega_p m_e c}{e}, \quad (2.23)$$

which is the cold non relativistic wave-breaking field (see equation (2.11)).

2.4.3 Electron Acceleration in the Bubble Regime

Electrons trapped inside the bubble are longitudinally accelerated by the force expressed by (2.20). Acceleration lasts until the electrons outrun the wave. The dephasing length in the bubble regime can be calculated considering the time required for the electron to cover a distance equal to R , the radius of the bubble. Assuming that the electrons are highly relativistic, $v_e \rightarrow c$, and using the phase velocity (2.9), we obtain [42]

$$L_{deph} \simeq \frac{c}{c - v_\phi} R \simeq \frac{2}{3} \frac{\omega_0^2}{\omega_p^2} R. \quad (2.24)$$

In general, the energy gained in an acceleration length L_{acc} is

$$\Delta E = eE_{WF} L_{acc} = \varepsilon_{WF} l_{acc} m_e c^2, \quad (2.25)$$

where E_{WF} is the average wake field experienced by the electrons during acceleration along L_{acc} , $\varepsilon_{WF \max} = eE_{WF \max} / m_e c \omega_p$ and $l_{acc} = L_{acc} \omega_p / c$. The maximum energy gained is obtained when the electrons are accelerated up to the dephasing length.

This is possible if $L_{etch} > L_{deph}$, that is $c\tau \geq \frac{2}{3} R$, which means that if the pulse is too short,

dephasing will not be reached. Because the bubble is roughly a sphere the electrons will travel a distance equal to R in the co-moving frame before reaching dephasing. Lu *et al.*

[45] calculated E_{WF} inside the bubble and showed that for $a_0 > 4$ the wakefield grows linearly with the distance from the centre of the bubble, i.e. the maximum field attainable is $\varepsilon_{WF \max} = k_p R/2$. Then, from (2.16) $\varepsilon_{WF \max} \approx \sqrt{a_0}$. Because the wakefield varies almost linearly then the average field is $\varepsilon_{WF} = \sqrt{a_0}/2$. Putting all together, (2.25) becomes

$$\Delta E \approx \frac{2}{3} m_e c^2 \left(\frac{\omega_0}{\omega_p} \right)^2 a_0. \quad (2.26)$$

2.4.4 Beam loading

The incredibly high accelerating gradient makes LWFA extremely attractive; however, the acceleration gradient is just one of the main benchmarks for a particle accelerator. Other parameters that play an important role are the number of particles that can be accelerated, expressed by the luminosity, which is the number of particles per unit area and unit time, and the beam quality, given by the emittance, i.e. the phase space area occupied by the beam while propagating. In 1987 Katsouleas gave a first quantitative estimation of the maximum number of particle that can be accelerated in the linear regime of a plasma-based accelerator [46]. The wake of the driver is superimposed by the wake generated by the accelerated electrons to obtain the final form of the wake field. An estimate for the non-linear regime was given by Lu *et al.* [42] in

2007 based on energy balance. In Ref. [42] the bubble is assumed spherical and the total electromagnetic energy \mathcal{E} is calculated in the ion channel in the absence of the electron bunch. A similar amount of energy was estimated to be in the high density sheath surrounding the bubble, therefore the total energy available in a plasma wavelength is $2\mathcal{E}$. If N is the total number of particles in the bunch and $\langle E_z \rangle$ is the average accelerating field experienced by the electrons, then the total energy gained by the bunch in a plasma wavelength, assuming it to be $2R$, is $Ne\langle E_z \rangle 2R$. The balancing condition gives the relation

$$Ne\langle E_z \rangle 2R \simeq 2\mathcal{E}. \quad (2.27)$$

In Ref. [42] the estimates for the energy and the average accelerating field are

$$\mathcal{E} \simeq \frac{1}{60} (k_p R)^5 \left(\frac{m_e^2 c^5 \mathcal{E}_0}{e^2 \omega_p} \right), \quad (2.28)$$

$$\langle E_z \rangle \simeq \frac{1}{4} \frac{m_e c \omega_p}{e} k_p R, \quad (2.29)$$

therefore Eqn. (2.27) becomes:

$$N \simeq \frac{1}{15} \frac{(k_p R)^3}{k_p r_e}. \quad (2.30)$$

2.5 Betatron Oscillations

Electrons injected into the bubble with a nonzero transverse momentum experience both the longitudinal accelerating field and a transverse restoring force due to the ion background. This latter force gives rise to transverse oscillations, called betatron oscillations and the oscillating electrons emit a collimated beam of synchrotron radiation [47, 48]. Considering a simple model of a single electron propagating in an ion channel along the z direction, the restoring force can be calculated from Gauss' law and the equation of motion is given by [43]

$$\frac{d\vec{p}}{dt} = \vec{F}_{res} = -m_e \omega_p^2 \vec{r}_\perp / 2, \quad (2.31)$$

where r_\perp is the electron transverse position. The electron oscillate with a betatron frequency

$$\omega_{\beta} \sim \omega_p / \sqrt{2\gamma}, \quad (2.32)$$

with γ the electron Lorentz factor. The oscillatory motion is similar (or analogous) to the motion of electrons inside an undulator or wiggler [49]. However, here the plasma acts as a wiggler with periodicity λ_b and the strength parameter a_{β} is given by

$$a_{\beta} = \gamma \vartheta = \gamma k_{\beta} r_{\beta}, \quad (2.33)$$

where ϑ is the maximum deflection angle of the oscillatory trajectory, k_b is the betatron wavenumber and r_b is the betatron oscillation amplitude. As in a conventional insertion device, synchrotron radiation is emitted by the relativistic electrons [44]. The radiation is emitted in a narrow cone

$$\vartheta = a_{\beta} / \gamma. \quad (2.34)$$

The properties of the radiation depends strongly on a_{β} : if $a_{\beta} \ll 1$ the electron motion is near the propagation axis and the radiation is primarily emitted at the fundamental frequency

$$\omega_f = \omega_\beta 2\gamma^2 = \sqrt{2}\gamma^{3/2}\omega_p, \quad (2.35)$$

which is the betatron frequency Doppler shifted in the laboratory frame. For $a_\beta > 1$, the amplitude of the electron oscillations grows and high harmonics are radiated and a broadband spectrum is emitted. The spectral intensity grows up to the critical frequency given by [50]:

$$\omega_c = \frac{3c\gamma^3}{2R}, \quad (2.36)$$

with $R = k_\beta^2 / r_\beta$, the effective radius of curvature of the electron trajectory. The frequency spectrum can be obtained from the Fourier transform of the temporal distribution of the electric field at the observer. If \vec{n} is the direction of observation, the radiation emitted per unit frequency and unit solid angle can be calculated from Liénard–Wiechert potentials [44]:

$$\frac{d^2 I}{d\omega d\Omega} = \frac{e^2}{4\pi^2 c} \left| \int_{-\infty}^{+\infty} \vec{E}(\vec{r}, t) e^{i\omega(t - \vec{n} \cdot \vec{r}(t)/c)} dt \right|_{\mathbb{K}}^2, \quad (2.37)$$

where

$$\vec{E}(\vec{r}, t) = e \left[\frac{\vec{n} - \vec{\beta}}{\gamma^2 (1 - \vec{\beta} \cdot \vec{n})^3 R^2} \right]_{ret} + \frac{e}{c} \left[\frac{\vec{n} \times [(\vec{n} - \vec{\beta}) \times \dot{\vec{\beta}}]}{(1 - \vec{\beta} \cdot \vec{n})^3 R} \right]_{ret}. \quad (2.38)$$

The subscript “ret” indicates that the quantity in the square brackets has to be evaluated at the retarded time, which represents the delay between the photon emission and the time at which the radiation reaches the observer. The first term of Eqn. (2.38) can be neglected in the relativistic regime because of the $1/\gamma^2$ dependence. The radiation rate scales with γ^2 , and the number of photons [50] emitted per electron in every betatron oscillation are,

$$N_{phot} = \frac{2\pi}{9} \alpha_f a_\beta. \quad (2.39)$$

where $\alpha_f = 1/137$ is the fine structure constant [50]. During acceleration, the betatron oscillation amplitude decreases with $\gamma^{-1/4}$. This dependence can be shown by writing down the Hamiltonian for a harmonic oscillator

$$H = \gamma m_e c^2 + \frac{1}{2} \gamma m_e \omega_\beta^2 y^2 = \gamma m_e c^2 + \frac{\omega_p^2}{4} m_e y^2, \quad (2.40)$$

where

$$\begin{aligned}\gamma &= \sqrt{\gamma_z^2 + p_y^2/m_e^2 c^2} \\ \gamma_z &= \sqrt{1 + p_z^2/m_e^2 c^2}.\end{aligned}\quad (2.41)$$

We define r_β through

$$m_e \frac{\omega_p^2}{4} r_\beta^2 = H - \gamma_z m_e c^2. \quad (2.42)$$

If $\gamma_z = \gamma_z(t)$, then

$$m_e \frac{\omega_p^2}{4} 2r_\beta \dot{r}_\beta = \dot{H} - \dot{\gamma}_z m_e c^2. \quad (2.43)$$

Now, since the second term in (2.40) does not depend explicitly on time, we can write

$$\dot{H} = m_e c^2 \frac{\partial \gamma}{\partial t} = m_e c^2 \frac{1}{2} \frac{2\gamma_z \dot{\gamma}_z}{\gamma}, \quad (2.44)$$

Then (2.43) becomes

$$m_e \frac{\omega_p^2}{2} r_\beta \dot{r}_\beta = m_e c^2 \frac{\dot{\gamma}_z}{\gamma} (\gamma_z - \gamma) \frac{(\gamma_z + \gamma)}{(\gamma_z + \gamma)}. \quad (2.45)$$

Using Eqn. (2.41) it becomes

$$m_e \frac{\omega_p^2}{2} r_\beta \dot{r}_\beta = -\frac{\dot{\gamma}_z}{\gamma(\gamma_z + \gamma)} \frac{p_y^2}{m_e}. \quad (2.46)$$

For $\gamma_z^2 \gg \frac{p_y^2}{m_e^2 c^2}$ $\gamma \simeq \gamma_z$ and we can write

$$H \simeq \gamma_z m_e c^2 + \tilde{H}, \quad (2.47)$$

where

$$\tilde{H} = \frac{p_y^2}{2\gamma_z m_e} + \frac{m_e \omega_p^2 y^2}{4} = \frac{m_e \omega_p^2 r_\beta^2}{4}. \quad (2.48)$$

The average kinetic energy

$$\frac{\bar{p}_y^2}{2\gamma_z m_e} = m_e \frac{\omega_p^2}{4} \bar{y}^2 = \frac{\bar{\tilde{H}}}{2}. \quad (2.49)$$

From (2.46), if $\gamma \simeq \gamma_z$, we have

$$m_e \frac{\omega_p^2}{2} r_\beta \dot{r}_\beta = -\frac{\dot{\gamma}_z}{2\gamma_z^2} \frac{p_y^2}{m_e}. \quad (2.50)$$

From Equation (2.48) and (2.49) we have $\frac{r_\beta^2}{\bar{y}^2} = 2$ and using (2.49) in (2.50)

$$m_e \frac{\omega_p^2}{2} r_\beta \dot{r}_\beta = -\frac{\dot{\gamma}_z}{\gamma_z} \frac{m_e \omega_p^2}{4} \bar{y}^2 = -\frac{\dot{\gamma}_z}{\gamma_z} m_e \omega_p^2 \frac{r_\beta^2}{8}, \quad (2.51)$$

which gives

$$\frac{\dot{r}_\beta}{r_\beta} = -\frac{\dot{\gamma}_z}{4\gamma_z} \Rightarrow r_\beta \propto \gamma^{-1/4}. \quad (2.52)$$

The damping of the oscillation amplitude is shown in Figure 2-3.

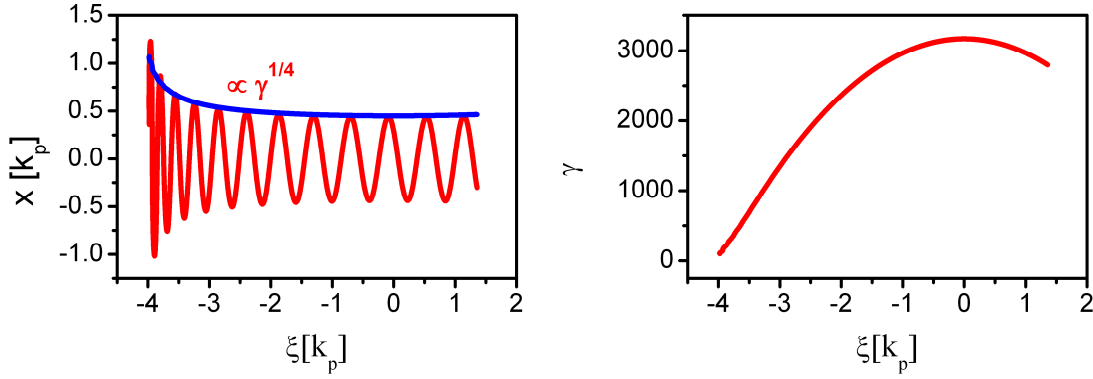


Figure 2-3: Evolution of the electron trajectory (l.h.s.) and of the electron Lorentz factor (r.h.s.) in the bubble regime as calculated analytically assuming a spherical bubble and a plasma density of $2 \times 10^{18} \text{ cm}^{-3}$. The oscillation amplitude (see l.h.s.) evolves as $\gamma^{1/4}$ as expected from (2.52).

2.6 Harmonically Resonant Betatron Motion

The presence of the laser field inside the bubble can dramatically change the electron dynamics. In 1999, Pukhov [51] introduced the concept of an electron-laser resonance in a relativistic channel. This occurs when the laser frequency, as seen by the electrons, equals the betatron frequency, and leads to effective energy exchange between electrons and laser. The electron motion was described in his theory with the equation for a driven oscillator. Starting from Pukhov's work we have investigated the analogous motion in the bubble regime. When the laser partially fills the bubble ($\tau_l \geq R/c$), electrons can experience the laser electromagnetic field, and the total force acting on the electron is given by Eqn. (2.19). If the laser propagates along z and is linearly polarized in y , the vector potential can be written as

$$\vec{A} = \hat{y}A_0 e^{-\frac{(t-z/v_g)^2}{2\tau^2}} e^{-\frac{(x^2+y^2)}{2\sigma^2}} \cos(k_0 z - \omega_0 t). \quad (2.53)$$

Setting $f(\vec{r}, t) = e^{-\frac{(t-z/v_g)^2}{2\tau^2} - \frac{(x^2+y^2)}{2\sigma^2}}$ and $g(z, t) = \cos(\omega_0(t - z/v_p))$, the

corresponding electric field is

$$E_y(\vec{r}, t) = -\partial A_y / \partial t = -A_0 [(\partial f / \partial t) g + f (\partial g / \partial t)], \quad (2.54)$$

where $\partial f / \partial t = -(t - z / v_g) f / \tau^2$, and $\partial g / \partial t = -\omega_0 \sin(\omega_0 (t - z / v_p))$. The

components of the magnetic field are

$$\begin{aligned} B_x(\vec{r}, t) &= -\partial A_y / \partial z = -A_0 [(\partial f / \partial z) g + f (\partial g / \partial z)] \\ B_y(\vec{r}, t) &= 0 \\ B_z(\vec{r}, t) &= \partial A_y / \partial x = A_0 (\partial f / \partial x) g \end{aligned} \quad , \quad (2.55)$$

with

$$\begin{aligned} \partial f / \partial x &= -x f / \sigma^2 \\ \partial f / \partial z &= (t - z / v_g) f / (v_g \tau^2) = -(\partial f / \partial t) / v_g \\ \partial g / \partial z &= (\omega_0 / v_p) \sin(\omega_0 (t - z / v_p)) = -(\partial g / \partial t) / v_p \end{aligned} \quad . \quad (2.56)$$

The components of the Lorentz force are

$$\begin{aligned} F_{Lx}(\vec{r}, t) &= -e v_y B_z = -e A_0 v_y (\partial f / \partial x) g \\ F_{Ly}(\vec{r}, t) &= -e E_y - e (v_z B_x - v_x B_z) = e (\partial A_y / \partial t + v_z \partial A_y / \partial z + v_x \partial A_y / \partial x) \\ &= e A_0 [(\partial f / \partial t + v_x \partial f / \partial x + v_z \partial f / \partial z) g + f (\partial g / \partial t + v_z \partial g / \partial z)] \\ &= e (d A_y / dt - v_y \partial A_y / \partial y) \\ F_{Lz}(\vec{r}, t) &= e v_y B_x = -e v_y A_0 [(\partial f / \partial z) g + f \partial g / \partial z] \end{aligned} \quad . \quad (2.57)$$

Writing the transverse component of the left term of Eqn. (2.20) as

$$F_y = \frac{dp_y}{dt} = \frac{d}{dt}(m_e \gamma \dot{y}), \quad (2.58)$$

Using (2.20), (2.31) and (2.32) we obtain

$$\ddot{y} + \Gamma \dot{y} + \omega_\beta^2 y = \frac{F_{Ly}}{m_e \gamma}. \quad (2.59)$$

This is the equation for a damped driven harmonic oscillator, where $\Gamma = \dot{\gamma}/\gamma$ is the damping factor due to the relativistic mass increase [52, 53]. The γ -dependence of ω_β leads to a shift in the resonance on a slow timescale, and anharmonic motion on a fast timescale. The laser frequency can shift by several percent to ω'_0 by photon deceleration [54] and is Doppler shifted to $\tilde{\omega} = \omega'_0 \left(1/(2\bar{\gamma}_z^2) + 1/(2\gamma_g^2) \right)$, where γ_g is the Lorentz factor for the group velocity of the segment of the laser pulse interacting with the electrons in the bubble. The oscillation amplitude grows considerably when $\Gamma < \omega_\beta$ and the laser field is in resonance with a harmonic of the betatron oscillation, $\tilde{\omega} = l \omega_\beta$, where l is the harmonic number. Γ vanishes at dephasing ($z \simeq L_d$) when $\dot{\gamma} \rightarrow 0$ and the betatron amplitude suddenly increases. At this point both the radiation rate and γ are at their maximum. The harmonically resonant betatron regime predicted analytically is confirmed by simulations where it is clearly observed as shown in Figure 2-4 with simulation performed using the OSIRIS PIC code [41] using as input the

parameters (plasma density and laser normalized vector potential) of the experiment reported in the following chapter.

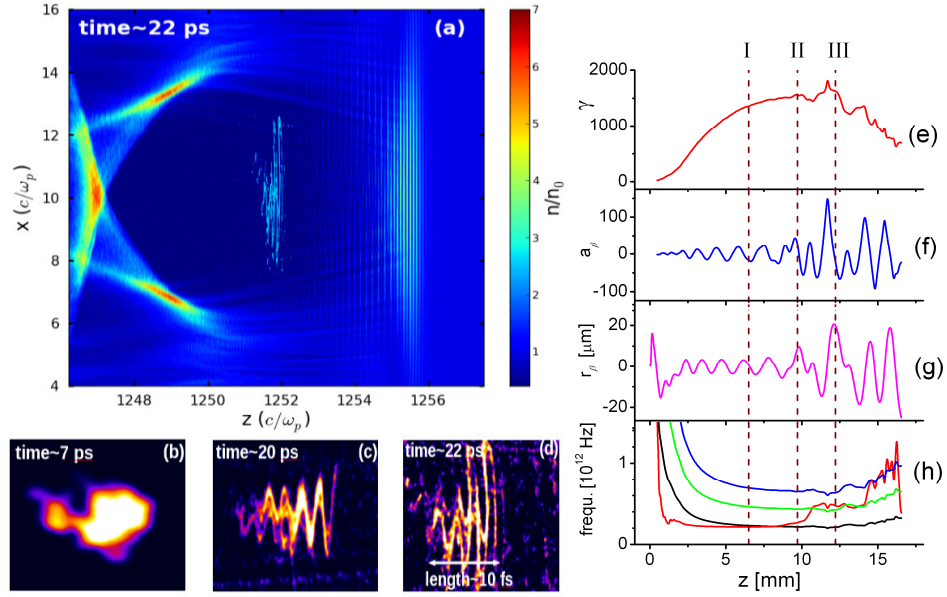


Figure 2-4: OSIRIS simulations of laser-driven betatron oscillations: l.h.s.: a) snapshot of electron distribution, and electron beam trajectories for the non resonant (b), weakly resonant (c) and strongly resonant case (c). R.h.s.: trajectories of one electron showing (e) evolution of γ , (f) a_β , (g) r_β , and (h) frequencies

Figure 2-4 synthesizes the essence of the harmonically resonant regime. Starting from Figure 2-4b electrons, initially injected at the rear of the “bubble”, perform independent betatron oscillations arising from their initial transverse position and momentum. The amplitude of these “free” oscillations is damped due to the longitudinal acceleration (*i.e.* $\Gamma > 0$), see Eqn. (2.52) and Figure 2-3. At dephasing, $\Gamma \approx 0$, resonance occurs (*i.e.* the phase $\approx \pi$) resulting in rapid growth of the betatron amplitude

until $r_\beta \approx R$, as shown in Figure 2-4g. Since the laser phase is the same for all electrons at a given longitudinal position, these forced oscillations have identical phases and their trajectories coalesce [55], as shown by the well-defined oscillations in y observable in Figure 2-4c-d. As the betatron frequency decreases with increasing axial momentum, it stays close to the Doppler-downshifted laser frequency for only a short time, and then slips to one half, then one third, of this frequency (and could carry on towards further subharmonics if γ kept growing). In each case, the growing oscillation amplitude causes the Lorentz factor corresponding to the axial velocity to increase more slowly than the one corresponding to the momentum. This allows the resonance to persist for a finite time before it is lost and the betatron frequency slips towards the next laser subharmonic, which is the same as a harmonic of the betatron frequency (Figure 2-4h). Resonance with the fundamental cannot be maintained continuously as γ increases. The resonance with the fundamental betatron frequency by itself is not sufficient to produce a noticeable effect on a_β . Harmonic resonance is required to allow a_β to grow to large values. Therefore, resonance with the fundamental betatron frequency is quickly lost. The novelty of our approach is the inclusion of the damping term, which was not included in Pukhov's theory [51]. The damping factor adds a nonlinearity that introduces both odd and even harmonics and allows the resonance to persist between the laser frequency and harmonics of the betatron frequency: electrons can be driven at harmonics of the betatron frequency because of anharmonic motion arising from variations of γ . When out of resonance, the laser field has little effect on the betatron motion and electrons retain both their high amplitude and coalesced

trajectories. Eventually, electrons begin to decelerate and/or leave the plasma at an arbitrary phase of the high-amplitude oscillation, with only a residual phase space spread, *i.e.* emittance is conserved from the original “free” oscillation and is similar to that just after injection, whereas the high-amplitude oscillation can lead to shot-to-shot pointing variations. In a realistic experiment, injection occurs after a delay that depends on the evolution of the laser beam in the plasma medium, which in turn determines the distance at which injection occurs. This is a highly nonlinear process that depends on both laser and plasma properties [40, 42, 54]. Therefore the accelerator length (*i.e.* injection to end of depletion length or plasma medium) can vary. As a result, for a fixed acceleration length (limited by the depletion length or plasma medium length), the wakefield acceleration structure vanishes either before dephasing (I - illustrated in Figure 2-4), at dephasing (II) or beyond dephasing (III). This accounts for the variability of the electron beam properties from the LWFA. However, close to dephasing r_β and a_β can grow substantially without an appreciable change in γ , as can be seen in Figure 2-4.

2.7 Conclusions

We have shown, in analytical and numerical studies that during LWFA in the bubble regime the presence of the laser can strongly influence the dynamics of electrons. Electrons travelling inside a bubble filled by the laser pulse can enter into resonance

with the laser field. Hitherto, only resonance between the laser frequency, at the fundamental betatron frequency had been investigated [51, 56]. Here we have shown how the nonlinearity due to the relativistic mass increase gives rise to a harmonically resonant motion. Resonance between the laser frequency and harmonics of the betatron frequency can occur, and when this happens both r_β and a_β increase rapidly. High r_β and a_β values correspond to a high critical frequency of the betatron spectrum and an enhancement of the number of photons emitted per electron. The betatron radiation spectrum emitted in the harmonically resonant conditions can scale up to the MeV range, which strongly enhances the source brightness. The next chapter describes the experiment carried out to demonstrate and prove the harmonically resonant regime. This paves the way to a new field of applications of this novel ultra-compact bright tuneable X- and gamma-ray source.

References

1. Strickland D. and Mourou G., "Compression of Amplified Chirped Optical Pulses", *Opt. Commun*, **56**, 219 (1985)
2. Shvets G. and Fisch N.J., "Superradiant Amplification of an Ultrashort Laser Pulse in a Plasma by a Counterpropagating Pump", *Phys. Rev. Lett.*, **81**(22), 4879 (1998)
3. Trines R.M.G.M. and al. e., "Simulations of efficient Raman amplification into the multipetawatt regime", *Nat. Phys.*, **7**, 87 (2011)
4. Vieux G., *et al.*, "Chirped pulse Raman amplification in plasma ", *New J Phys*, **13**, 063042 (2011)

5. Tajima T. and Dawson J.M., "Laser Electron Accelerator", *Phys. Rev. Lett.*, **43**(4), 267 (1979)
6. Modena A. and et.al., "Electron acceleration from the breaking of relativistic plasma waves", *Nature*, **377**, 606 (1995)
7. Mangles S.P.D. and al. e., "Electron Acceleration from the Breaking of Relativistic Plasma Waves", *Nature*, **431**, 535 (2004)
8. Geddes C.G.R. and al. e., "High Quality Electron Beams from a Laser Wakefield Accelerator Using Plasma-Channel Guiding", *Nature*, **431**, 538 (2004)
9. Faure J. and al. e., "A Laser-Plasma Accelerator Producing Monoenergetic Electron Beams", *Nature*, **431**, 541 (2004)
10. Leemans W.P. and al. e., "GeV Electron Beams from a Centimetre-Scale Accelerator", *Nat. Phys.*, **2**, 696 (2006)
11. Brunetti E. and al. e., "Low emittance, high brilliance relativistic electron beams from a laser-plasma accelerator", *Phys. Rev. Lett.*, **105**, 215007 (2010)
12. Wiggins S.M. and al. e., "High quality electron beams from a laser wakefield accelerator", *Plasma Phys. Control. Fusion* **52**, 124032 (2010)
13. Lundh O., *et al.*, "Few Femtosecond, Few Kiloampere Electron Bunch Produced by a Laser-Plasma Accelerator", *Nat. Phys.*, **7**, 219 (2011)
14. Esarey E. and al. e., "Physics of laser-driven plasma-based electron accelerators", *Rev. Mod. Phys.*, **81**, 1229 (2009)
15. Quesnel B. and Mora P., "Theory and simulation of the interaction of ultraintense laser pulses with electrons in vacuum", *Phys. Rev. E*, **58**(3), 3719 (1998)
16. Sun G.-Z. and al. e., "Self-focusing of short intense pulses in plasmas", *Phys. Fluids*, **30**(2), 526 (1987)
17. Butler A., Spence D.J., and Hooker S.M., "Guiding of High-Intensity Laser Pulses with a Hydrogen-Filled Capillary Discharge Waveguide", *Phys Rev Lett*, **89**(18), 185003 (2002)

18. Nikitin S.P., Alexeev I., Fan J., and Milchberg H.M., "High efficiency coupling and guiding of intense femtosecond laser pulses in preformed plasma channels in an elongated gas jet", *Phys Rev E*, **59**(4), R3839 (1999)
19. Kim K.Y., Alexeev I., Fan J., Parra E., and Milchberg H.M., "Plasma Waveguides: Addition of End Funnel and Generation in Clustered Gases", *AIP Conference Proceedings*, **647**, 646 (2002)
20. Esarey E., Sprangle P., Krall J., and Ting A., "Self-focusing and guiding of short laser pulses in ionizing gases and plasmas", *Quantum Electronics, IEEE Journal of*, **33**(11), 1879 (1997)
21. Spence D.J., Butler A., and Hooker S.M., "First demonstration of guiding of high-intensity laser pulses in a hydrogen-filled capillary discharge waveguide ", *Journal of Physics B: Atomic, Molecular and Optical Physics*, **34**(21), 4103 (2001)
22. Hooker S.M., *et al.*, "GeV Plasma Accelerators Driven in Waveguides ", *Plasma Phys. Control. Fusion*, **49**, B403 (2007)
23. Bobrova N.A., Esaulov A.A., Sakai J.I., Sasorov P.V., Spence D.J., Butler A., Hooker S.M., and Bulanov S.V., "Simulations of a hydrogen-filled capillary discharge waveguide", *Phys Rev E*, **65**(1), 016407 (2001)
24. Jaroszynski D.A., *et al.*, "Radiation sources based on laser-plasma interactions", *Philos T Roy Soc A*, **364**(1840), 689 (2006)
25. Wiggins S.M., Reijnders M.P., Abuazoum S., Hart K., Welsh G.H., Issac R.C., Jones D.R., and Jaroszynski D.A., "Note: Femtosecond laser micromachining of straight and linearly tapered capillary discharge waveguides ", *Rev Sci Instrum*, **82**(9), 096104 (2011)
26. Durfee C.G., III and Milchberg H.M., "Light pipe for high intensity laser pulses", *Phys Rev Lett*, **71**(15), 2409 (1993)
27. Thomas A.G., *et al.*, "Effect of laser-focusing conditions on propagation and monoenergetic electron production in laser-wakefield accelerators", *Phys Rev Lett*, **98**(9), 095004 (2007)

28. Ralph J.E., Marsh K.A., Pak A.E., Lu W., Clayton C.E., Fang F., Mori W.B., and Joshi C., "Self-Guiding of Ultrashort, Relativistically Intense Laser Pulses through Underdense Plasmas in the Blowout Regime", *Phys Rev Lett*, **102**(17), 175003 (2009)
29. Gorbnnov L.M. and Orsanov V.I., "Excitation of plasma waves by an electromagnetic wave packet", *Zh. Eksp. Teor. Fiz.*, **93**, 509 (1987)
30. Sprangle P., Esarey E., Ting A., and Joyce G., "Laser wakefield acceleration and relativistic optical guiding", *Appl. Phys. Lett.*, **53**, 2146 (1988)
31. Esarey E., Ting A., Sprangle P., and Joyce G., "The laser wakefield accelerator", *Comments Plasma Phys. Controlled Fusion*, **12**, 191 (1989)
32. Joshi C. and al. e., "Ultrahigh gradient particle acceleration by intense laser-driven plasma density waves", *Nature*, **311**, 525 (1984)
33. Krall J. and al. e., "Enhanced acceleration in a self-modulated-laser wake-field accelerator", *Phys. Rev. E*, **48** (1993)
34. Krall J., Ting A., Esarey E., and Sprangle P., "Enhanced acceleration in a self-modulated-laser wake-field accelerator", *Phys Rev E*, **48**(3), 2157 (1993)
35. Decker C.D. and al. e., "The evolution of ultra-intense, short-pulse lasers in underdense plasmas", *Phys. Plasmas*, **3**, 2047 (1996)
36. Akhiezer A.I. and Polovin R.V., *Zh. Eksp. Teor. Fiz.*, **30**, 915 (1956)
37. Esarey E. and Pilloff M., "Trapping and acceleration in nonlinear plasma waves", *Phys. Plasmas*, **2**, 1432 (1995)
38. Katsouleas T. and Mori W.B., "Wave-Breaking Amplitude of Relativistic Oscillations in a Thermal Plasma", *Phys. Rev. Lett.*, **61**, 90 (1988)
39. Kruer W.L., "Wavebreaking amplitudes in warm, inhomogeneous plasmas ", *Phys. Fluids*, **22**, 1111 (1979)
40. Pukhov A. and Meyer-Ter-Vehn J., "Laser wake field acceleration: the highly non-linear broken wave regime", *Appl. Phys. B*, **74**, 355 (2002)
41. Fonseca R.A., "Lectures Notes", *Comput. Sci.*, **2331**, 9 (2002)

42. Lu W., Tzoufras M., and Joshi C., "Generating multi-GeV electron bunches using single stage laser wakefield acceleration in a 3D nonlinear regime", *Phys. Rev. ST- Accel. Beams*, **10**, 061301 (2007)
43. Kostyukov I., Pukhov A., and Kiselev S., "Phenomenological theory of laser-plasma interaction in "bubble" regime", *Phys Plasmas*, **11**(11), 5256 (2004)
44. Jackson J.D., *Classical Electrodynamics*, ed. J. Wiley and Son New York. (1999)
45. Lu W., Huang C., Zhou M., Mori W.B., and Katsouleas T., "Nonlinear theory for relativistic plasma wakefields in the blowout regime", *Phys Rev Lett*, **96**(16), 165002 (2006)
46. Katsouleas T., Wilks S., Chen P., Dawson J.M., and Su J.J., "Beam Loading in Plasma Accelerators", *Part. Accel.*, **22**, 81 (1987)
47. Esarey E., Shadwick B.A., Catravas P., and Leemans W.P., "Synchrotron radiation from electron beams in plasma-focusing channels", *Phys Rev E*, **65**(5), 056505 (2002)
48. Kostyukov I., Kiselev S., and Pukhov A., "X-ray generation in an ion channel", *Phys Plasmas*, **10**(12), 4818 (2003)
49. Whittum D.H., "Electromagnetic-Instability of the Ion-Focused Regime", *Phys Fluids B-Plasma*, **4**(3), 730 (1992)
50. Duke P., *Synchrotron Radiation: Production and Properties*: Oxford Science Publications. (2008)
51. Pukhov A., Sheng Z.M., and Meyer-ter-Vehn J., "Particle Acceleration in Relativistic Laser Channels", *Phys Plasmas*, **6**(7), 2847 (1999)
52. Nam I., Hur M.S., Uhm H.S., Hafz N.A.M., and Suk H., "Controlling the Betatron Oscillations of a Wakefield-Accelerated Electron Beam by Temporally Asymmetric Laser Pulses", *Phys Plasmas*, **18**(4), 043107 (2011)
53. Cipiccia S., *et al.*, "Gamma-Rays from Harmonically Resonant Betatron Oscillations in a Plasma Wake", *Nat Phys*, **7**(11), 867 (2011)
54. Reitsma A.J.W., Trines R.M.G.M., Bingham R., Cairns R.A., Mendonca J.T., and Jaroszynski D.A., "Photon kinetic modeling of laser pulse propagation in underdense plasma", *Phys Plasmas*, **13**(11), 113104 (2006)

55. Nemeth K., Shen B.G., Li Y.L., Shang H.T., Crowell R., Harkay K.C., and RCary J., "Laser-Driven Coherent Betatron Oscillation in a Laser-Wakefield Cavity", *Phys Rev Lett*, **100**(9), 095002 (2008)
56. Kneip S., *et al.*, "Observation of Synchrotron Radiation from Electrons Accelerated in a Petawatt-Laser-Generated Plasma Cavity", *Phys Rev Lett*, **100**(10), 105006 (2008)

Chapter 3

3.1 Introduction

In the laser wakefield accelerator transverse oscillations of electrons in the plasma bubble trailing the laser pulse emit synchrotron-like radiation known as betatron radiation. As pointed out in Chapter 2, the properties of the betatron radiation strongly depend on the electron acceleration process. Recent experimental results have shown that this radiation is bright, spatially coherent [1] and tuneable in the keV range, with a peak energy limited to 1-10 keV. However, as discussed in Chapter 2, the interaction of electrons with the laser pulse can amplify the betatron motion leading to an increase in the energy of emitted photons, which can extend to several MeVs.

In this Chapter we present the first experimental evidence of harmonic-betatron resonance [2] and show that the betatron amplitude is resonantly enhanced when electrons interact with the laser pulse [3, 4] and, at higher energies, this leads to orders of magnitude increase in the photon energy. Resonant betatron emission has been investigated by simultaneously monitoring the electron beam properties using an electron energy spectrometer with LANEX [5] screens and image plates [6], while

simultaneously monitoring the x-ray photon properties using image plates (IP) and/or an x-ray semiconductor detector. During the investigation three distinct sets of data (indicated by the lines I, II & II in Figure 2.3) have been recorded. In all cases the recorded electron energy is around 700 MeV. Furthermore, the onset of injection depends on the detailed evolution of the mode structure in the plasma waveguide, which in turn depends on the timing of the discharge and relativistic effects. In the first experiment, carried out at a density of $\approx 1.6 \times 10^{18} \text{ cm}^{-3}$, we studied the highly damped stage (I) by measuring the photon energy peak and angular divergence using cut-off filters and image plates. This has been followed by an investigation, carried out at a density of $\approx 2 \times 10^{18} \text{ cm}^{-3}$, of the weakly and strongly resonant regimes (II & III), by recording single-shot spectra of the gamma-ray spectra. To enable evaluation of the brilliance, the source size has been estimated using phase-contrast imaging techniques. The investigation and experimental evidence of the three different regimes is explained in the following sections. We measure 10^8 gamma-ray photons per pulse with spectra peaking between 20 and 150 keV, and a peak brilliance of 10^{23} photons/s mrad² mm² 0.1%bandwidth, with 10^7 photons emitted between 1 and 7 MeV. Femtosecond duration gamma rays may find a use in medical imaging, isotope production, homeland security and potentially probing nuclear phenomena [7]. The experimental challenges, solutions, setup description and results are presented in the following sections.

3.2 Broadband high flux single shot measurements of betatron radiation

Despite the simplicity of the LWFA concept, the electron motion is determined by a highly nonlinear process that depends on the interplay of both plasma and laser parameters. Injection, beam loading, dephasing and depletion length can be strongly effected by shot-to-shot variation of density or laser parameters with a consequent variation of the electron beam properties. The betatron radiation, besides being a new promising light source, is a powerful tool that also gives an insight into the acceleration mechanism and electron beam properties [8]. The ability to detect and characterize the betatron spectrum on every shot can open the door to a better understanding of its role in determining the acceleration process, which is important in the development of completely tuneable, compact electron and light sources. As pointed out in the previous chapter, depending on the electron energy at which resonance occurs, the energy range of the radiation can span from a few keV to several MeV. Over this range of energies the number of photons emitted per electron can increase by an order of magnitude. The wide energy range and high flux makes the betatron radiation spectrum hard to measure directly in a single shot measurement as would be preferred. To allow a broad energy range one solution is to use different spectrometers to measure spectra in different energy windows and then reconstructing the whole spectrum. However, for high flux the problem is more complex. In principle metal filters of different materials and thicknesses can be used to attenuate the flux to low levels while defining different band-passes to

reconstruct the spectrum. However, the use of metal filters results in a loss of information: the low energy tail of the incoming spectrum is cut by the strong absorption of the material at the k-edge energy, which corresponds to the energy gap between the innermost and second electron orbitals of the atom making up the filter. Atoms act as strong absorbers at this energy. An alternative method relies on the natural divergence to attenuate the beam, but this requires tens of meters in the experimental area. However, as we will show, Compton scattering can be used to compress the energy spectrum and attenuate the flux simultaneously. When combined with a suitable single shot energy resolving detector, spectra can be measured up to several MeV

3.2.1 Compton Scattering

Compton scattering occurs when an x- or γ - ray photon interacts with an electron. The incoming photon is deflected after interacting with the electron by an angle θ , and a portion of its energy is transferred to the electron, which is assumed to be initially at rest (Figure 3-1), conserving the total energy and momentum.

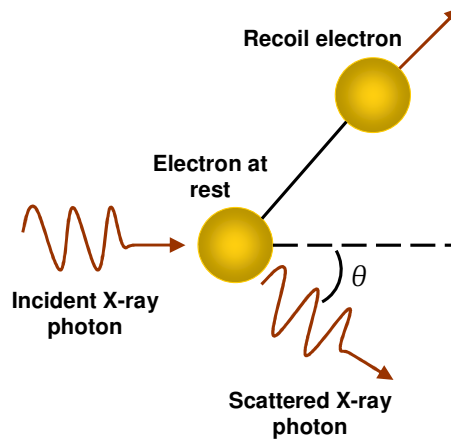


Figure 3-1: Compton scattering scheme.

The energies of incoming and scattered photons, E and E' respectively, are related to the scattering angle by the well known relation [9]:

$$E' = \frac{E}{1 + \frac{E}{m_e c^2} (1 - \cos \theta)} \quad (3.1)$$

This formula shows how the energy of the scattered photon, for a fixed energy of the incoming photon decreases while the angle increases. Moreover, the cross section of the process varies with both the angle and the energy of the incoming photon. The Klein-Nishina formula gives the differential scattering cross-section $d\sigma/d\Omega$ for Compton scattering:

$$\frac{d\sigma}{d\Omega} \propto Z * P(E, \vartheta)^2 (P(E, \vartheta) + P(E, \vartheta)^{-1} - 1 + \cos^2 \vartheta), \quad (3.2)$$

$$P(E, \vartheta) = \frac{1}{1 + \frac{E}{m_e c^2} (1 - \cos \vartheta)},$$

The dependence of the scattered photon energy on the incoming photon energy for different angles and of the differential cross section on the angle for different incoming photon energies are shown in Figure 3-2. The Compton effect contracts and downshifts the incoming photon spectrum and therefore can be used to extend both energy and flux range of an x-ray detector. The Compton effect is already harnessed in physics to characterize light sources: i.e. in astrophysics, Compton telescopes [10] allow the gamma-ray energy and the source position of incoming gamma-ray photons to be determined. A Compton telescope utilises two detectors, with one acting as a Compton scattering centre where the Compton-produced electron is detected, while the other detects the scattered photons. From the energy deposited in each detector, it is possible to reconstruct the energy of the incoming radiation, and the scattering angle gives information on the source position. Taking inspiration from this technique we have adapted it to our particular requirements for the betatron experiment. In our case the source position is known and therefore the detection scheme is modified to a single detector setup: the first electron detector is not required anymore and is replaced by a scattering centre, while the second detector detects effectively a collimated beam of photons at a fixed angle with respect to the scattering centre. Using this information it is possible to directly calculate the energy of the incoming photon. The scattered photon energy is downshifted by an energy difference that depends on the angle. By observing

at an appropriate angle, it is possible to indirectly measure the photon energy outside the nominal detection range of the detector/spectrometer. In addition to downshifting, the Compton effect also contracts the spectrum, which reduces the resolution, as shown in Figure 3-2 (a). Moreover, the cross-section of the Compton effect (3.2) decreases with increasing scattering angle [Figure 3-2(b)]. Hence, the Compton effect also effectively attenuates the radiation flux incident on the detector. Depending on the type of measurement there is a trade-off between the energy range, spectral resolution and signal intensity.

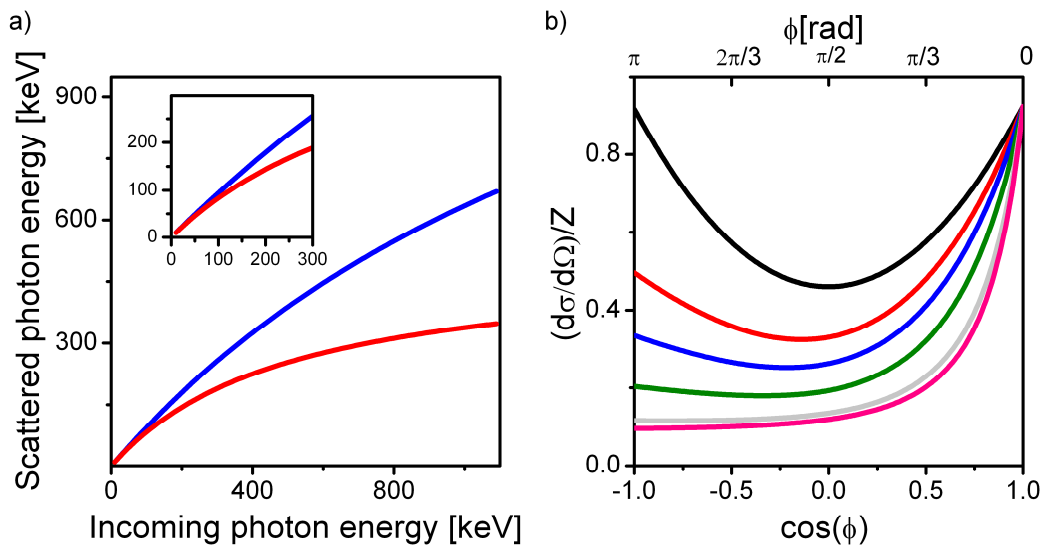


Figure 3-2: a) Compton side scattered photon energy plotted as a function of the energy of the incoming radiation, for different incident angles: $\pi/4$ (blue line), $\pi/2$ (red line), $3\pi/4$ (green line). The inset graph shows a zoom up to 300 keV. b) angular cross section vs angle for different incoming photon energies: 1 keV (black line), 100 keV (red line), 200 keV (blue line), 400 keV (green line) 800 keV (grey line), 1000 keV (pink line).

3.2.2 A Pixel Matrix Semiconductor as an X-ray Spectrometer

Having found a potential configuration for a single shot betatron radiation detector, the other challenge is to choose an appropriate x-ray spectrometer that will work in a noisy electromagnetic environment, and in single-shot mode to reconstruct the whole spectrum. Even if the Compton effect contracts the energy window to use a single detector, keeping the setup as simple as possible, this still needs to have a quite large energy range, from tens to hundreds of keV. Moreover, to reconstruct the whole spectrum in a single-shot mode the detector needs to have the capability of detecting and discriminating all the photons. The number of detected photons needs to be high enough to guarantee a proper spectrum reconstruction; this implies a large number of pixels.

Pixel matrix semiconductor detectors are good candidates for this kind of application. Semiconductor pixel detectors have an excellent spatial resolution and allow high signal-to-noise ratio measurements to be made, which has enabled them to become key components in large-scale particle tracking detection systems for high energy physics experiments [11]. Technological developments have widened the potential application of these kinds of detectors allowing them to be used for x-ray imaging and spectroscopy. Examples of these type of detectors are Medipix [12, 13] and Timepix [14], which are pixelated detectors, developed at CERN, based on complementary metal–oxide–semiconductor (CMOS) technology.

Timepix, in particular is a promising and versatile detector because it can work in a spectrometer mode. Because of this it is used for a wide range of applications from the life sciences to material studies and, as shown in the next sections, it has properties that make it a good candidate for our betatron source characterisation experiment.

3.2.3 Medipix and Timepix

Medipix is a hybrid pixelated semiconductor detector that detects in a single photon counting mode. It consists of a 256 x 256 matrix of identical pixels, each occupying an area of 55 x 55 μm^2 . When a high energy particle or photon interacts with the detector material, it deposits energy and generates electron-hole pairs. The charge produced is then collected by electrodes and the signal processed by miniaturized integrated circuit chips (one for each pixel) that are connected to the active material by a solder bump bond, as shown in Figure 3-3. By exploiting 6-metal, 0.25 μm , CMOS transistor technology, a large number of interconnected layers are produced. Each chip contains a charge preamplifier, two identical discriminators to select the energy window of interest and a shift register. The miniaturization provides a spatial resolution comparable with simpler integrating readout systems, while maintaining a very high signal to noise ratio [15].

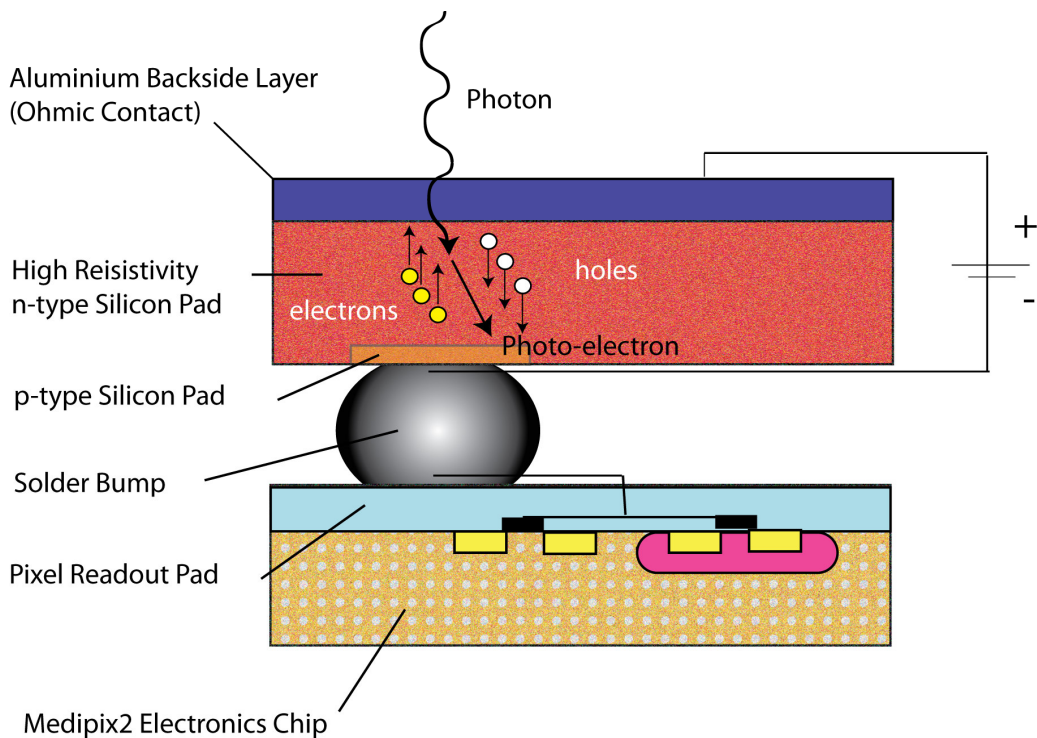


Figure 3-3: Schematic diagram of a Medipix pixel. The detector material, in this case silicon, is connected by a solder bump-bond to the underlying electronic chip pad. In this scheme the incoming photon interacts with the semiconductor layer via photoelectric effect generating a photo-electron which in turn deposits energy in the form of electron-hole pairs.

Timepix [12] is an evolution of Medipix. It has a single absorption threshold and each pixel has two working states: when the shutter signal is high data are shifted from pixel to pixel. When the shutter signal is low the pixel counter can be incremented in three different ways: event counting, arrival time, and “time-over-threshold” (TOT). In the event counting mode, or Medipix mode, each event above threshold increments the counter by 1 and the counter counts the number of incoming particles. In arrival time mode the counter counts from the time of activation of the discriminator until the shutter

is set to high, thus giving it a measure of the arrival time of the incoming particle. In the TOT mode the counter is incremented continuously while the signal is above a threshold allowing a direct energy measurement for each pixel. It is in this TOT mode that Timepix shows promising use, such as x-ray spectrometry [14], when the photon flux per pixel is less than one. It is worth noting that a single x-ray photon can generate signals in many adjacent pixels because charge produced by the particle can diffuse during the collection process. The size of the cluster of pixels into which diffusion occurs depends on the depth of the particle-semiconductor interaction and the properties of the radiation, semiconductor material and the bias voltage. The bias voltage determines the speed of collection: the slower the speed, the larger the diffusion. Therefore, for a proper reconstruction of the radiation spectrum, it is necessary to take into account the charge sharing effect and to add up the energy deposited in each pixel cluster to determine the total energy deposited by a photon.

In general the robustness of the device allows it to function in an electromagnetically noisy environment [15] and the fine pixelation of the active area leads to a high spatial resolution. This, combined with the excellent signal-to-noise ratio, has stimulated our interest in using Timepix for characterising hard X-ray spectra in single-shot applications. To determine if Timepix is actually suitable for betatron radiation experiments we have investigated two different semiconductor materials with different thicknesses, bump-bonded onto the Timepix readout chip: 300 μm Si and 1 mm CdTe [16]. The larger atomic number of the latter results in a better detection efficiency at higher energy, at the expense of resolution due mainly to the charge sharing

effect [17], which also sets a limit to the cell size and therefore limits the scale of miniaturisation and the maximum overall flux that can be sustained in the single photon per pixel mode.

3.2.3.1 Timepix Characterisation

In the literature there is no published information on the behaviour and characterisation of Timepix under MeV photon irradiation. To prove Timepix is suitable as a betatron radiation detector, we have characterized the response of the Timepix detectors under photon irradiation from a few keV up to more than 1 MeV. The first step performed was to investigate the response of the detector using the calibrated x-ray and gamma-ray sources reported in Table 3-1. The data corresponds to a 300 μm thick Si Timepix detector, but a similar analysis has been conducted for the 1 mm thick CdTe detector.

Source	Photon Energy [keV]
Am ²⁴¹	13.9 keV, 26.3 keV , 59.5 keV
Cs ¹³⁷	661.7 keV
Co ⁶⁰	1173.2 keV, 1332.5 keV
Na ²²	511keV, 1274.5 keV

Table 3-1: Laboratory sources used for calibration of the Timepix detectors

The first source used to calibrate and verify the quality of the reconstructed spectra was Americium-241 (Am-241). Am241 decay produces both x-rays and 5.5 MeV alpha particles. A cardboard layer and a 2 mm thick copper (Cu) sheet were placed between

the source and the detector to block the alpha particles. The X-rays from Am241 also cause the emission of Cu k-alpha photons, which can be used as a further reference for calibration. The recorded spectrum is shown in Figure 3-4.

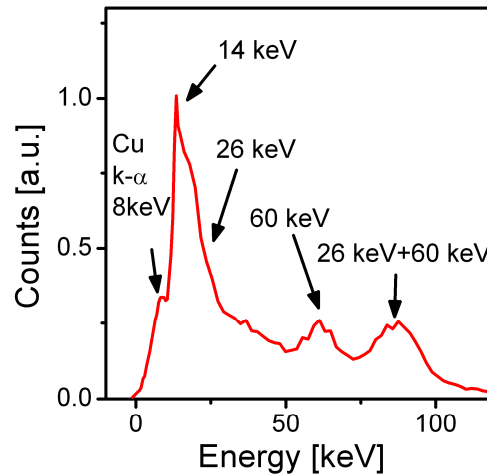


Figure 3-4: Laboratory source Am-241 spectrum and k-alpha from copper (Cu) recorded with the 300 μm Si Timepix detector.

To explore the high energy range we irradiated the detector with photons emitted by Cesium-137 (Cs-137), Sodium-22 (Na-22) and Cobalt-60 (Co-60). As shown in the recorded spectra of Figure 3-5a, for all three sources, the detector does not detect photons in the range 511-1333 keV: the photons are too energetic to be stopped inside the 300 μm silicon bulk. All three spectra feature a smooth high energy tail but Na-22 and Co-60 produce a pronounced peak at about 200 keV, with the strongest peak obtained from Co-60, that emits two lines in the MeV range, at 1172 and 1332 keV.

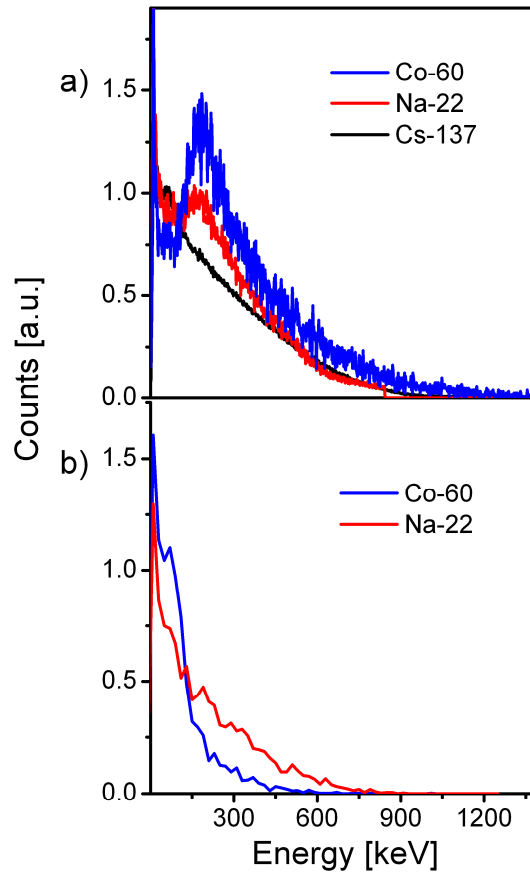


Figure 3-5: a) Laboratory source Cs-137, Na-22 and Co-60 spectra recorded with the 300 μm Si Timepix detector. b) GEANT4 simulation results obtained for the simple monolayer model under Co-60 and Na-22 irradiation. For the Co-60, the results are obtained by summing the contribution from two different photon energies, 1332 keV and 1172 keV to reproduce the double emission line of the source.

To understand how the photons are detected inside Timepix and how the signal is formed, we have modelled the detector using GEANT4 [18]. GEANT4 is a simulation toolkit written in object oriented C++ programming language that describes the passage

of elementary particles through matter. It implements a complete range of functions including geometry of the system, description of materials involved, tracking of particles, external electromagnetic fields and physics models to handle particle interaction with matter over a wide energy range. It has been used for many different applications such as particle physics, nuclear physics, medical physics and accelerator design.

We have simulated Timepix using GEANT4, modelling its geometry as a simple 300 μm thick mono-layer of Silicon. To reconstruct the signal we have assumed that the detector was able to discriminate each photon (single photon per pixel working mode). The signal was reconstructed from the energy deposited in the bulk by each primary photon coming from the source and by secondary particles generated by the primary photons. We have simulated the irradiation for both the Na-22 and Co-60 laboratory sources. The simulated signals, shown in Figure 3-5b, display a long tail without reproducing the peak observed at 200 keV. This suggests that the silicon monolayer model is not sufficiently comprehensive to explain the signal formation in the pixel detector. While low energy photons are completely stopped inside the active semiconductor, higher energy photons are not and therefore the semiconductor layer probably only plays a partial role in signal formation, while the effect of the surrounding material should also be taken into account.

To reproduce the experimental behaviour of Timepix we added a high Z substrate layer to the back of the Si bulk detector layer in our simulation to account for the

electronic chip and readout pad components (as shown in Figure 3-3). We then studied the device response while varying the “effective” atomic number Z and thickness of the back layer and photon energy, as shown in Figure 3-6a ($Z = 100$ is the maximum value allowable in GEANT4). Z gives the effective total scattering cross-section and represents the whole multi-element back layer. The main effect of adding the back layer is apparent in all three sets of simulated spectra, which clearly shows a peak at ~ 200 keV for $Z > 50$ [Figure 3-6(a)], for a thickness > 20 μm [Figure 3-6(b)] and photon energy > 1 MeV [Figure 3-6(c)]. Note the saturation of the peak signal for both thickness > 100 μm and photon energy > 1.3 MeV. Important information on signal formation in Timepix can therefore be deduced from these simulations. When the energy of the photons is only a few tens of keV, the main part of the energy is deposited in the silicon. However, when the energy increases to the MeV range, it is the back layer that mainly interacts with the radiation via Compton scattering. The total signal recorded by Timepix is a sum of the energy deposited directly in the Si bulk plus a fraction of the energy scattered in the back layer mainly via Compton scattering.

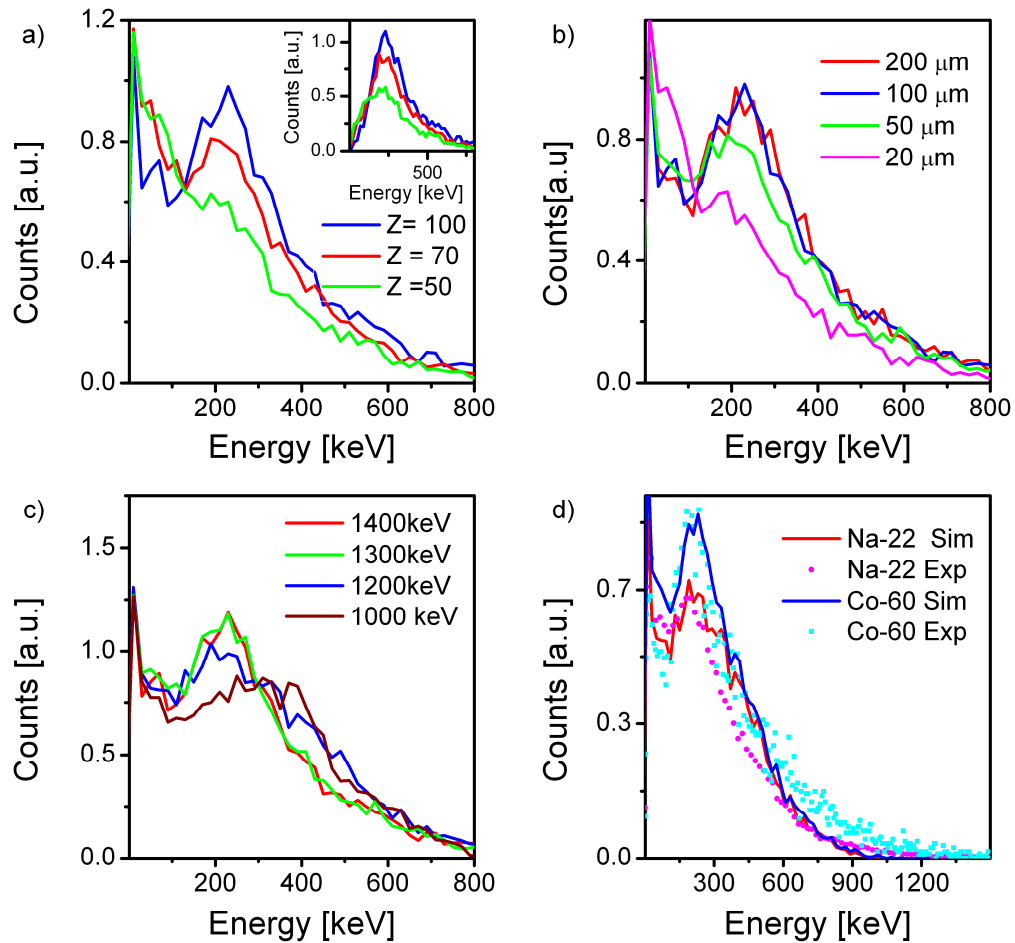


Figure 3-6: a) Simulated signal shape dependence on the atomic number of the material. For increasing Z a bump at 200 keV appears. The inset shows the signal contribution from the back layer. The simulations have been carried out for 1300 keV photons and a 100 μm thick back layer. b) Signal shape dependence on the thickness of the back layer (1300 keV photon energy and $Z = 100$). c) Signal shape dependence on the energy of the incoming radiation (100 μm thickness and $Z = 100$). d) Experimental spectra (dots) for Co-60 and Ni-22 reproduced from Figure 3-5a and best-fit GEANT4 simulations results (solid lines) obtained from modelling the detector with 100 μm back layer thickness and $Z = 100$.

The observed behaviour can be explained using the differential scattering cross-section for the Compton Scattering $d\sigma/d\Omega$ given by the Klein-Nishina formula[9] (3.2). The cross-section increases linearly with Z and this is the reason for the appearance of the intense peak when the back layer is included in the simulations. Moreover, increasing the incoming photon energy lowers the cross-section and increases the mean free path (the average distance between collisions). This implies that, for higher energies, the interaction occurs at a greater depth inside the material than for lower energies. Therefore, for higher energy, only photons that are Compton-scattered at large angles can be collected. As a consequence, the contribution to the spectrum from the back layer changes from being broad for lower energy photons, to increasingly narrow as it finally approaches the Compton back scattering energy for the higher energy photons. This explains the appearance of the peak at about 200 keV in the spectra, both in the experimental data and in the simulations, which corresponds to Compton backscattered photons for the range 1300-1400 keV.

With this knowledge, best fits to the recorded Timepix spectra for the Co-60 and Na-22 sources have been obtained, as shown in Figure 3-6(d). Good agreement is obtained for a $Z = 100$, 100 μm thick back layer model. The spectra have been reconstructed taking into account all of the energy deposited in the Silicon layer plus a contribution of 50% of the energy scattered by the back layer. We considered just a fraction of the total energy deposited in the back layer because the electrodes physically occupy only a part of the total volume of the back layer itself and just the energy collected by the electrons contributes to the formation of the signal. The fraction

contributed by the back layer has been chosen to properly match the experimental and the simulated data. The important conclusion of this analysis is that for incoming photons in the MeV range, it is the *shape* of the peak in the spectrum, due to back scattered photons that is related to the energy of the incoming radiation. Therefore, unless the spectral shape is deconvoluted taking the peak into account, the silicon Timepix cannot be utilised as a spectrometer in the MeV range.

However, exploiting the Compton effect, the energy range can be increased by a significant amount. A 300 μm thick element Si Timepix can detect photon energies up to around ~ 80 keV [14]. It is possible to use Compton side-scattering at an angle of 150° to extend the energy range to ~ 120 keV (Figure 3-2a). The 1 mm thick CdTe model, has a nominal detecting range that, because of the thicker element and higher atomic number, extends up to 662 keV (confirmed by observing emission lines from the Cs-137 calibration source). Therefore, applying the Compton side-scattering configuration to the CdTe Timepix, the maximum detectable energy can easily extend to several MeV, perfectly matching the requirements for the resonant betatron experiment.

3.3 Experimental Setup

To investigate the potential of betatron emission as a brilliant source of hard x-ray and gamma rays, we have focussed a 5 J and 55 ± 5 fs duration laser pulse from the ASTRA-Gemini laser [19] into a preformed plasma waveguide [20] with a plasma

density $n_p \approx 2 \times 10^{18} \text{ cm}^{-3}$, as shown in Figure 3-7. The initial vector potential $a_0 \approx 2$ of the laser pulse is enhanced as a result of the non linear evolution in the plasma waveguide and can easily reach a value 3 times higher (giving $L_d \approx 10 \text{ mm}$ and $R \approx 20 \text{ }\mu\text{m}$), which subsequently leads to self-injection and quasi-monoenergetic electron bunches.

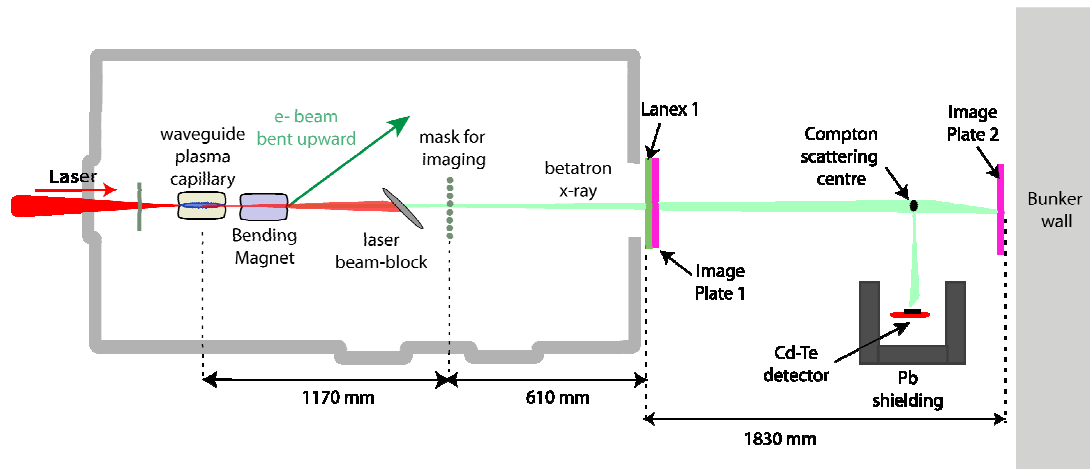


Figure 3-7: Experimental setup: A F/16 spherical mirror focuses the laser pulse (5 J, $55 \pm 5 \text{ fs}$, 800 nm) to a $40 \pm 5 \text{ }\mu\text{m}$ diameter spot at the entrance of 4 cm long, $300 \text{ }\mu\text{m}$ diameter, pre-formed plasma capillary waveguide [20] with an on-axis density of $n_p \approx 2 \times 10^{18} \text{ cm}^{-3}$. The laser beam initially has an intensity of $9 \times 10^{18} \text{ Wcm}^{-2}$ that corresponds to $a_0 = 2$ and bubble radius $R = 10 \text{ }\mu\text{m}$. A $600 \text{ }\mu\text{m}$ thick Al foil blocks laser light from x-ray detectors. At the end of the interaction chamber Lanex 1 and image plate 1 is used to detect the electron beam deflected by the bending magnet. The energy resolution of the electron spectrometer estimated with the code General Particle Tracer [21] is $\sim 2\%$. On the r.h.s.: the x-ray detectors; image plate 2 placed on axis and the CdTe detector screened behind lead bricks to measure the radiation side-scattered by the aluminium post via the Compton effect.

The electron beam was deflected from the laser axis using a bending magnet (0.7 T) placed after the capillary. The deflected electrons were detected with a Lanex screen at the end of the interaction chamber (Figure 3-7) allowing a simultaneous measurement of the electron beam charge and energy.

3.3.1 Highly Damped Regime

In the highly damped stage (I) x-rays are expected to be emitted with spectra peaked at few tens of keV. In this range the CdTe detector [12] cannot be used because of strong K_{α} emission at 30 keV from the semiconductor bulk. As an alternative, we have used a set of copper and tungsten filters to selectively attenuate the x-ray flux and estimate the spectral content using an x-ray image-plate (IP), while simultaneously measuring the electron spectra. The x-ray image-plate used during the experiment is the FUJI-BAS-MS-2325. An image plate is made of a layer of barium fluorohalide phosphor crystals embedded in a plastic supportive medium. When an IP is exposed to x-rays, the secondary electrons produced are trapped into lattice defects intentionally introduced during the manufacturing. The trapped states decay and emit radiation in the blue spectral region. The rate of decay depends on the temperature and the composition of the image plate. The metastable states decay also if illuminated by 640 nm light [22], as happens during the read-out in a scanning system. The image-plate is sensitive mainly to photons in the 4-80 keV [23] range but can detect higher energies photons with reduced

sensitivity [24]. Image plates are largely used for x-ray imaging thanks to the excellent dynamic range, efficiency and large area [23]. To measure the x-ray beam divergence and estimate the critical photon energy, an image plate was placed on axis against the Perspex window of the vacuum chamber. A set of metal foils (4 per time), of different thicknesses or material, were placed 93 cm from the capillary exit on the x-ray beam axis. The electron beam is bent upward by the bending magnet to avoid irradiating the filters and image plates. Simultaneous measurement of the attenuation through different foils gives a good estimation of both the background noise level and the critical photon energy of the emitted radiation. Assuming that the incoming radiation has a synchrotron like spectrum, we calculated the critical energy required to reproduce the measured attenuation through the set of filters. Using this technique it has been possible to estimate the peaks of the spectra to be around 20 ± 2 keV, corresponding to a critical photon energy of 60 keV, while the measured x-ray angular divergence is 14 mrad, for 600-700 MeV electrons as shown in Figure 3-8. Using these values in Equations 2.33, 2.34 and 2.36, we obtain $n_e \approx 2 \times 10^{18} \text{ cm}^{-3}$, $r_\beta \approx 3 \mu\text{m}$ and $a_\beta \approx 20$. The measured γ and the corresponding calculated r_β and a_β match exactly to values expected for the highly damped regime (I) predicted with OSIRIS [25], as shown in Figure 2.3e-h.

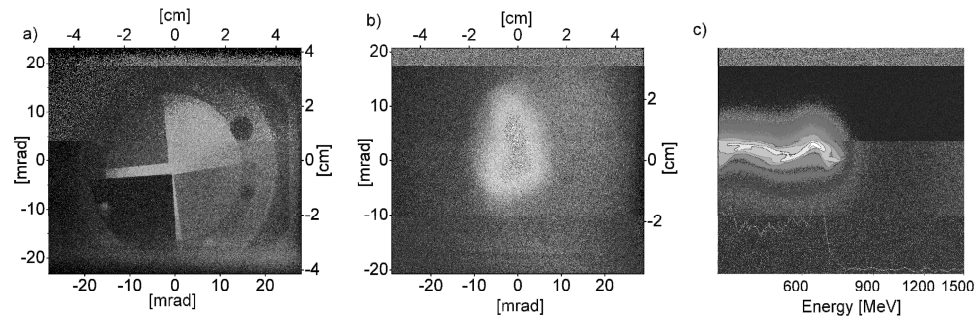


Figure 3-8: X-ray beam and electrons spectrum recorded using an image plate at the end of the vacuum chamber. a) X-ray image as transmitted through metallic filters (0.3 (top left) and 1 mm (bottom left) tungsten foil, 0.5 (top right) and 1 mm (bottom right) copper foil). Calibrated filter attenuation gives a spectral peak at 20 keV (critical energy of 60 ± 15 keV). b) X-ray beam profile with a divergence of 14 mrad measured simultaneously with 700 ± 10 MeV electron beam shown in c).

3.3.2 Weakly and Strongly Resonant Regime

The weakly and strongly resonant regimes have been investigated using Timepix. To minimise background radiation coming mainly from the bremsstrahlung background, the electron beams are bent away from the laser axis with the dipole magnet placed immediately after the accelerator. With this solution the electrons hit the chamber wall and eventually generate the bremsstrahlung radiation off axis. We arrived to choose this configuration after having problem with bremsstrahlung background in a previous attempt of this same experiment. In that case the electron beam was bent off axis after the interaction chamber with the magnet of an electron spectrometer that was connected

to the interaction chamber by a steel pipe. Because of the electrons pointing instability, which is made worse by the betatron oscillations, the electrons often hit the pipe or the chamber wall before entering the electron spectrometer, resulting in a strong source of bremsstrahlung radiation that overlapped and masked the betatron radiation. In the new configuration a Perspex window placed on the chamber end wall transmits the x-ray radiation onto a 12 mm diameter aluminium rod placed on-axis 3.4 m from the source. The Timepix detector is placed in a shielded enclosure to ensure that only Compton side scattered radiation is detected. The scattering angle is fixed at 90° as a compromise between resolution, flux attenuation and laboratory geometry. At this angle of detection, the energy range is moderate for the silicon detector but significant for the CdTe detector [up to several MeV for CdTe as shown in Figure 3-2(a)]. The flux attenuation, calculated using GEANT4, is a factor of 10^6 - 10^7 for both detectors. Two examples of resonant cases (II & III) of x-ray spectra, for a 20% higher plasma density compared with the non resonant case, are shown in Figure 3-9. The spectra have been recorded with the CdTe detector in the Compton side scattering configuration. Here the semiconductor detector measures the betatron radiation Compton side scattered at 90° from a 12 mm diameter aluminium rod. The x-ray spectrum in Figure 3-9(a) peaks at 50 keV (i.e. critical energy of 150 keV). For $n_e = 2 \times 10^{18} \text{ cm}^{-3}$, $\gamma = 1400$ and $E_c = 150 \text{ keV}$, from equation 2.33 and 2.36, we can calculate $a_\beta = 50$ and $r_\beta = 7 \mu\text{m}$, which matches the values expected for the weakly resonant case (II) shown in Figure 2.3e-h, where injection occurs later and the electron bunch exits the potential before dephasing and growth in r_β has taken place. In contrast, the peak at 150 keV (i.e. critical energy of 450

keV) shown in Figure 3-9 b corresponds to a strong resonant interaction with the laser (III) and evolution that has already passed dephasing. Doing the same kind of calculations for the new values $n_e = 2 \times 10^{18} \text{ cm}^{-3}$, $\gamma = 1400$ and $E_c = 450 \text{ keV}$, we obtain $r_\beta = 23 \text{ }\mu\text{m}$, $a_\beta = 160$. For these parameters, assuming $a_0 = 6$ after self-focusing and using Equation 2.15, we can calculate the bubble radius to be $20 \text{ }\mu\text{m}$: the oscillations are now completely filling the bubble. This is what is expected for the strongly resonant case (III) as shown in Figure 2.3.

When no resonance was occurring no radiation was scattered by the aluminium post and no signal was detected by Timepix.

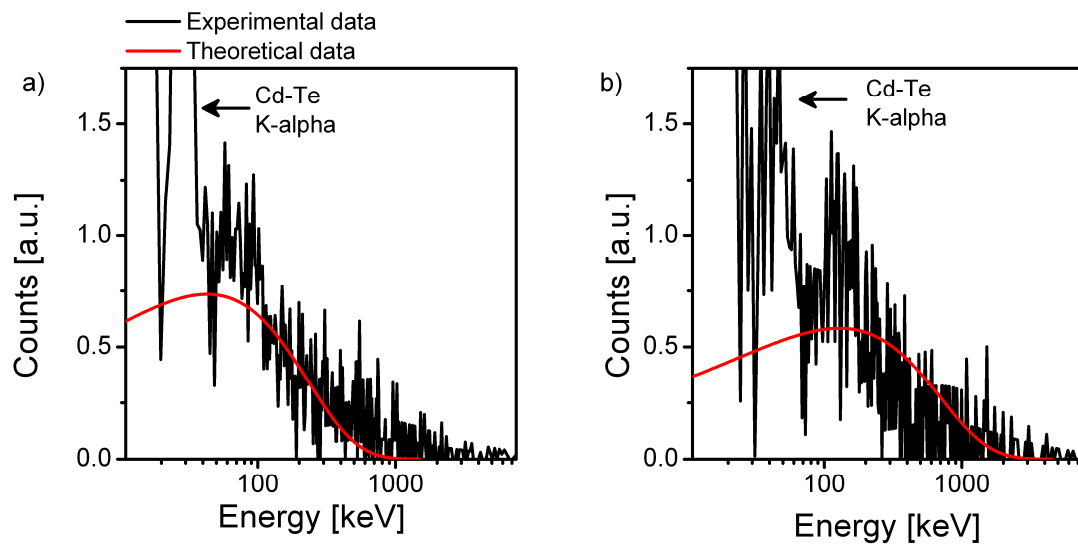


Figure 3-9: Two of the single shot x-ray spectra, from 90° Compton side scattered radiation from a 12 mm Al rod measured with a CdTe semiconductor detector, are overlapped with the predicted synchrotron spectra corresponding to the measured critical photon energies. l.h.s: a spectrum peaking at 50 keV, corresponding to a critical energy

of 150 keV, identifies the weakly resonant case II. r.h.s. a spectrum peaking at 150 keV, corresponding to a critical energy of 450 keV, identifies as the strongly resonant case III. During the experiment we recorded in total ~ 20 single shot spectra corresponding to the harmonically resonant regime. The measured electron energy is 633 ± 70 MeV for both cases. The energy has been estimated from the average over the previous 10 electron spectra being the lanex removed during the single shot x-ray measurement. The uncertainty on the measure is given by the r.m.s.

3.3.3 Phase Contrast Experiment

For a betatron source, the size of the source corresponds to the amplitude of the betatron oscillation. To measure the betatron source and then prove that the gamma rays originate from a very small source size we have used phase contrast technique. In conventional radiography, radiation that passes through an inhomogeneous object is differentially absorbed, resulting in a detected intensity pattern reflecting the distribution of absorbing material of the sample. Phase-contrast imaging, on the other hand, provides a measure of the variation of the phase of the transmitted x-ray radiation, which enhances the contrast of weakly absorbing media. Phase-contrast imaging based on a broad bandwidth betatron source, which has a high spatial coherence, can be used to image large areas with a lower absorbed dose than conventional imaging techniques. Conventional x-ray imaging is based on absorption by the object material, which depends on the imaginary part β of the refractive index (where the refractive index is expressed as $n = 1 - d + i\tilde{\beta}$). Image contrast is thus entirely due to absorption

differences. For weakly differentiated absorbing or fine structures the contrast is very low. However, differences in the real part of the refractive index, d , allow the contrast to be enhanced to highlight detail with respect to the surrounding background. The main limitation due to a widespread application of phase contrast imaging is the necessity of utilising coherent x-ray source and a detector with a high spatial resolution. Fringe patterns are mainly destroyed by the blur induced by the x-ray source size (spatial coherence) and by the polychromatism of the beam (temporal coherence). However Wilkins and al. in the letter to Nature [26] have shown that it is possible to acquire phase contrast imaging with polychromatic hard x-ray beam having high spatial coherence. As far as the spatial coherence is concerned, it is defined as:

$$d_c = \lambda \frac{\Delta}{2\sigma}, \quad (3.3)$$

where Δ is the source-sample distance, σ is the source size (Figure 3-10).

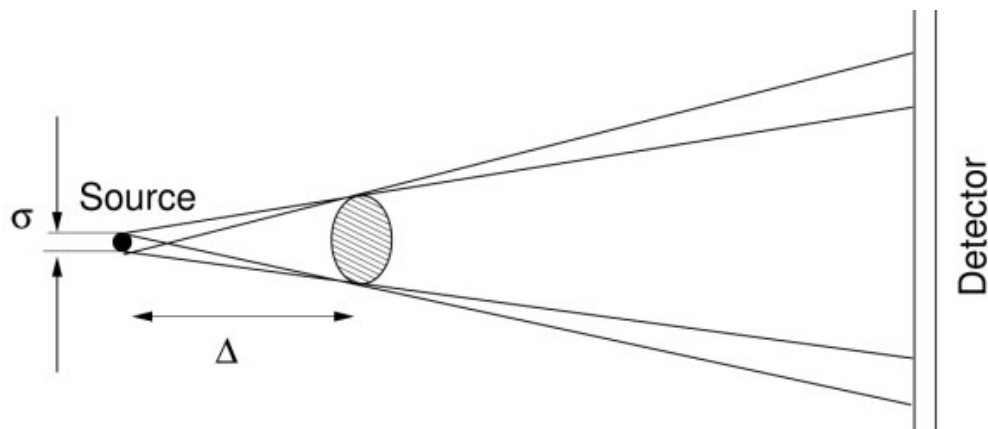


Figure 3-10: Phase contrast imaging simplified scheme.

During the experiment we imaged, using the betatron radiation, a grid of copper wires with different thickness (100, 75, 50, 40 and 25 μm diameter), placed 1.17 m from the betatron source inside the vacuum chamber. An imaging plate (FUJI-BAS-MS-2325) was placed at 3.6 m from the source. The scanning resolution of the image plate was 50 μm . The image detected in a single shot experiment is shown in Figure 3-11a. To deduce information on the source size from the recorded image, we have compared the experimental wires profile with calculations done for a finite size source. In the calculation we have traced the rays from the source to the screen taking into account both attenuation and refraction occurring inside the wires. To estimate the refractive index, we have considered the electrons to be free in the metal and therefore treated the wire as plasma. Therefore, the plasma density corresponding to the metal can be estimated as $n_p = \frac{d_{Cu}}{A} N_A Z$, where d_{Cu} is the metal density, A and Z are the atomic weight and atomic number and N_A is the Avogadro's number. From the plasma density it is then possible to calculate the plasma frequency and the dielectric constant as: $\epsilon = 1 - \omega_p^2 / \omega^2$ with ω the frequency of the incoming radiation. The calculations have been done for an incoherent source with a flat distribution of the photon energy in the range of 10 – 100 keV. The contribution of each ray, in amplitude and phase, is added up to produce the final intensity distribution. The calculated values are compared with the measured profiles that in turn result from an average over 5 different profiles taken along the wire length to account the wire alignment with respect to the image plate. A good match for all the different thickness is obtained for a source size of 15 μm , which

corresponds to an oscillation amplitude $r_\beta = 7.5 \mu\text{m}$ (Figure 3-12). This matches the predicted oscillation amplitude in the weakly resonant case (II) with OSIRIS.

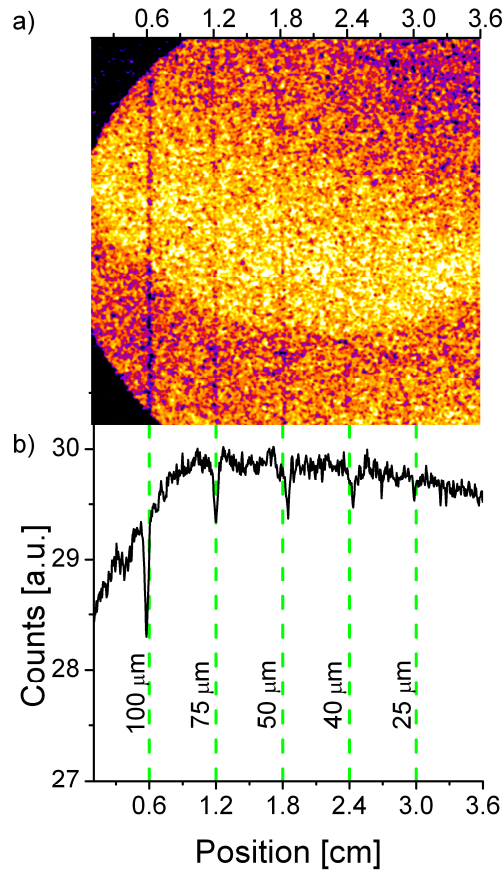


Figure 3-11: a) Phase contrast image recorded on an image-plate placed close to the bunker wall, showing four copper wires of 100, 75, 50 and 40 μm thickness respectively from left to right. Lineout b) is image profiles where the faint shadow of a fifth 25 μm thick wire is barely visible at position 3 cm. From calculations the expected attenuation without refraction would give a signal about the 70% weaker.

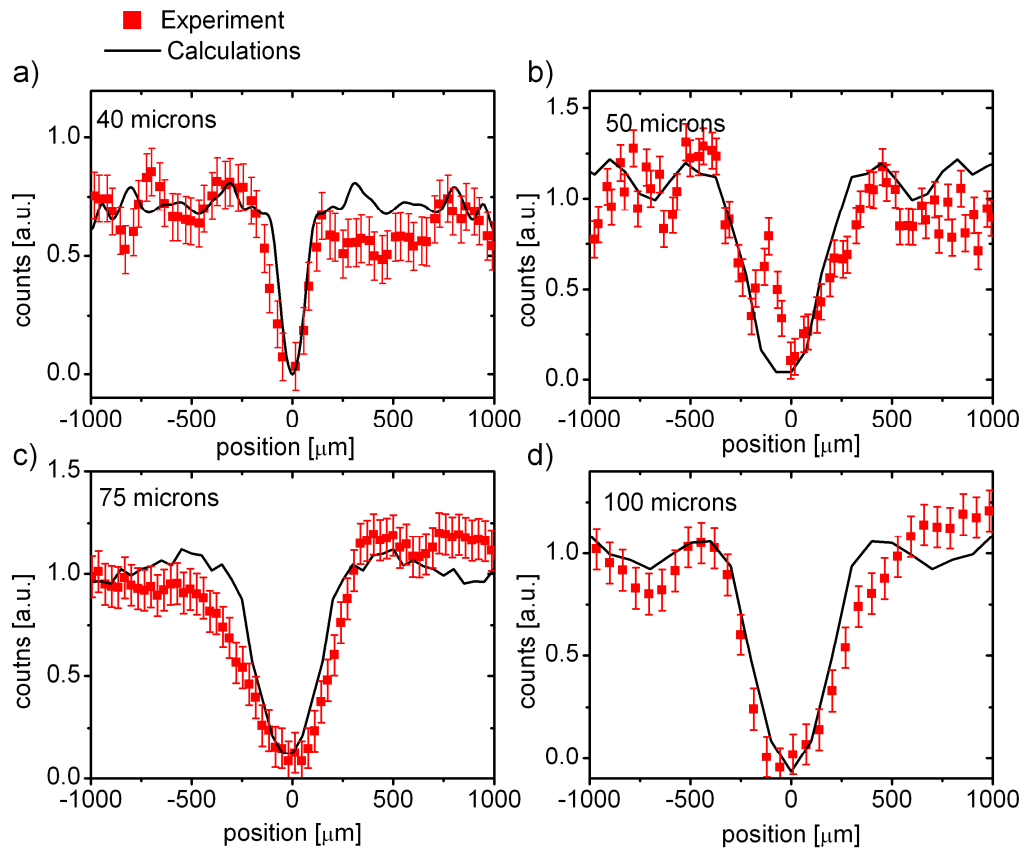


Figure 3-12: Plots of the shadows cast by the wires (solid squares) compared with data fits (solid lines) consistent with a 15 μm diameter x-ray source size for 40 (a), 50 (b), 75 (c) and 100 μm (d). The calculations have been done assuming an x-ray spectrum distributed over 10 to 100 keV, corresponding to the weakly resonant case. The error bars are given by the standard deviation of the background obtained in the region of the IP alongside the image.

3.4 Conclusion

In conclusion, we have presented the experimental evidence, for the first time, of the electron-laser harmonically resonant interaction predicted in Chapter 2. The three different regimes: highly damped, weakly and strongly resonant have been explored and fully characterized. A summary of the results obtained are reported in Table 3-2. As already pointed out in the previous sections, the agreement between experiment and simulations is good in all the three regimes. It is important to notice that, while switching from one regime to another, the measured electron energy is almost constant ~ 700 MeV. Indeed, because of Equation 2.33 and 2.39, we expect the most part of the emission to occur close to dephasing when the energy is maximum. And moreover, as predicted in OSIRIS simulations, shown once again in Figure 2.3, all three regimes can occur close to dephasing. The regime of operation can be selected using the tuning parameters: laser intensity, laser pulse length, density modulation inside the capillary and controlled injection of electrons. The success of the experiment relies first of all on a deep theoretical understanding of the electron-laser interaction process that has allowed a careful design of the experiment and to accurately choose, model and understand the detection system.

The experimental measurements were successful thanks also to the adoption of a Compton side scattering configuration to measure the intense narrow beam of hard x-rays resulting from the betatron motion of very energetic electrons. The spectra measured in the strongly resonant regime extend up to several MeV, an energy region

where currently no synchrotron sources are available or are planned to be in the near future.

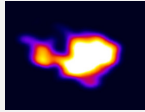
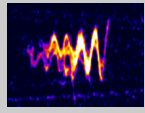
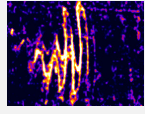
Regime	Parameters	
	Simulations	Experiment
Highly Damped (I)	 $r_\beta = 2-3 \mu\text{m}$ $a_\beta = 25$ $E_c = 60 \text{ keV}^{(**)}$ $E_e \sim 750 \text{ MeV}$	$r_\beta = 3 \mu\text{m}^{(**)}$ $a_\beta = 20^{(**)}$ $E_c = 60 \text{ keV}^{(*)}$ $E_e = 700 \pm 10 \text{ MeV}^{(*)}$
Weakly Resonant (II)	 $r_\beta = 8 \mu\text{m}^{(*)}$ $a_\beta = 50^{(*)}$ $E_c = 150 \text{ keV}^{(**)}$ $E_e \sim 750 \text{ MeV}^{(*)}$	$r_\beta = 7.5 \mu\text{m}^{(*)}$ $a_\beta = 50^{(**)}$ $E_c = 150 \text{ keV}^{(*)}$ $E_e = 633 \pm 70 \text{ MeV}^{(*)}$
Strongly Resonant (III)	 $r_\beta = 20 \mu\text{m}^{(*)}$ $a_\beta = 150^{(*)}$ $E_c = 450 \text{ keV}^{(**)}$ $E_e \sim 750 \text{ MeV}^{(*)}$	$r_\beta = 23 \mu\text{m}^{(**)}$ $a_\beta = 160^{(**)}$ $E_c = 450 \text{ keV}^{(*)}$ $E_e = 633 \pm 70 \text{ MeV}^{(*)}$

Table 3-2: Summary of the betatron experiment results. Parameters with * in the simulations column are direct output of OSIRIS and in the experiment column are directly measured. The parameters with ** are calculated from other parameters of the same regime. The values for the simulations parameters are all extracted from Figure 2.3.

The x-ray pulse length is estimated to be ≈ 10 fs from Figure 2.3d, considering that most photons are emitted when a_β is large at resonance. From GEANT4 simulations, it has been possible to calculate the x-ray detection efficiency in the Compton side scattering configuration and to estimate the number of incoming photons to be about 5×10^8 . After correcting the acquired spectrum by the detection efficiency calculated

using GEANT4, we obtained the number of photons per unit energy that can be then normalized to 0.1% of the bandwidth (BW). By using source size value of 20 μm , estimated from the OSIRIS simulations for the strongly resonant case (III), assuming that all the photons emitted in the solid angle with elliptical section, having as minor axis $1/\gamma$ and major axis a_β/γ with $\gamma=1500$ and $a_\beta=150$ for the weakly resonant case, and that the pulse length is the one estimated from OSIRIS simulations (10 fs), we can estimate the peak brilliance to be in excess of 10^{23} photons/s mrad² mm² 0.1% B.W., which is comparable with the brilliance of a third generation storage ring but in a spectral range not accessible to synchrotrons. In the strongly resonant regime it should be possible to scale up the resonant betatron source spectra to several MeV with higher laser intensities and lower plasma densities. For example $a_0 = 10$, $n_e = 10^{18}$ cm⁻³ and $r_\beta = R = 34$ μm gives $a_\beta \approx 200$, which will produce photons with a critical energy > 5 MeV and an efficiency of the order of 1% or larger. Such a source would open up new applications in high contrast imaging of weakly absorbing matter, time resolved probing of the nucleus and production of medical radio-isotopes through photo-nuclear reactions and dense matter imaging (i.e. probing pellets used in inertial confinement fusion).

References

1. Shah R.C., Albert F., Ta Phuoc K., Shevchenko O., Boschetto D., Pukhov A., Kiselev S., Burgy F., Rousseau J.P., and Rousse A., "Coherence-Based Transverse Measurement of Synchrotron X-ray Radiation from Relativistic Laser-Plasma Interaction and Laser-Accelerated Electrons", Phys Rev E, 74(4), 045401 (2006)

2. Cipiccia S., et al., "Gamma-Rays from Harmonically Resonant Betatron Oscillations in a Plasma Wake", *Nat Phys*, 7(11), 867 (2011)
3. Mangles S.P.D., et al., "Laser-Wakefield Acceleration of Monoenergetic Electron Beams in the First Plasma-Wave Period", *Phys Rev Lett*, 96(21), 215001 (2006)
4. Nemeth K., Shen B.G., Li Y.L., Shang H.T., Crowell R., Harkay K.C., and RCary J., "Laser-Driven Coherent Betatron Oscillation in a Laser-Wakefield Cavity", *Phys Rev Lett*, 100(9), 095002 (2008)
5. Glinec Y., Faure J., Guemnie-Tafo A., Malka V., Monard H., Larbre J.P., Waele V.D., Marignier J.L., and Mostafavi M., "Absolute Calibration for a Broad Range Single Shot Electron Spectrometer", *Rev Sci Instrum*, 77(10), 103301 (2006)
6. Zeil K., Kraft S.D., Jochmann A., Kroll F., Jahr W., Schramm U., Karsch L., Pawelke J., Hidding B., and Pretzler G., "Absolute Response of Fuji Imaging Plate Detectors to Picosecond-Electron Bunches", *Rev Sci Instrum*, 81, 013307 (2010)
7. Jaroszynski D.A., et al., "Radiation Sources Based on Laser-Plasma Interactions", *Philos T Roy Soc A*, 364(1840), 689 (2006)
8. Kneip S., et al., "Non-invasive Characterization of Transverse Beam Emittance of Electrons from a Laser-Plasma Wakefield Accelerator in the Bubble Regime Using Betatron X-ray Radiation", *arXiv:1105.5559v1*, (2011)
9. Knoll G.F., *Radiation Detection and Measurement: John Wiley & Sons, Inc.* (2000)
10. Bloser P. and Ryan J., "New material advance gamma-ray telescope", *SPIE Newsroom*, 10.1117/2.1200802.1058 (2008)
11. Di Bari D., et al., "Performance of 0.5 x 106 Sensitive Elements Pixel Telescope in the WA97 Heavy Ion Experiment at CERN", *Nuclear Instruments and Methods in Physics Research Section A: Accelerators, Spectrometers, Detectors and Associated Equipment*, 395(3), 391 (1997)

12. Llopart X., Ballabriga R., Campbell M., Tlustos L., and Wong W., "Timepix, a 65k Programmable Pixel Readout Chip for Arrival Time, Energy and/or Photon Counting Measurements", Nucl Instrum Meth A, 581(1-2), 485 (2007)
13. Llopart X., Campbell M., Dinapoli R., Segundo D.S., and Pemigotti E., "Medipix2: a 64-k Pixel Readout Chip with 55 μm Square Elements Working in Single Photon Counting Mode", Ieee T Nucl Sci, 49(5), 2279 (2002)
14. Jakůbek J., "Precise Energy Calibration of Pixel Detector Working in Time-Over-Threshold Mode ", Nucl. Instr. Methods A (In press) 633, S262 (2011)
15. Platkevič M., Granja C., Jakůbek J., and Vykydal Z., "Medipix in Extremely Hostile Environment", Proceedings Workshop CTU Prague, 12, 212 (2008)
16. Cipiccia S., et al., "A single-shot detector for ultra-fast, high flux, broad energy range X-ray spectroscopy based on Compton scattering", Journal of Instrumentation, submitted (2011)
17. Cermak P., Stekl I., Bocarov V., Jakubek J., Pospisil S., Fiederle M., and Zuber K., "The Characterization of CdTe TimePix Device and the Study of its Capabilities for the Double Beta Decay Measurements", Nuclear Science Symposium Conference Record, 444 (2008)
18. Agostinelli S., et al., "GEANT4-a Simulation Toolkit", Nucl Instrum Meth A, 506(3), 250 (2003)
19. Hooker C.J., et al., "Commissioning the Astra Gemini Petawatt Ti:sapphire Laser System", CLEO/QELS 2008, 1 (2008)
20. Hooker S.M., et al., "GeV Plasma Accelerators Driven in Waveguides ", Plasma Phys. Control. Fusion, 49, B403 (2007)
21. Van der Geer S.B. and De Loos M.J. "General Particle Tracer code: design, implementation and application", Doctoral degree Universiteit Eindhoven Eindhoven (2001)
22. Paterson I.J., Clarke R.J., Woolsey N.C., and Gregori G., "Image Plate Response for Conditions Relevant to Laser-Plasma Interaction Experiments", Meas Sci Technol, 19, 095301 (2008)
23. Thompson A., et al., X-ray data Booklet. third ed Berkeley. (2009)

24. Thoms M., "The Quantum Efficiency of Radiographic Imaging with Image Plates", *Nuclear Instruments & Methods in Physics Research A*, 378, 13 (1996)
25. Fonseca R.A., "Lectures Notes", *Comput. Sci.*, 2331, 9 (2002)
26. Wilkins S.W., Gureyev T.E., Gao D., Pogany A., and Stevenson A.W., "Phase-Contrast Imaging Using Polychromatic Hard X-rays", *Nature*, 384(6607), 335 (1996)

Chapter 4

4.1 Introduction

The betatron radiation emitted by electrons undergoing acceleration in a laser-plasma wakefield accelerator has been shown both theoretically and experimentally to be a very compact bright tuneable x- and gamma-ray source up to MeV photon energy range. The source covers an energy range where there are currently no synchrotron sources and in general there are no high peak brightness tuneable light sources. Despite the effort to cover this gap also using Compton back scattering [1], the only other high brightness gamma-ray sources are in nature, i.e. gamma-ray burst in distant astrophysics sources and nuclear decays. Moreover, the scaling laws for betatron emission suggest methods for further enhancing the performance of these sources to extend their energy range and efficiency. This will make the source attractive for applications such as radioisotopes generation or dense matter probing where a high flux of photons with an energy above 10 MeV is required. To satisfy this requirement, high repetition, higher power lasers are needed. The rapid development of laser technology is close to providing 10 Hz PW devices and it is anticipated that kHz PW lasers based on diode

laser technology, will be commercially available in the future. However, with the current state of the art another compact high efficiency gamma-ray source that reaches beyond 10 MeV and based on the LWFA, can be produced by taking advantage of a sibling to synchrotron emission: bremsstrahlung.

The word bremsstrahlung comes from two German terms: *bremsen* which means "to brake" and *strahlung* "radiation", as the Collins dictionary reports, is radiation emitted by charge subject to some kind of acceleration. Strictly speaking, synchrotron radiation is a type of bremsstrahlung radiation. However, conventionally synchrotron radiation refers to the case in which the acceleration is perpendicular to the direction of motion and usually due to a magnetic field. Bremsstrahlung radiation refers to the case in which the acceleration is negative (deceleration) and parallel to the direction of motion, arising from collisions with nuclei [2].

When an electron beam passes through dense material, high energy bremsstrahlung photons are emitted in a collimated beam with high flux. In the past decade it has been shown experimentally that a LWFA can drive a bremsstrahlung source [3]. In this Chapter we investigate using GEANT4 [4] Montecarlo simulations, the main tuneable properties of a gamma-ray source based on bremsstrahlung. We show how a source based on this emission process starting from a quasi-monoenergetic LWFA electron beam can produce more than 10^9 photons with a mean energy of 10 MeV per pulse. We present experimental results that show the feasibility of this method of producing high energy photons and compare the results with simulations. We have

evaluated the practical scaling required to effectively use this source as a tool to produce radioisotopes via photo-nuclear reactions.

A further step in modelling the possibilities of a bremsstrahlung based source has led us to discover a potential focusing method of the gamma-ray beam. A procedure to generate a converging gamma-ray beam is studied numerically and a scheme for an experimental proof is proposed. Following a series of easy steps, experimental evidence of a converging gamma-ray source should be obtainable. This would make this bremsstrahlung source a unique source. The impact of a converging gamma-ray beam would be profound: this kind of source has the potential to trigger a technological revolution in many fields e.g. in industrial and medical applications as will be reviewed in the last section of this Chapter.

4.2 Bremsstrahlung Radiation Overview

Bremsstrahlung radiation, as synchrotron radiation, is emitted by accelerated charge and can be described using the Liénard–Wiechert potentials [2], which give the angular distribution of the radiated power as:

$$\frac{dP(t')}{d\Omega} = \frac{e^2}{4\pi c} \gamma^6 \frac{|n \times \{(n - \beta) \times \dot{\beta}\}|^2}{(1 - n \cdot \beta)^5}. \quad (4.1)$$

with $\beta = v/c$ the electron velocity normalised to the speed of light. For the bremsstrahlung process $\beta \parallel \dot{\beta}$ and therefore the total radiated power, obtained by integrating (4.1) over all angles, is:

$$P = \frac{2}{3} \frac{e^2}{m^2 c^3} \left(\frac{dp}{dt} \right)^2. \quad (4.2)$$

It is worthwhile noticing that the emission is more important for light than for heavy particles, because of the m^{-2} dependence. Doing the same calculation for the case $\beta \perp \dot{\beta}$, that is the synchrotron emission, we obtain:

$$P = \frac{2}{3} \frac{e^2}{m^2 c^3} \gamma^2 \left(\frac{dp}{dt} \right)^2. \quad (4.3)$$

The rate of change in momentum in (4.2) is actually the rate of change of particle energy along the path:

$$P = \frac{2}{3} \frac{e^2}{m^2 c^3} \left(\frac{dp}{dt} \right)^2 = \frac{2}{3} \frac{e^2}{m^2 c^3} \left(\frac{dE}{dx} \right)^2, \quad (4.4)$$

where the term $\frac{dE}{dx}$ is the energy lost by the particle per unit of path length. For an electron the quantity $\frac{dE}{dx}$ lost via bremsstrahlung is:

$$-\left(\frac{dE}{dx} \right) = \frac{NEZ(Z+1)e^4}{137m_e^2 c^4} \left(4 \ln \frac{2E}{m_e c^2} - \frac{4}{3} \right), \quad (4.5)$$

where N is the atomic density, E the electron energy and Z the atomic number. This formula indicates that the energy loss is strongly dependent on the particle energy and the atomic mass of the material. Only fast electrons can have a significant bremsstrahlung yield and at relativistic energies the photons are emitted in a narrow cone with an opening angle of $1/\gamma$ [2]. The radiation energy spectrum is a continuum that extends up to the energy of the electron itself. The electron energy and the material properties also determine the cross-section of the process. Bremsstrahlung cross-section calculations, both for non-relativistic and relativistic cases, and for thin and thick targets, are available in the literature and have been widely reviewed by Koch and Motz [5]. The main properties investigated in Ref. [5] that need to be highlighted here are the dependences of the bremsstrahlung spectrum on the electron energy and the photon angle. In the above mentioned article it is shown that for higher electron energy, more photons are emitted at higher energy (Figure 4-1). As far as the spectral angular distribution is concerned, as the emission angle increases, the relative number of high energy photons increases until the trend is reversed for very large angles (Figure 4-2). Therefore a first “tuning knob” is given by the electron energy and the observation angle: by varying these parameters it is possible to obtain different output spectra.

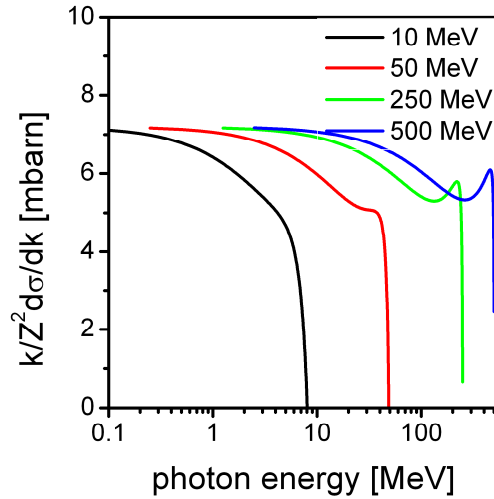


Figure 4-1: The graph shows the dependence of the bremsstrahlung cross section integrated over emission angle on photon and electron energy. k is the energy of the emitted bremsstrahlung photon, Z is the atomic number of the target material. The graph refers to platinum with $Z = 78$ and the calculations have been performed using formula 3BS(e) in Ref. [5].

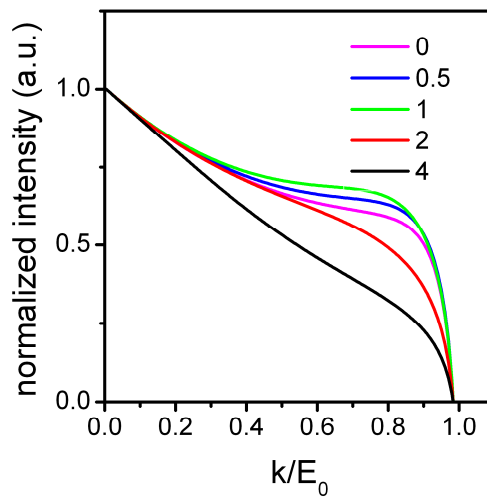


Figure 4-2: The graph shows the relative intensity of the emitted photons depending on the reduced photon angle ($E_0 \cdot \vartheta$) with E_0 the initial electron energy and ϑ the

observation angle. The calculations have been performed for $Z = 78$ using formula 2BS in Ref. [5].

The detailed report of Koch and Motz is a product of many studies accumulated over several years and it is a fundamental starting point for any other bremsstrahlung study. However, the study does not include the dependence of many properties of the bremsstrahlung beam that are key points for harnessing the beam in different applications, i.e. the source size, divergence and conversion efficiency, etc. To use an LWFA electron beam to drive a useful bremsstrahlung source current knowledge must be implemented to understand the combined influence of electron beam and target properties on the final gamma-ray beam properties and to be able to forecast and master the gamma-ray beam yield.

4.3 Laser-Plasma Wakefield Accelerator Driven Bremsstrahlung Source

Laser accelerated electrons have been used to produce a bremsstrahlung radiation in 2002 by R.D. Edward et al. [3], where they produced gamma-ray beams from electrons generated in both a solid target and underdense plasma (gas-jet). In both cases, the electron beam was not monoenergetic and had a thermal Maxwellian distribution. A source based on LWFA electrons in a gas-jet target produced a highly collimated high gamma-ray flux beam. In 2005, Glinec et al. demonstrated the application of such a

source for the radiography of complex and dense objects with sub-millimetre resolution [6]. However, lack of control of the electron beam properties at that time prevented the necessary tuning of the source properties for effective practical applications.

A compact tuneable gamma-ray source would have immediate impact on industrial application for non-destructive inspection, detector calibration and testing. Particularly interesting is the potential medical application as a radioisotope generator for Positron Emission Tomography (PET), which is an imaging modality used to discriminate malignant from non-malignant cells in cancer diagnosis and monitoring [7]. The vast majority of radioisotopes are currently produced in nuclear reactors [8] or, as an alternative, using a proton beam delivered by a conventional accelerator such as a cyclotron or linac. Typical positron emitting isotopes have short half-lives: fluorine-18 (^{18}F) 110 minutes, carbon-11 (^{11}C) 20 minutes, nitrogen-13 (^{13}N) 10 minutes and oxygen-15 (^{15}O) 2 minutes. The most common ones are ^{18}F and ^{11}C mainly because of the longer decay times. Given the short half-life of the radioisotopes, it is necessary at least to implement a fast transportation system to convey isotopes samples from the production centre to the therapy area and, for some isotopes, the generation must be carried out on site just before injection into the patient. Because of the large shielding needed to screen the accelerator and its high associated cost, this equipment is affordable only to very few elite centres. An alternative way to generate radioisotopes is via photo-nuclear reaction by gamma-ray irradiation [9]. At the moment the current technology sets a limit to the availability of gamma-ray sources because of the size and costs related to the particle accelerator driving the source. A gamma-ray source based on LWFA

could be a solution for making the radioisotope production much more affordable and accessible. Indeed, because they are extremely compact, inexpensive and require much less shielding than a conventional accelerator, this source could be made widely available and, in principle, it could be placed directly beside the therapy area.

The feasibility of radioisotopes activation produced by gamma-rays using bremsstrahlung from LWF accelerated electrons having either a Maxwellian [10] or quasi monoenergetic [11, 12] spectral distribution has been demonstrated by several groups. A proof-of-principle study allows the requirements for the electron bunch to be relaxed [12]. However, the ability to tune the gamma beam parameters (source size, divergence and electron-photon conversion efficiency) is a vital factor for real and effective application in medical and scientific fields. The tuneable possibilities of a LWFA-bremsstrahlung based source toward the customization for specific application have hitherto never been explored.

In the next section we study numerically the scaling of the properties of ultra-compact gamma-ray sources based on LWFA and bremsstrahlung. The investigation has been conducted using GEANT4 [4].

4.4 Laser-Plasma Wakefield Accelerator

Bremsstrahlung Source: Scaling

To investigate in detail the electron beam requirements for generating and tuning a compact gamma-ray source based on the bremsstrahlung mechanism we have simulated the process using GEANT4 [4]. The electron source has been simulated as a diverging point source. All the simulations are based on 10^4 particles incident on a metal target. The parameters and their values are shown in Table 4-1.

Parameter	Values	Unit
electron energy	100, 250, 500, 1000	MeV
electron divergence	1, 5, 10	mrad
material (Z)	Al (13), Cu (29), W (74)	.-.
Target thickness	0.05, 0.5, 1, 2	cm
Source-target distance	5, 20, 50, 100	cm

Table 4-1: Electron and target parameters scanned in the simulations.

The bremsstrahlung output has been characterized as a function of the conversion efficiency, defined as the number of photons emitted per electron, the r.m.s. source size, the half-angle divergence and pulse duration. The simulated output efficiency (Figure 4-3) shows a linear dependence on both the electron energy and target thickness. The source size (Figure 4-4) scales linearly with source-target distance and show a superlinear trend as a function of the electron divergence. The linear dependence can easily be understood because increasing the source-target distance, the r.m.s. electron

beam size at the target increases linearly. On the other hand the increase of the electron divergence has a dual effect: the electron beam size at the target increases linearly, as does the path length of the electron inside the target. The interplay of these two factors gives rise to the observed superlinear dependence. The photon divergence (Figure 4-5) scales linearly with Z and target thickness but decreases exponentially with electron energy. Finally, the pulse duration (Figure 4-6) depends only on the target thickness. The length of the gamma-ray pulse emitted has been estimated by determining the position inside the target where the bremsstrahlung process occurs, which corresponds to the occurrence time of the event. From the simulations we estimate the gamma-ray pulse duration to be of the order of picoseconds, independent of the electron bunch length (for bunch length of the order of femtoseconds), but a function of the material, which influences the electron path.

Table 4-2 shows a summary of the results obtained with GEANT4.

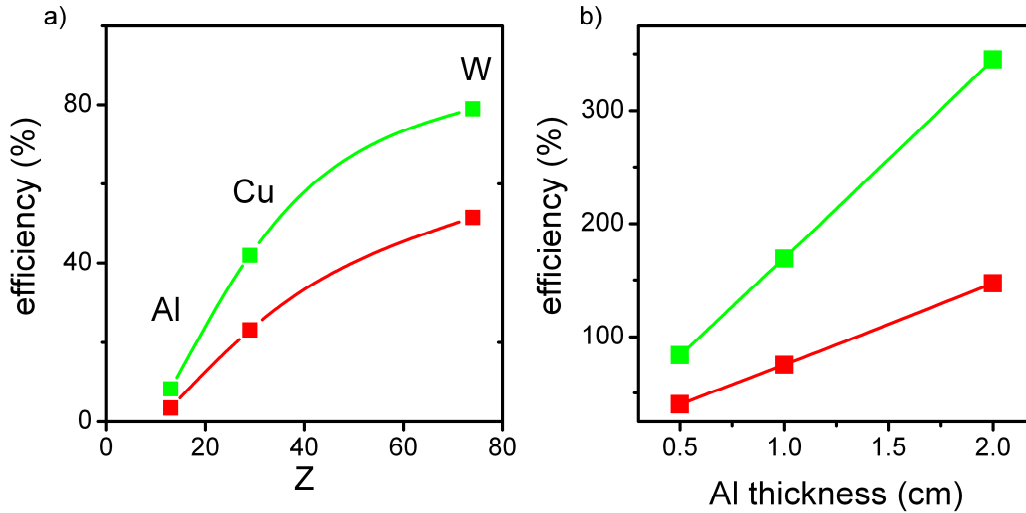


Figure 4-3: Scaling of the photon efficiency with (a) target material Z for thickness 0.5 mm and (b) target thickness (Al target). The green points represent the efficiency for all photons and the red points that for photons > 1 MeV. The efficiency is independent of the electron energy (> 100 MeV), divergence and electron source-target distance.

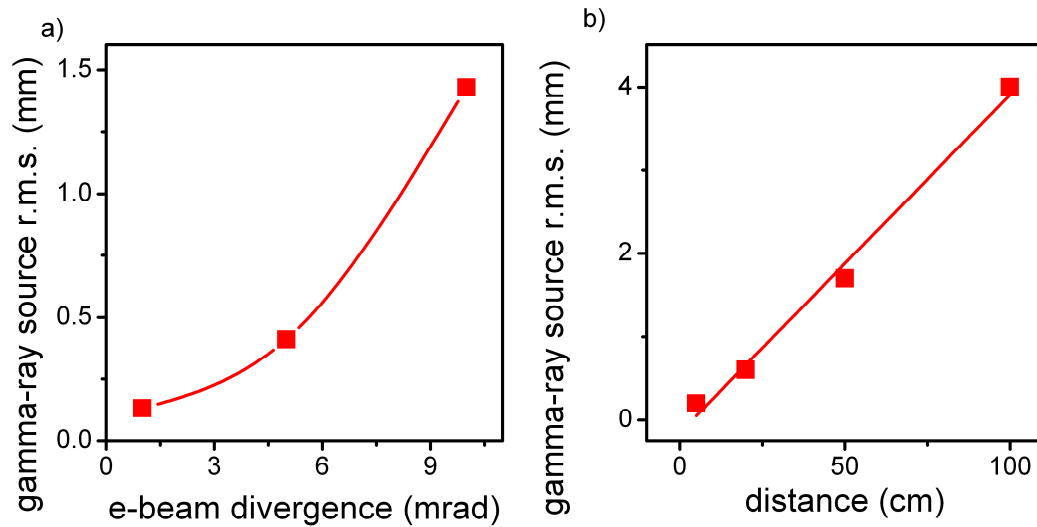


Figure 4-4. Scaling of the photon source size with (a) electron beam divergence for source-target distance = 5 cm and, (b) electron source-target distance for a e-beam divergence = 1 mrad. The photon source size was independent of the electron energy, target material Z and thickness.

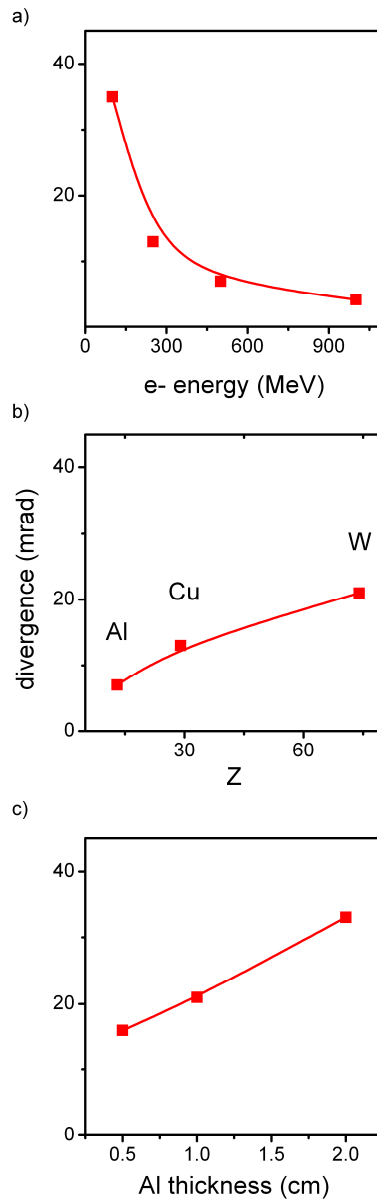


Figure 4-5. Scaling of the photon divergence with (a) electron energy for a 0.5 mm thick Cu target placed 5 cm from the electron source, (b) target material Z for a 250 MeV electron beam, 0.5 mm thick target placed 5 cm from the source and, (c) target thickness, for a target placed at 1 m from the source for 250 a MeV electron beam with a 1 mrad divergence. The divergence of the γ -ray beam is independent of the electron divergence and electron source-target distance.

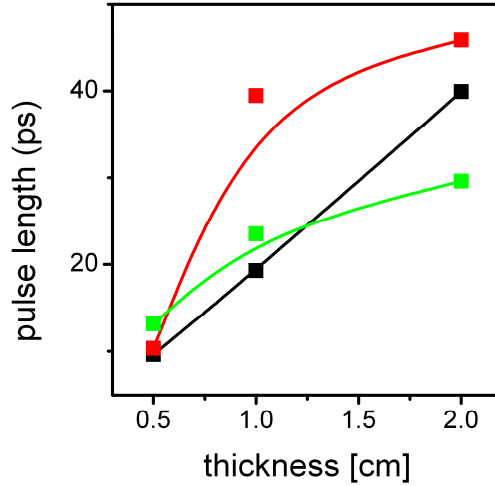


Figure 4-6. Scaling of the photon pulse length with target thickness for aluminium (black points), copper (red points) and Tungsten (green points). The pulse length dependence on the target thickness varies strongly with Z, which determines the integrated length and evolution of the electron path.

	Conversion efficiency [%]	Source size	Gamma divergence	Pulse Duration
e^- energy	=	=	↓	=
e^- divergence	=	↑↑	=	=
Z material	↑↑	=	↑↑	**
Target thickness	↑↑	=	↑↑	↑↑
Source-target distance	=	↑↑	=	=

Table 4-2: Summary of the effects of increasing the parameters listed in the first column on the bremsstrahlung based gamma-ray source properties given in the heading. Symbols ↑, ↓ and = indicate increasing, decreasing and no effect, respectively. ** the Pulse duration dependence on the material changes as the thickness of the target varies. Not a univocal trend can be identified.

The numerical study highlights the key parameters for tuning the properties of a bremsstrahlung based gamma-ray source. All the electron beam parameters identified as “tuning knobs” are adjustable thanks to the progress in LWFA technology. The simulations suggest that a LWFA-bremsstrahlung gamma-ray source has large potential as a new tuneable gamma-ray source. The high flexibility should allow matching different application requirements, such as gamma-ray flux or source size, which could be a crucial factor for applications where e.g. a short exposure time is required or for spatial resolution in high Z material imaging.

4.5 Experimental Setup

A preliminary experimental test to characterize divergence and flux of a gamma-ray bremsstrahlung radiation source based on a monoenergetic laser wakefield accelerated electron beam has been carried out on the Astra Gemini laser system at the Rutherford Appleton Laboratory [13]. During the experiment the vertically polarized 800 nm laser beam was focused onto a 200 μm diameter, 3.3 cm long hydrogen filled sapphire capillary in which plasma was produced by a high voltage discharge (on-axis plasma density of $1\text{-}2 \times 10^{18} \text{ cm}^{-3}$) [14]. The laser energy on target was 2.5-3.5 J and the pulse length was 60-80 fs giving an intensity of $\approx 3\text{-}6 \times 10^{18} \text{ Wcm}^{-2}$ and initial normalized vector potential $a_0 = 1.2\text{-}1.7$.

Electron beams with 10-30 pC charge at the peak were produced on almost every shot. The electron energy spectrum was measured using a magnetic dipole electron spectrometer placed just after the main vacuum chamber and the central electron energy was typically between 200 and 400 MeV, with a measured mean relative energy spread of 8%. The experimental setup and an example of an electron energy spectrum are shown in Figure 4-7: a-b.

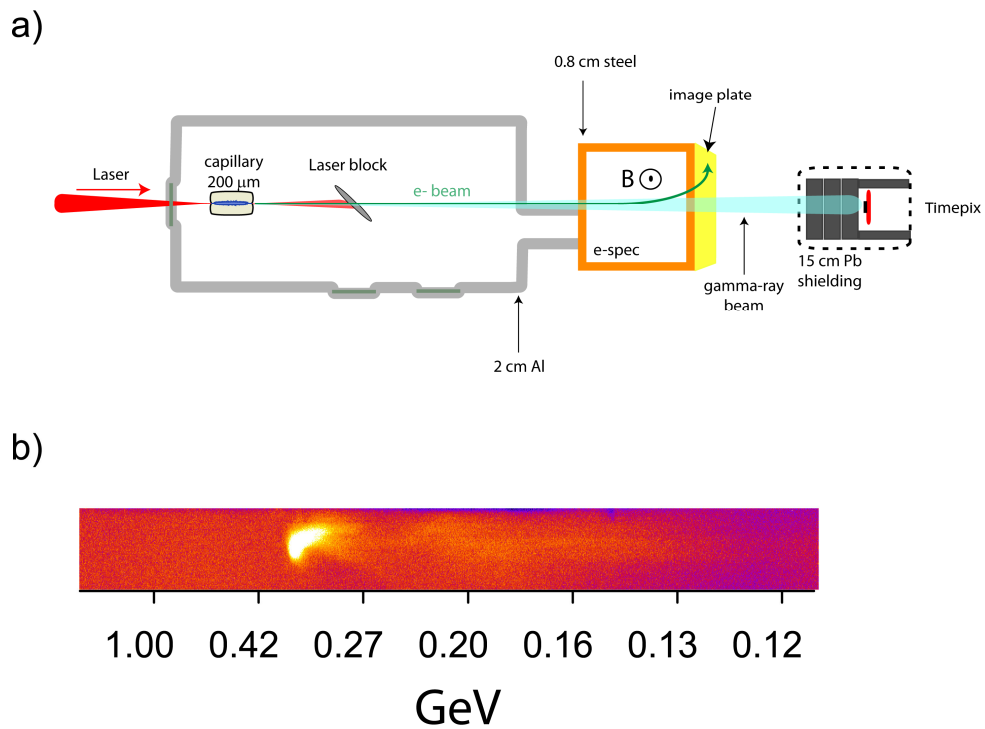


Figure 4-7: (a) Experimental setup and (b) typical electron energy spectrum with a central energy of 330 MeV, measured r.m.s. relative energy spread of 20% and charge of 14 pC.

To generate gamma-rays by the bremsstrahlung process, the electron beam passes through a 2 cm thick Al chamber wall and 8 mm of steel and is then dispersed by the electron spectrometer magnetic field to record the beam energy. The characterization of the source has been achieved by measuring both the transverse spatial beam profile and the photon flux. To measure the profile, an imaging plate (FUJI-BAS-MS-2325) was placed on the electron spectrometer window. In a single shot (Figure 4-8), the electron beam (left side) and the generated gamma-ray beam (centre) are simultaneously recorded by the imaging plate. The measured experimental profile and the corresponding GEANT4 simulation for a 220 MeV electron beam agree very well. During the same experiment we have also demonstrated that the bremsstrahlung beam can be used for imaging and probing dense matter. A 5 cm thick lead brick is placed in front of the lower part of the image plate during this shot. Its shadow is the darker area on the bottom of Figure 4-8a, more evident in the magnified image on the bottom of Figure 4-9. Figure 4-9 shows both the gamma beam profiles recorded within and outside the shadowed area: the bremsstrahlung beam is transmitted through the 5 cm lead brick and is recorded on the image plate. This demonstrates that it can be used to probe dense matter. In Figure 4-9 we notice that the beam imaged within the shadow is shifted toward the left compared with the beam outside the shadow. The photon flux transmitted through the 2 cm Al is attenuated by 8 mm of steel before it reaches the image plate, while there is no attenuation of the following bremsstrahlung emission due to the 8 mm of steel, which, therefore, represents the major contribution to the high energy photon flux hitting the image plate. Because of the fringe field of the electron spectrometer the electrons are slightly bent by the magnetic field before interacting with the steel layer.

The bremsstrahlung emission due to the steel is not parallel to the previous emission from the Al but points slightly to the left compared with the emission from the Al. This explains why the bremsstrahlung beam profile inside and outside the lead shadow are slightly shifted relative to each other.

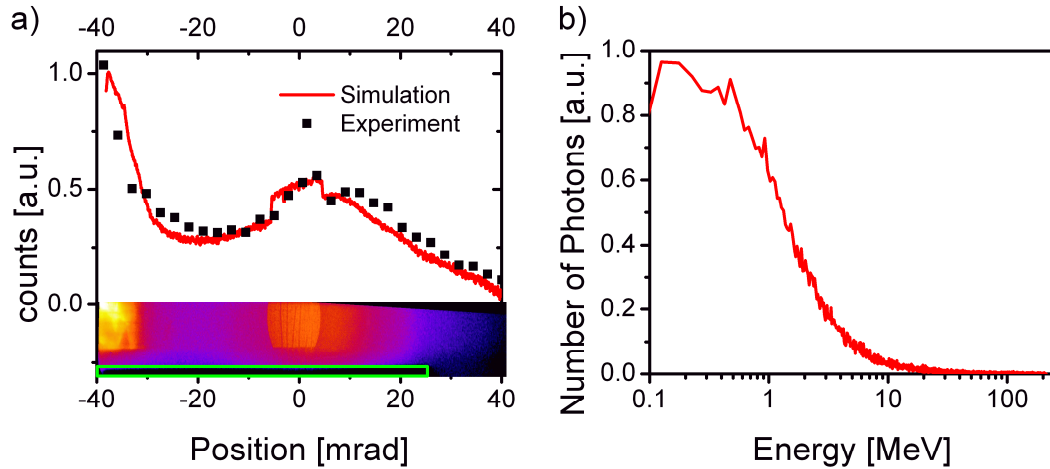


Figure 4-8: (a) Imaging plate image (lower) and corresponding transverse profile (upper). The electron beam is the bright region on the left hand side and the gamma-ray beam produced by the electrons going through the Al and steel target is the bright region on-axis. The experimental profile (red curve) overlaps with the expected profile obtained from GEANT4 simulations (black points) for a 220 MeV electron beam. The centre of the image shows the shadow of the aperture of the main vacuum chamber of the electron spectrometer, (b) calculated energy spectrum of the bremsstrahlung radiation. The green box on the bottom of (a) marks the edges of a 5 cm thick lead brick placed in front of the image plate.

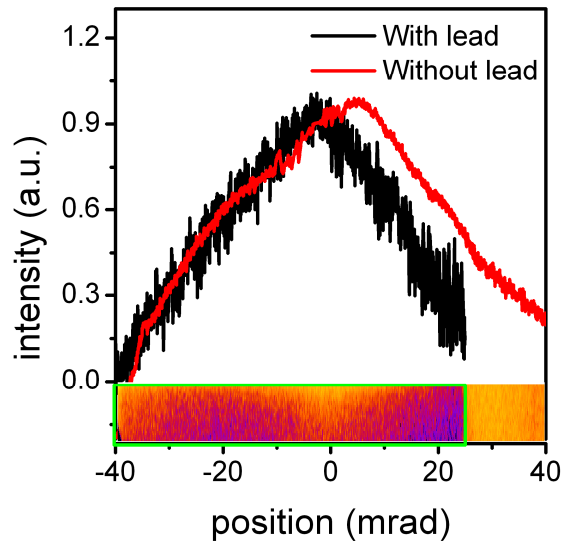


Figure 4-9: Bremsstrahlung beam profile imaged within the lead shadow. The radiation is transmitted through 5 cm of lead and recorded on the image plate. The bottom of the figure is a magnification of Figure 4-8a. The green box marks the corresponding area in Figure 4-8a.

To measure the photon flux we have used a pixelated semiconductor x-ray detector, Timepix [15]. This detector is the same used for the betatron experiment described in Chapter 3. In this case we used the device with a 300 μm thick silicon substrate which gives a detection range from 5 keV up to about 100 keV. When irradiated with higher energy photons, the detector does not adequately function as a spectrometer but still works as a counter [16]. In both cases, operating as a spectrometer and/or a counter, the average photon flux has to be lower than one photon per pixel. In the experiment (Figure 4-7: a), the detector has been used in counter mode, placed on-axis 4 m from the

capillary exit and behind 15 cm of lead to sufficiently attenuate the photon flux. An example of the detector screenshot during the acquisition is shown in Figure 4-10.

The detection efficiency of Timepix in this experimental configuration has been modelled with GEANT4, which shows that it is possible to estimate the average number of incoming photons is $(7 \pm 3) \times 10^8$ per pulse from the average number of detected counts, 630 ± 250 over 12 shots. The maximum number of photons is 1×10^9 . The bremsstrahlung process in this configuration has an efficiency of about 400% that would correspond to a charge of 20-25 pC, which is in good agreement with the average measured charge for the shots under study (15 ± 8 pC). The average photon energy, extrapolated from the expected simulated spectrum [see Figure 4-8 (b)], is 10 MeV while the simulated photon pulse duration is 10 ps. Therefore, each shot corresponds to ~1 mJ, i.e., a power of ~100 MW.

The good agreement between simulations and experimental data supports the possibility of tuning the bremsstrahlung source and verify that its properties are appropriate for applications.

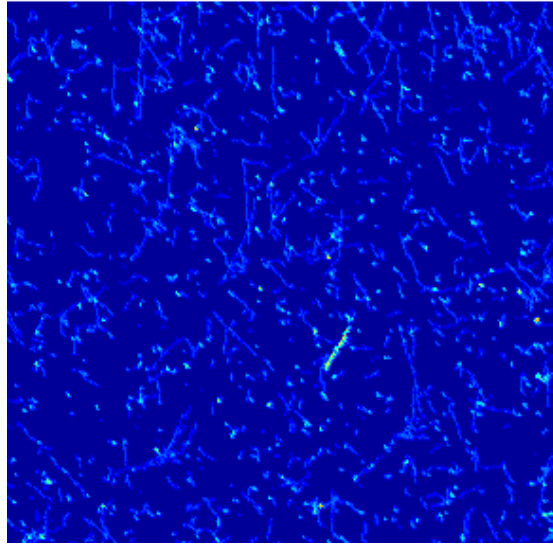


Figure 4-10: Example of the active area screen shot of the Timepix x-ray detector upon irradiation with bremsstrahlung photons. The number of detected counts for this shot is 768.

4.6 Scaling for Potential Applications: Radioisotope Production

We have explored the possibility of harnessing monoenergetic LWFA electron beams to drive a new tuneable gamma-ray source based on the bremsstrahlung process. A numerical study shows that control of the electron beam properties and a proper choice of the target parameters leads to a unique ultra-compact, high energy gamma-ray source that is tuneable in size, divergence and flux. The control of the electron beam properties relies on both the properties of the electron beam and its transport. The test experiment reported here provides results that are in good agreement with the theoretical

expectation, which encourages further development in this direction. The electron properties required are determined by the applications, which also indicate the path to the first concrete applications of LWFA technology. As an example of a potential application, electron beam charge and energy, and the electron-photon efficiency are the key factors for producing radionuclides for PET. These radionuclides are positron emitters, most commonly fluorine-18 (^{18}F) [17], which is usually produced by irradiating oxygen-18 (^{18}O), a stable isotope of oxygen, contained in water or enriched water, with a proton beam with an energy in the range of 5-30 MeV. An alternative way to produce it is via a photo-nuclear process, where the cross-section strongly depends on the gamma-ray energy and has a threshold energy between 11-18 MeV that drops sharply above 25 MeV [18]. In this energy range the nucleus acts as a strong absorber. This phenomenon, called the giant dipole resonance, has been interpreted as excitation of collective vibration of the protons against the neutron that ends up creating an electric dipole moment [18]. From the cross-section, it can be estimated that 10^{10} ^{18}F nuclei can be produced in equilibrium after one hour exposure, when $\sim 10^9$ photons/s impinge with an energy in the range of interest. If we consider a 300 pC, 1 GeV, 1 mrad divergence electron beam going through a 1 mm W target placed 5 cm from the source, 6×10^{11} photons/shot will be produced, of which 6×10^8 have an energy between 15 and 25 MeV. With a repetition rate of 10 Hz, 6×10^9 photons/s are delivered making this gamma source an excellent candidate for a laser-driven radioisotope production method.

4.7 Towards a Converging Gamma-Ray Beam

Gamma-rays are particularly hard to focus. This is a problem faced every day in astrophysics where there is the need for x- and gamma-ray focusing optics in telescopes to detect and characterise gamma-ray sources from space, such as supernova explosions [19]. For this purpose gamma-ray lenses based either on Fresnel [20], Bragg (in reflection) or Laue (in transmission) [21] diffraction are used. Their focal lengths are extremely long (from meters up to millions of kilometres [19]). At the moment these lenses are the only solution for astrophysics sources. However, other fields could benefit from converging gamma-ray beams. In x- and gamma-ray imaging for example, beside the detector pixel size and the system geometry, the source size plays a primary role in determining the image spatial resolution. By squeezing the size of the gamma-ray source down to sub millimetre level, it would be possible to have a spatial resolution that could enable on site detection of micro-fractures inside fuel rods in nuclear power plants or the integrity of nuclear waste. Importing from astrophysics the optical solutions would encounter major hurdles mainly because of the size of the optics and the focal length. But on Earth, on the contrary, it may be possible to act on the source to produce a converging beam. This led the ALPHA-X group to propose a new way of producing a focused gamma-ray beam. Bremsstrahlung radiation is emitted in a narrow cone with an average half-angle of $1/\gamma$. By focusing the high energy electrons with magnetic lenses [22], bremsstrahlung beams produced in a target before the focal point can form a converging gamma-ray beam (Figure 4-11).

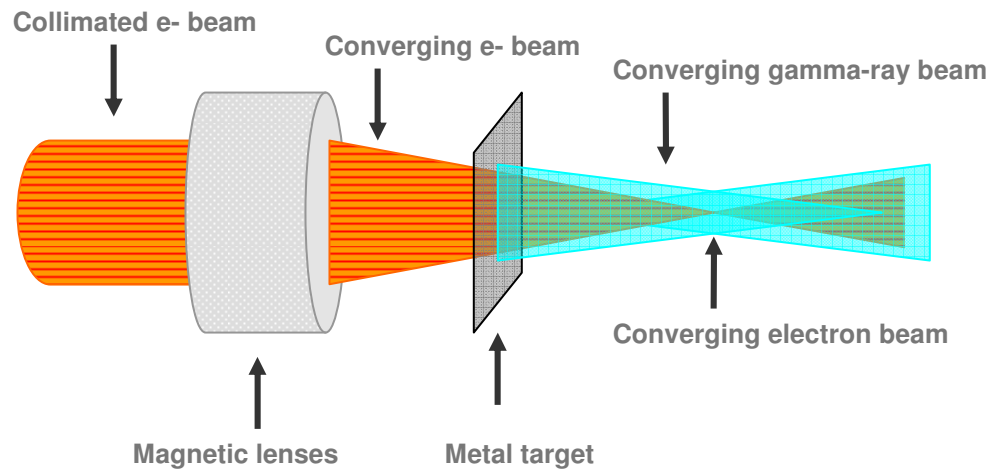


Figure 4-11: Simplified scheme to set-up to produce a converging gamma-ray beam.

To explore the feasibility of the idea and determine the conditions that should be satisfied to produce a converging gamma ray beam, we have performed a series of simulations for mono-energetic electron beams passing through a selection of metal targets. The simulations have been performed with GEANT4, varying the focal length, target material, thickness position and ambient medium. A summary of the simulation parameters are given in Table 4-3.

Parameter	Values	Unit
electron energy	50, 100, 150, 250	MeV
Focal length (FL)	10, 15, 20, 30, 40	cm
material (Z)	Al (13), Cu (29), In (49), W (74)	.-.
Target thickness	1, 2, 5, 10, 20	mm
Source-target distance (for fixed FL)	1, 3, 5	cm
Ambient medium	Air, Water	.-.

Table 4-3: Simulation parameters used in the converging gamma ray beam studies.

The first relevant result can be seen in the energy scan. In these simulations a converging electron beam with a 10 cm focal length, was passed through a 1 mm thick Al target placed 5 cm from the source and co-propagated in air with the emerging bremsstrahlung gamma-ray beam. In Figure 4-12 the r.m.s. gamma-ray beam size is plotted as a function of the distance from the source. For low electron energy (50 MeV) the emerging gamma ray beam diverges while for higher energy electron beams the gamma-ray beam converges. Lower energy electrons are strongly deviated from their converging trajectories, because scattering in the Al foil destroys the convergence. It is apparent that a converging gamma-ray beam can be readily produced by bremsstrahlung using a converging high energy electron beam. For a 1 mm Al foil an energy ≥ 100 MeV is required to achieve a converging beam.

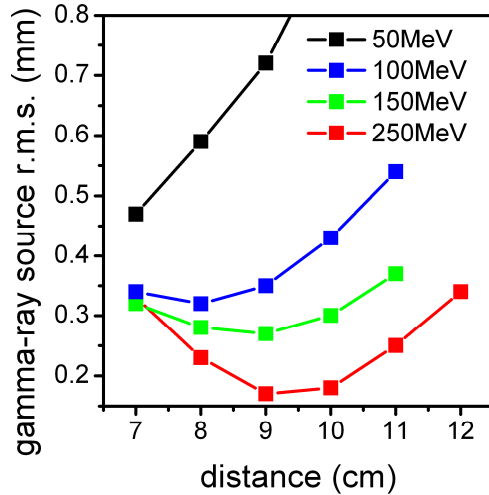


Figure 4-12: Energy scan for 50-250 MeV electron beam with 10 cm focal length.

Having established that high energy electrons are necessary to have a converging gamma beam, all the following simulations have been run for 250 MeV electron beams.

Figure 4-13(a) shows how, changing the focal position (FP) for a fixed source-target distance, it is possible to tune the gamma-beam FL and spot size at the focus. The spot size at focus and the focal position are also strongly affected by the target material, as shown Figure 4-13(b), where the atomic number Z has been increased, resulting in a decrease of the gamma-ray focal length. However, the main effect of changing the target material is to vary the gamma-beam spot size at focus. For Al, Cu and In, the emerging gamma-ray beam converges and the spot size increases with the atomic number. For very high atomic number (tungsten) the gamma-ray beam does not converge anymore. In this last case convergence can be recovered using a higher energy electron beam.

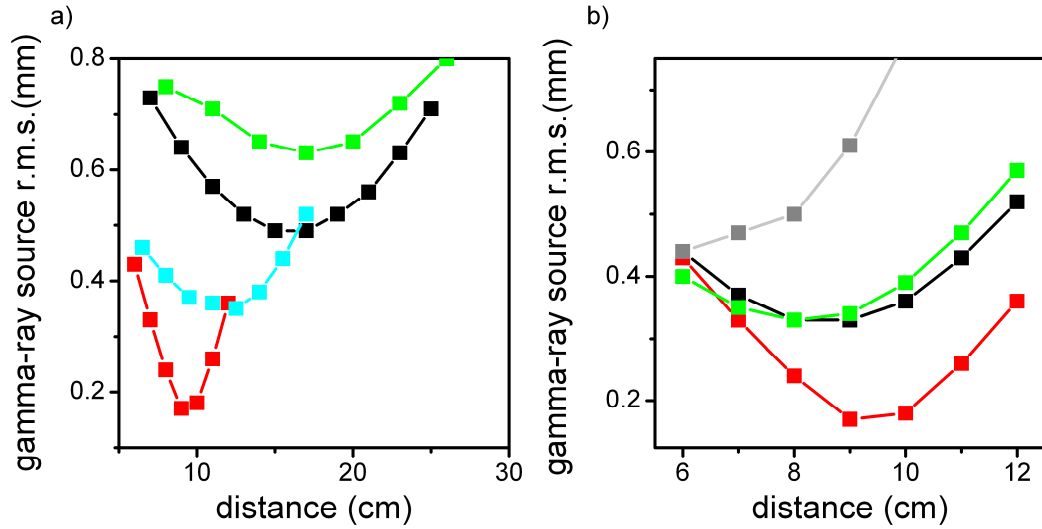


Figure 4-13: GEANT4 simulation results obtained for a 250 MeV electron beam passing through a 1 mm thick solid target placed 5 cm from the source. The electron r.m.s. beam size is 1 mm. a) Bremsstrahlung gamma-ray beam (r.m.s) profile vs distance from electron source obtained for an Al target changing the electron beam focal length: 10 cm (red dots), 15 cm (light blue dots), 20 cm (black dots) and 30 cm (green dots). b) Bremsstrahlung gamma-ray r.m.s beam profile for different target material Al (red dots), Cu (black dots), In (green dots) and W (grey dots) for 10 cm focal length.

Adjusting the relative distance between the source and the metal target also varies the spot size at focus, for a fixed focal length. This can be clearly seen in Figure 4-14, where it is evident that when the relative distance is decreased the spot size increases.

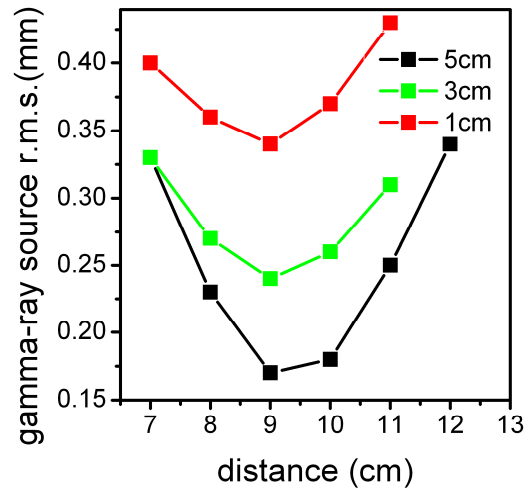


Figure 4-14: The graph shows the simulation results for a 250 MeV electron beam passing through a 1 mm thick Al foil placed at different distances from the source, for a fixed focal length of 10 cm. Both the focal length and the spot size at focus depend on the position of the target.

The other necessary condition for a converging beam is given by the target thickness. Figure 4-15 shows simulation results obtained for different target thickness: for 250 MeV electron energy and Al as a target material, the maximum thickness to produce a converging gamma beam is 1 cm. This maximum thickness also varies with energy, FL and material (Z).

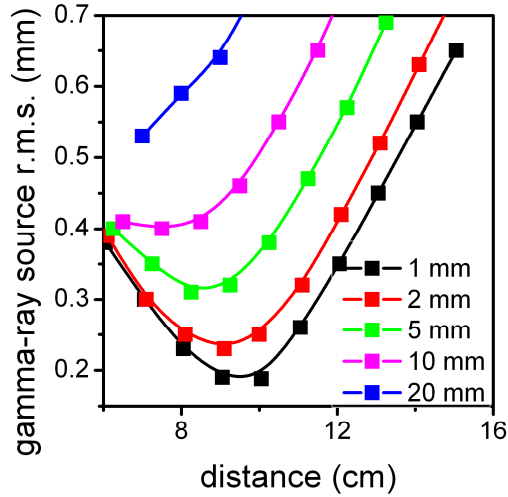


Figure 4-15: Gamma-ray beam profile for different target thickness. The simulations are carried out for an Al target placed 5 cm from the source with FL = 10 cm and an electron energy of 250 MeV.

The actual focal position (FP) does not necessarily overlap with the set focal length (FL). First of all, as already seen in Figure 4-13b, the actual focal position depends on the target material, which is clearly shown in Figure 4-16(a), whereas for a fixed value of FL (10 cm) increasing the atomic number Z , the gamma-ray FP decreases. Figure 4-16(b) shows how increasing the FL of the electron beam, the relative FP (percentage of FP on FL) decreases linearly. Finally, for a fixed 10 cm FL, the FP decreases while increasing the target thickness (Figure 4-16c).

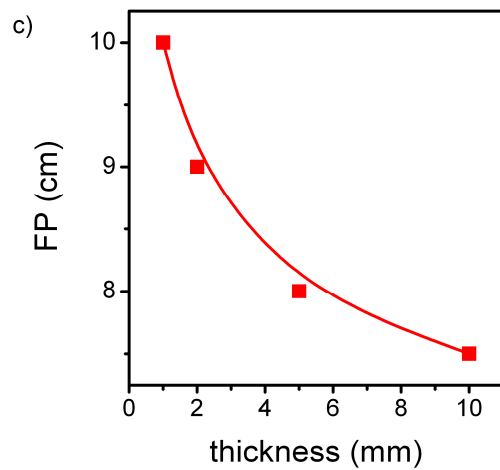
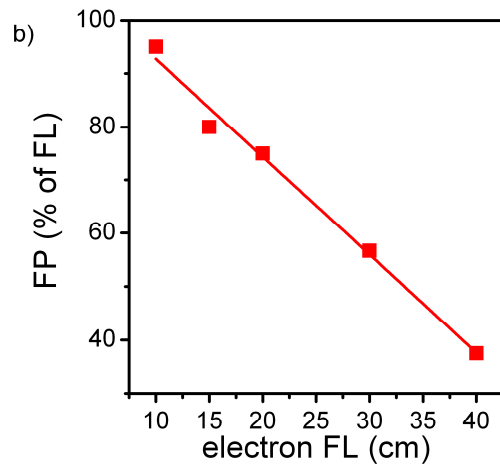
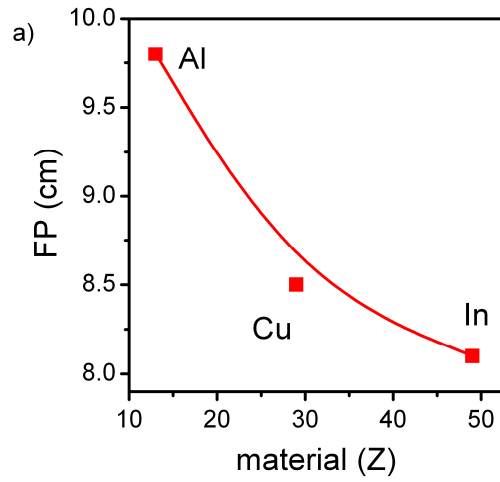


Figure 4-16: FP dependence on different parameters: a) target atomic number, b) electron beam FL, c) target thickness.

In the last set of simulations electrons are deflected away from the gamma-ray beam. In this case the simulated geometry is shown in Figure 4-17: the electron beam is passed through an Al foil placed 1 cm from the source and then bent away using a dipole magnetic field placed between the target and the focal point. The gamma ray beam profile is studied for propagation in two different ambient media: air and water. The results are shown in Figure 4-18: when the electron beam is decoupled from the gamma-ray beam, the spot size is smaller at the focus because no other emission is produced after the interaction with the Al foil. For the simulated geometry when the propagation medium is water the secondary γ -ray emissions from the electrons is stronger because of the higher medium density. To completely avoid the secondary effects of the interaction of the electrons with the ambient medium, a higher magnetic field needs to be applied. Simulations show that for the geometry used with a magnetic field of 0.5 Tm the electrons are not bent enough and the secondary emissions in the water strongly overlaps and disturbs the gamma-ray beam produced by the Al foil and the convergence property is almost lost. Increasing the electrons deviation from the axis with a magnetic field of 1 Tm results in complete decoupling and a gamma beam is produced in the water.

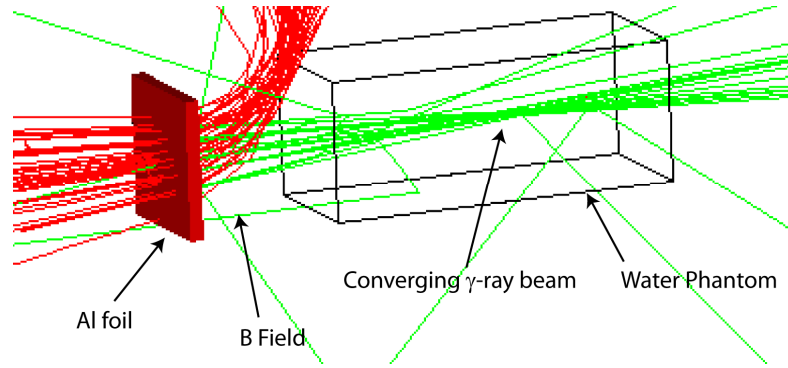


Figure 4-17: Simulation scheme: the red tracks are electrons and green tracks are gamma-rays. The magnetic field deflects the electrons after the Al while the converging γ -ray beam propagates through the water phantom.

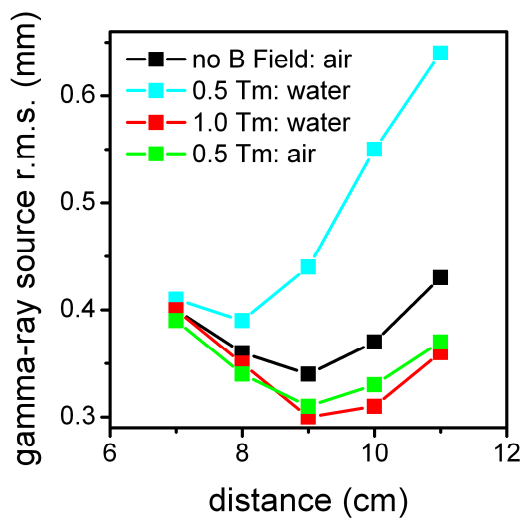


Figure 4-18: Simulations with magnetic field and water.

In summary, we have numerically investigated a scheme to produce a converging gamma-ray beam based on a LWFA driven bremsstrahlung source. In the next sections we overview potential medical applications for this novel source. The idea of producing

a converging gamma from converging electron beam producing bremsstrahlung radiation has been submitted for a patent.

4.8 Converging Gamma-Ray Beam and Radiosurgery: a Possible Application

One of the fields in which a converging gamma-ray beam could be particularly attractive is radiotherapy in cancer treatment. Radiation therapy is one of the most effective ways to treat a tumour before or after surgery, to either shrink the tumour or destroy residual tumour, and to control symptoms and provide pain relief [23]. Despite its wide use in medicine, radiotherapy comes with the concomitant problem of toxicity due to the damage of healthy tissue. The level of toxicity depends strongly on the type of ionizing radiation that is used for the treatment. Three different types of ionizing radiation can be employed, listed in order of decreasing toxicity, are x-rays, electrons and ions. The different toxicity depends on the way the radiation is absorbed inside the body. The energy deposited by x-rays decreases exponentially as the depth increases. Electrons deposit a dose that is almost flat and then falls off quickly [7]. The fall-off point depends on the electron energy, and for conventional 20-30 MeV medical accelerators the penetration depth is only a few cm. Ions, on the other hand, deposit most of their energy at the end of their tracks, in the so called Bragg peak (

Figure 4-19). The Bragg peak position can be tuned by tuning the ion energy [24] in the range of 10-20 cm[7] (Figure 4-20).

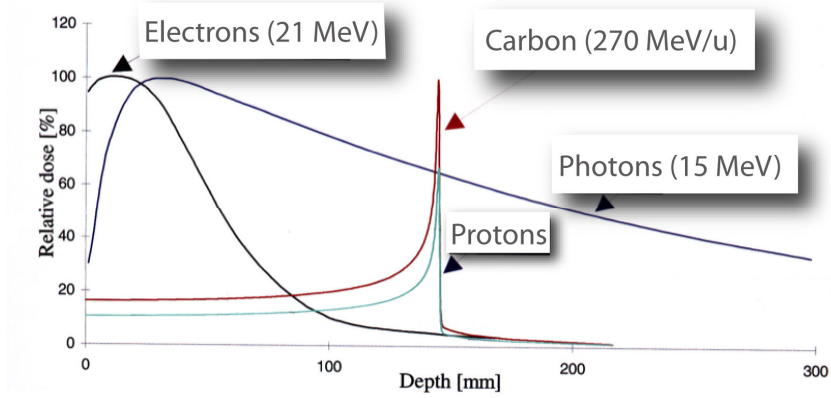


Figure 4-19: Profile of the energy deposition in tissue for electrons, photons and carbon ions. Image source Ref.[25].

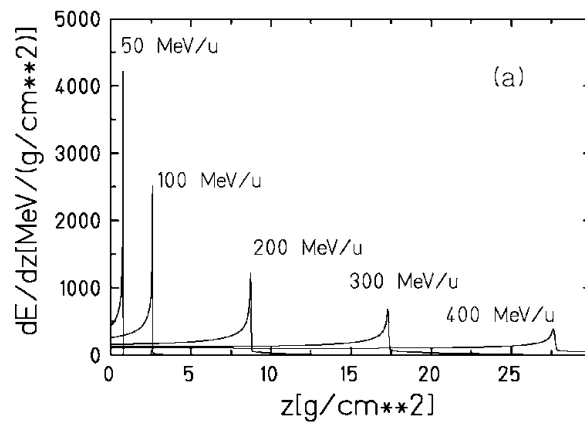


Figure 4-20: Bragg position as function of the ion energy calculated for ^{12}C . Image from Ref. [24]

Electrons cannot currently be used to treat deep seated tumours because they fail to penetrate more than a few cm in water. X-ray and gamma-ray beams, produced via bremsstrahlung by electron beam accelerated with conventional linac [26], can reach the tumour but deposit a high dose in shallow tissue. Ions are widely recognised as providing the best solution. Despite the fact that x-rays are the most toxic it is also the most widely used because ion accelerators are hugely expensive and only few centres can afford the cost. Currently efforts have been made to improve the effectiveness of radiotherapy, in particular x-ray therapy to make it less toxic to healthy tissue. The most important modulator of radiation effects are the total dose, the dose rate, the interval of time between two delivered doses, the specific properties of the organ irradiated and the volume. Taking into account these parameters, stereotactic radiosurgery and radiotherapy methods have been developed to minimize treatment side effects. The peculiarity of stereotactic techniques is the delivery of high doses to the tumour while minimizing irradiation of the surrounding healthy tissue. This is achieved using many collimated gamma-ray beams that overlap in the volume to be treated. Equivalently, a converging gamma-ray beam can be used. Delivering a converging gamma beam could have a significant impact on cancer treatment and, in general, for any application that could benefit from a converging beam.

In the next two sections we review the most popular radiosurgical techniques and then describe an innovative method of delivery a converging gamma-ray beam.

4.8.1 Overview of Radiosurgery Techniques

Radiosurgery is a medical non-invasive treatment used mainly to treat tumours by focusing ionising radiation into the volume to be treated. The term stereotactic in general refers to precisely positioning in three dimensional space the tip of a delicate instrument for biopsy, surgery or radiotherapy [7]. The concept of radiosurgery was introduced by a professor in neurosurgery, Leksell, in Sweden in 1951. In the initial idea an arc structure carried the treatment tool, i.e. an x-ray tube. The centre of the arc coincided with the target point, so that the arc could be rotated about its axis while the x-ray beam points at the target. The gist of the system is that each x-ray beam delivers a harmless dose everywhere but where the beams cross it delivers a destructive dose to the tumour. The first prototype was created in 1967 in Sweden by Leksell and Larson [7]. Instead of x-ray tubes the device consists of multiple cobal-60 beams (201) sharply collimated to create a small almost spherical treatment volume with sharp edges (see Figure 4-21). This was the birth of one of the best known stereotactic radiosurgery methods: the gamma knife. The most important aspects of this technique are the patient positioning and the source alignment to ensure that the target is treated. The handling and loading of the cobalt sources represents an important challenge for applying the gamma knife. The system has been redesigned a few times and developed to improve the shielding, the source positioning and accuracy. Starting from an isotropic source, a collimated beam is obtained through a complex system of filters. The overlapping of the collimated beams defines a high dose deposition volume that represents the focal point of the system. The

aperture size of the collimators defines the size of the beam at focus. Currently the gamma knife is mainly used for treating brain tumours, a frame ensures the correct positioning of the patient and no on line imaging control is required. The most recent model, introduced by Elekta in 2006, is Leksell Gamma Knife Perfexion. It is equipped with robotic automatic source positioning and is able to treat all intracranial and even cerebral column [7].

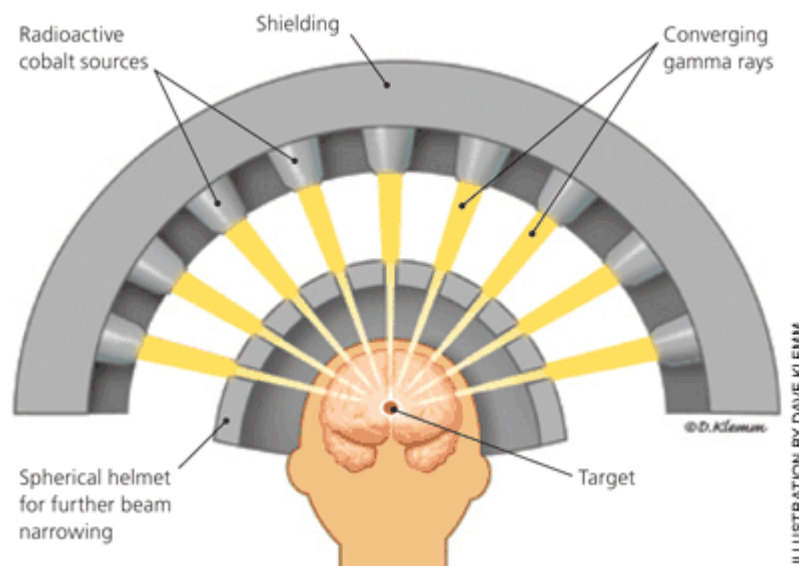


Figure 4-21: Gamma knife image from Ref. [27].

An alternative radiosurgery system is the modified linac radiosurgery system known as the Cyberknife (Accuray Inc.) [28]. This technology is based on a compact linear accelerator mounted on a robotic arm with fine movement ability (Figure 4-22). Hundreds of micro pencil beams and thousands of possible irradiation angles make possible the delivery of high radiation doses to a target volume while minimizing the

exposure of normal tissue. The system is frameless and requires a real-time imaging system to monitor the patient positioning that represents the main difference compared with the gamma-knife.



Figure 4-22: Cyberknife from Ref. [29].

A third type of radiosurgery uses ions instead of x-rays. As already pointed out, the peculiarity of ions is that on going through the matter they deposit most of their radiation at the end of their path, in the so called Bragg peak. The depth at which the Bragg peak appears for a given material depends on the initial energy of the ion beam, therefore by tuning the ion beam energy it is possible to target a well defined volume. This last method is not widely available because of the high cost, >£100 million, of ion accelerators [30].

4.9 The Converging Gamma-Ray Beam as a Novel Generation of Gamma-Knife

Following on the previous section where we described a converging gamma-ray beam as an interesting alternative to ion therapy, we consider a LWFA method that avoids the need to handle radioactive sources. This keeps the cost low while preserving the quality of the x-ray beams. The delivery of a converging gamma-ray beam does not depend on the way in which the electron beam is accelerated. However, as simulations show, only high energy electrons that are converging can generate a converging gamma ray beam because of the $1/\gamma$ dependence of the bremsstrahlung emission angle, but electron beams of 100 MeV or higher are required. As mentioned, medical linear accelerators can provide electrons up to a few tens of MeV, and higher energy implies an increase in cost and size, which detracts from its attractiveness. A LWFA driving the converging gamma beam, on the other hand, provides a high energy electron beam at low cost and small size. A preliminary numerical study of the expected dose deposition for a converging gamma beam is shown in Figure 4-23.

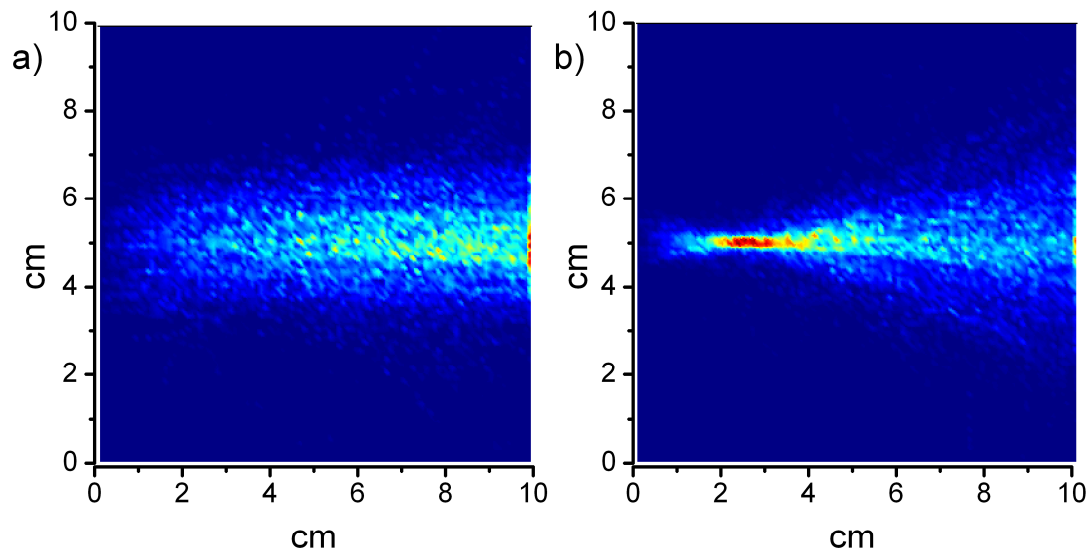


Figure 4-23: Deposited energy distribution in a 20 cm water phantom by gamma-rays produced via bremsstrahlung from 250 MeV electrons passing through a 1 mm Al target a) for 1 mrad divergence and b) for a focused beam. The beam propagates from the left side.

The size of a tens of MeV to GeV LWFA is a few millimetres to a few centimetres long. Furthermore, the laser beam path can be easily modified using standard optics, which would simplify the mechanical structure. Moreover, it is worthwhile noticing that the high energy electron beam could also be used for treatment. Higher electron energy results in higher penetration depth. If no decoupling magnetic field is applied after the electrons-solid target interaction both co-propagating converging gamma and electron beams could be a completely new way to treat cancer. The idea of using very high energy electrons (VHEE) [31-33] for cancer therapy has already been explored and the idea kept in a drawer because of the practical limitation to the feasibility due to the already mentioned size and cost. Here, there is now the possibility with a LWFA

accelerator not only to deliver the VHEE beam but also to couple it with a converging gamma-beam. The combination could potentially have interesting effects that could be investigated.

Another remarkable property of both electron and gamma-ray beams delivered via LFWA is the extremely short pulse length: the electron bunch length is few femtoseconds and the produced bremsstrahlung gamma-ray beam of the order of picoseconds. However, it is necessary to take into account that passage of the electron beam through the body itself is expected to produce a lengthening of the bunch. To estimate it we have used GEANT4 to simulate a very simple geometry, a monoenergetic 150 MeV electron beam passing through a phantom. The phantom made of 20 x 20 x 20 cm of water reproduces the human body. The simulations have been carried out for 10^4 particles with an initial bunch length of 3 μm . As electrons pass through the phantom they lose energy and the beam is no longer monoenergetic. The evolution of the electron spectrum is shown in Figure 4-24. The broadening of the energy spectrum implies a longer bunch length. From the distribution of the time of flight of the electron beam we have calculated the bunch length at different depth inside the phantom (Figure 4-25). From the simulations it appears that the bunch length becomes of the order of picoseconds after interacting with about 10 cm of water, which is still in the sub-nanosecond range and three orders of magnitude shorter than the bunch length of electron beam produced by a conventional accelerator.

Recently, bioelectric studies have recognised intense nanosecond and sub-nanosecond electric pulses as a new tool for cancer treatment and gene therapy [34]. The duration of the pulse is a key factor because to pass through the cell membrane the electric pulse rise-time needs to be shorter than 100 ns, that is the charging time of the membrane itself [34]. However, besides its potentials this treatment has disadvantages due to the invasive approach in which the electric field is delivered (with implanted electrodes) that causes discomfort to the patient. Currently, picosecond impulse radiating antennas are investigated as a method of delivering sub-nanosecond pulses for non-invasive delivery of electrical pulses to skin tumours [35]. However, the ultra-short electron beam produced by LWFA, with bunch length properties described in the previous paragraph, could be an alternative way of delivering intense electric pulses to the tumour. The main advantage could arise from using an electron beam from a LWFA that is non invasive and both shallow and deep tumours could be treated. Furthermore, it may be worthwhile studying its combined effect with radiation therapy.

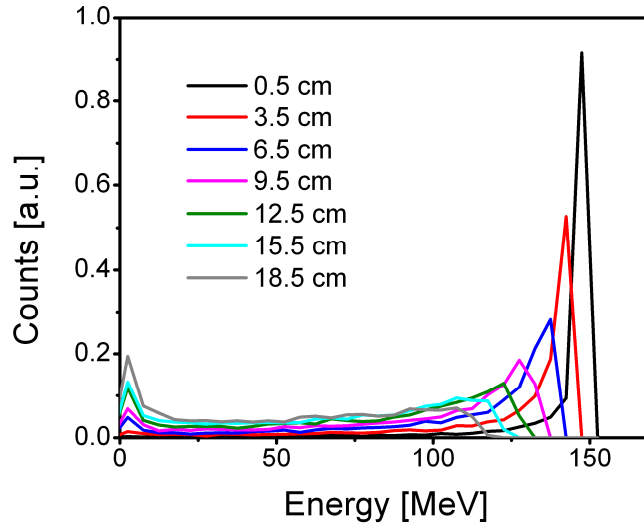


Figure 4-24: Electron spectrum evolution while interacting with phantom water

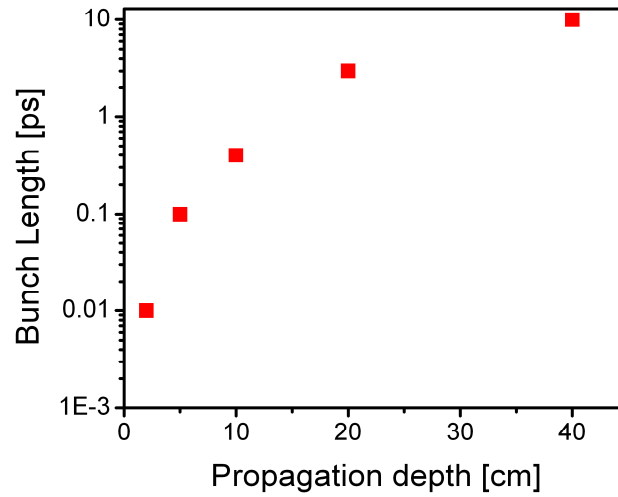


Figure 4-25: LWFA electron bunch length evolution as a function of the propagation depth in a water phantom.

4.10 Conclusions

In the first part of the Chapter we investigated the possibility of manipulating the bremsstrahlung gamma-ray beam by modifying the electron beam and target properties. We have provided the scaling properties of the bremsstrahlung radiation as a function of the electron beam and target properties. We have obtained experimental results in good agreement with numerical predictions (Figure 4-8). We have imaged the gamma-ray beam through 5 cm of lead (Figure 4-9) providing the experimental evidence of the possibility of using the LWFA bremsstrahlung gamma-ray source to probe dense matter. Using simulations we have provided the scaling required for radioisotope production. Therefore, the afforded tuneability makes the LWFA driven bremsstrahlung source attractive, firstly as an ultra-compact light source for dense matter probing, and secondly for radioisotope production.

In the second part of the Chapter we have explored the possibility of generating a converging gamma-ray beam from a LWFA bremsstrahlung source. With GEANT4 simulations we observe that, for a converging electron beam interacting with a suitably chosen metal target, it is possible to produce a converging gamma-ray beam. Reproducing experimentally the simulated conditions should be relatively easy and give a proof for an important tool for science and technology. The possibility of a converging gamma-ray beam suggests many new applications of the LWFA technology. We have discussed possible medical applications in cancer treatment and the development of a

novel concept of radiosurgery, but many further examples could be proposed e.g. high spatial resolution scanning of dense material such as *in situ* radiography of nuclear fuel rods.

Finally we have speculated about the possible interest in studying the combined effect of a converging gamma-ray beam and the ultra-short electron bunch in cancer treatment, overlapping radiotherapy and sub-nanosecond electric pulse effects.

References

1. Hartemann F.V., Brown W.J., Gibson D.J., Anderson S.G., Tremaine A.M., Springer P.T., Wootton A.J., Hartouni E.P., and Barty C.P.J., "High-Energy Scaling of Compton Scattering Light Sources", *Physical Review Special Topics - Accelerators and Beams*, **8**(10), 100702 (2005)
2. Jackson J.D., *Classical Electrodynamics*, ed. J. Wiley and Son New York. (1999)
3. Edwards R.D., *et al.*, "Characterization of a Gamma-ray Source Based on a Laser-Plasma Accelerator with Applications to Radiography", *Appl Phys Lett*, **80**(12), 2129 (2002)
4. Agostinelli S., *et al.*, "GEANT4-a Simulation Toolkit", *Nucl Instrum Meth A*, **506**(3), 250 (2003)
5. Koch H.W. and W. M.J., "Bremsstrahlung Cross-Section Formulas and Related Data", *Rev. Mod. Phys.*, **31**(4), 920 (1959)
6. Glinec Y., *et al.*, "High-Resolution Gamma-ray Radiography Produced by a Laser-plasma Driven Electron Source", *Phys Rev Lett*, **94**(2), 025003 (2005)
7. Halperin E.C., Perez C.A., and Brady L.W., *Principles and Practice of Radiation Oncology*, ed. L.W.W. Wolters Kluwer. (2008)
8. *Medical Radioisotopes Production without a Nuclear Reactor*. Available from: http://www.laka.org/medical_isotopes.html. (2010)

9. Baldwin G.C. and Klaiber G.S., "Photo-Fission of Heavy Elements", *Phys. Rev. E*, **71**(1), 3 (1947)
10. Cowan T.E., *et al.*, "Photonuclear Fission from High Energy Electrons from Ultraintense Laser-Solid Interactions", *Phys Rev Lett*, **84**(5), 903 (2000)
11. Reed S.A., *et al.*, "Photonuclear Fission with Quasimonoenergetic Electron Beams from Laser Wakefields", *Appl Phys Lett*, **89**(23), 231107 (2006)
12. Giulietti A., *et al.*, "Intense Gamma-ray Source in the Giant-Dipole-Resonance Range Driven by 10-TW Laser Pulses", *Phys Rev Lett*, **101**(10), 105002 (2008)
13. Hooker C.J., *et al.*, "Commissioning the Astra Gemini Petawatt Ti:sapphire Laser System", *CLEO/QELS 2008*, 1 (2008)
14. Ibbotson T.P.A., *et al.*, "Investigation of the Role of Plasma Channels as Waveguides for Laser-Wakefield Accelerators", *New J Phys*, **12**, 045008 (2010)
15. Llopart X., Ballabriga R., Campbell M., Tlustos L., and Wong W., "Timepix, a 65k Programmable Pixel Readout Chip for Arrival Time, Energy and/or Photon Counting Measurements", *Nucl Instrum Meth A*, **581**(1-2), 485 (2007)
16. Cipiccia S., *et al.*, "Timepix in Compton Side Scattering scheme: A Promising Single-Shot Tool for Ultra-Fast, High Flux, Broad Energy Range X-ray Spectroscopy Based Compton Side-Scattering", *J Appl Phys*, **submitted** (2011)
17. Janek S., Svensson R., Jonsson C., and Brahme A., "Development of Dose Delivery Verification by PET Imaging of Photonuclear Reactions Following High Energy Photon Therapy", *Phys Med Biol*, **51**(22), 5769 (2006)
18. Chomaz P. and Frascaria N., "Multiple Phonon Excitation in Nuclei: Experimental Results and Theoretical Descriptions", *Physics Reports*, **252**(5-6), 275 (1995)
19. Smither R.K., Abu Saleem K., Roa D.E., Beno M.A., Von Ballmoos P., and Skinner G.K., "High Diffraction Efficiency, Broadband, Diffraction Crystals for Use in Crystal Diffraction Lenses", *Exp Astron*, **20**(1-3), 201 (2005)
20. Krizmanic J., Skinner G., and Gehrels N., "Formation Flying for a Fresnel Lens Observatory Mission", *Exp Astron*, **20**(1), 497 (2005)

21. Pellicciotta D., Frontera F., Loffredo G., Pisa A., Andersen K., Courtois P., Hamelin B., Carassiti V., Melchiorri M., and Squerzanti S., "Laue Lens Development for Hard X-rays (> 60 keV)", *Ieee T Nucl Sci*, **53**(1), 253 (2006)
22. Anania M.P., *et al.*, "The ALPHA-X Beam Line: towards a Compact FEL ", *Proceedings IPAC 2010 TUPE052*, (2010)
23. Hoskin P.J., Oxford University Press.: Oxford (2003)
24. Krämer M., Jäkel O., Haberer T., Kraft G., Schardt D., and Weber U., "Treatment Planning for Heavy-ion Radiotherapy: Physical Beam Model and Dose Optimization", *Phys Med Biol*, **45**(11), 3299 (2000)
25. Available from: <http://www.quantumdiaries.org/author/cern/>
26. Whittum D.H., *Reviews of Accelerator Science and Technology*, ed. A.W. Chao and W. Chou. Vol. 2 Medical Applications and Accelerators Singapore: World Scientific Publishing Co. Pte. Ltd. (2009)
27. Available from: <http://www.aafp.org/afp/2008/1201/p1254.html>
28. Available from: <http://www.cyberknife.com/>
29. Available from: <http://www.upmccancercenters.com/radonc/cyberknife.cfm>
30. Ledingham K.W.D., Galster W., and Sauerbrey R., "Laser-Driven Proton Oncology : A Unique New Cancer Therapy?", *British Journal of Radiology*, **80**(959), 855 (2007)
31. Papiez L., "Image-Guided IMRT and Very High Energy Electrons (VHEE)", *Med Phys*, **33**(6), 2204 (2006)
32. Yeboah C., Sandison G.A., and Moskvina V., "Optimization of Intensity-Modulated Very High Energy (50-250 MeV) Electron Therapy", *Phys Med Biol*, **47**(8), 1285 (2002)
33. Fuchs T., Szymanowski H., Oelfke U., Glinec Y., Rechatin C., Faure J., and Malka V., "Treatment Planning for Laser-Accelerated Very-High Energy Electrons", *Phys Med Biol*, **54**(11), 3315 (2009)
34. Altunc S., "Subnanosecond Pulsed-Power Generated Electric Field for Cancer Treatment", *Nuclear & Plasma Sciences Society*, 34 (2009)

35. Altunc S., Baum C.E., Christodoulou C.G., and Schamiloglu E., "Spatially Limited Exponential Lens Design for Improved Focusing of an Impulse", *Proc. URSI General Assembly*, (2008)

Chapter 5

5.1 Discussion of Synchrotron Radiation from Betatron Oscillation of LWFA Electrons

Betatron oscillations of electrons during LWFA have already been proven to be a new, compact, bright synchrotron source [1-3]. Here we have demonstrated both theoretically and experimentally that when electrons interact with the laser pulse, during the acceleration, a resonance between the laser and a harmonic of the betatron frequency leads to a growth of the betatron oscillation amplitude motion. In the harmonically betatron resonant (HBR) regime the synchrotron emission is strongly enhanced by increasing the oscillation amplitude and consequently also the number of photons emitted and the critical energy. The radiation spectrum stretches from tens of keV to hundreds of keV with significant emission in the MeV range [3]. The radiation pulse duration has been estimated from OSIRIS simulations to be of the order of few femtoseconds. Looking at the position of the HBR source in the brilliance plot shown in

Figure 5-1 and Figure 5-2 it is immediately clear that this few centimetres long source has peak brilliance as high as third generation light sources. Moreover,

comparing the two graphs it can be seen that the HBR source is placed in a region of the energy-pulse duration space where no comparable sources exist or are planned for in the near future. For conventional light sources, technological and economical limitations prevent the access to the MeV photon energy and femtosecond pulse duration ranges. Furthermore, the HBR source, using a higher power laser, could scale up in energy to exceed 10 MeV photon energies. The HBR source represents at the moment the only available high brightness tool with a suitable energy and time resolution to allow time resolved exploration of nuclear processes, which until now has not been possible. As already mentioned, the small size and the relative low cost makes the source attractive for many other applications, such as radioisotope generation, dense matter probing and imaging.

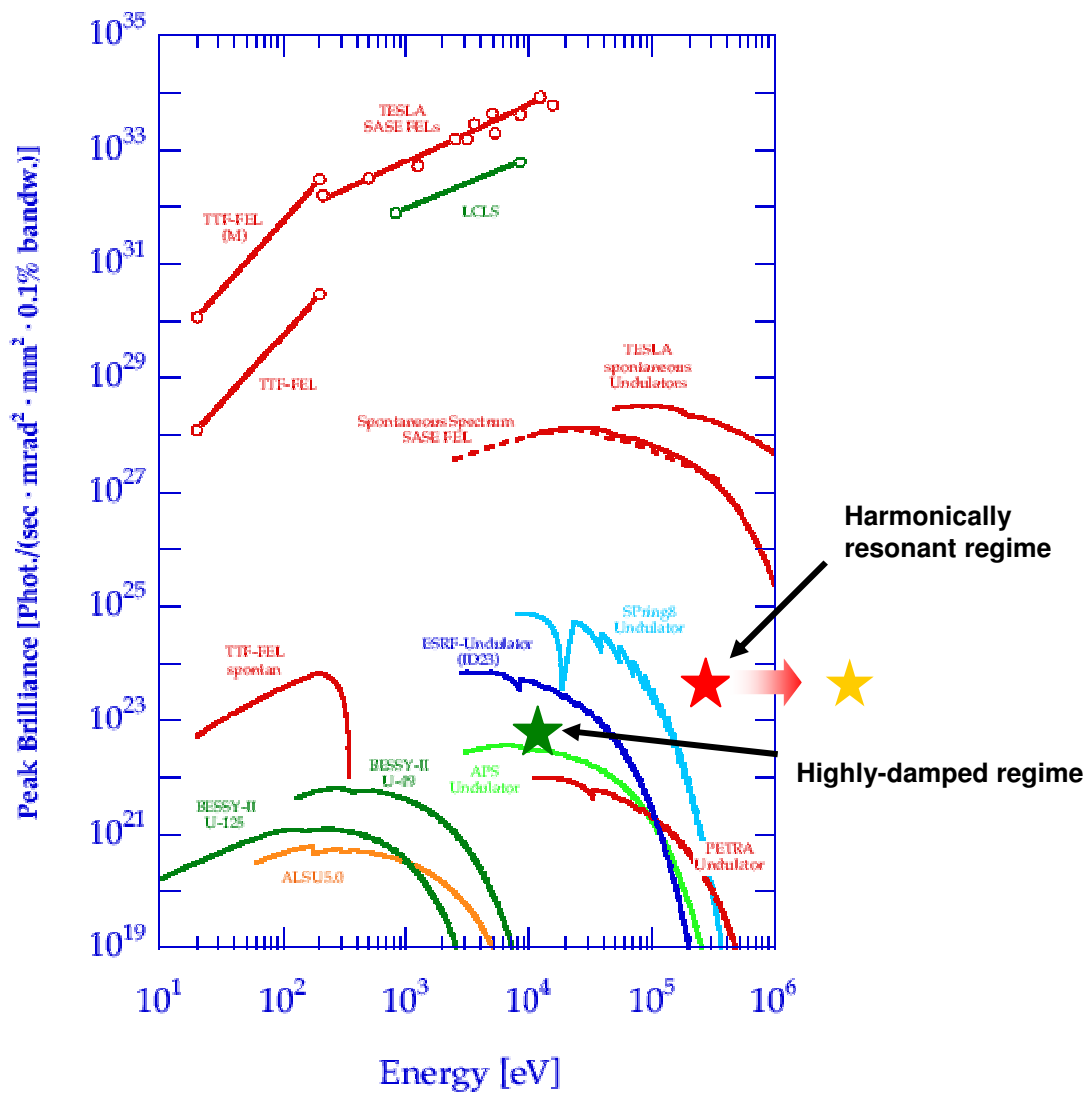


Figure 5-1: Peak brilliance as a function of the photon energy of third and fourth generation light sources. The stars represent the peak brilliance of the betatron source: green for the highly damped regime, red for the HBR regime and yellow the possible brilliance when scaling up in energy. Image taken from Ref. [4] and modified.

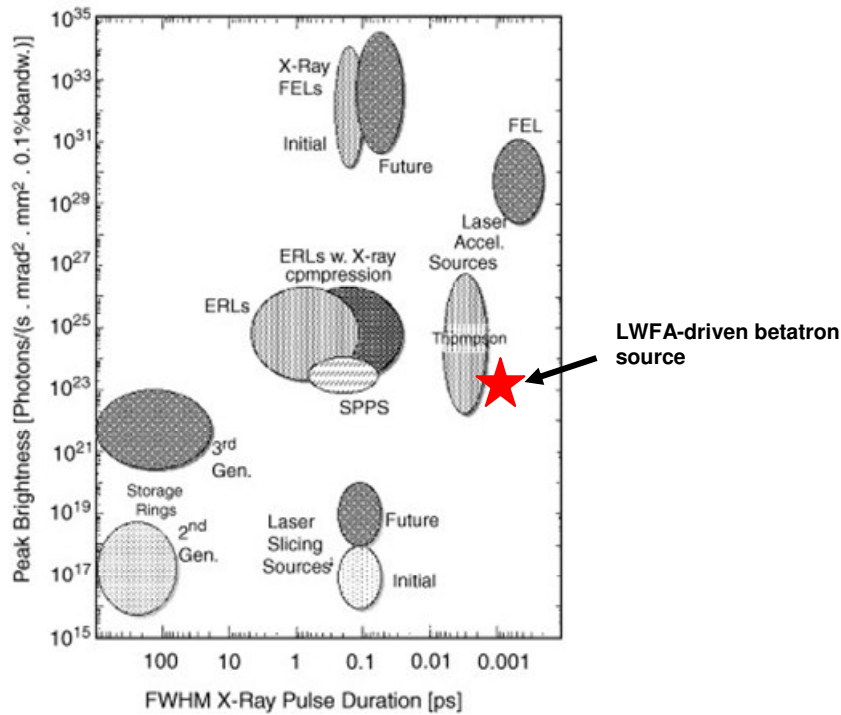


Figure 5-2: Peak brilliance as a function of the pulse duration for second, third and future generation synchrotron light sources compared with a LWFA-driven betatron source (red star). Image taken from Ref. [5] and modified.

5.2 Next Challenges for HBR Sources

The HBR source has proven to be a very interesting source with high potential both to widen scientific research, because of its unique properties (energy and pulse duration) and to make light sources more available through smaller size and lower cost. Even if the tuning knobs of the source have been identified, further studies are necessary to completely master the tuning parameters and adjust the properties depending on the specific requirements. One significant improvement would be to increase the brilliance,

both peak and average. The average is mainly controlled by the high power laser repetition rate and not much can be done about this but to wait for laser technology to advance. An increase of the peak brilliance can be obtained by increasing the number of betatron oscillations. We can imagine different possible ways to do it and speculate about possible scenarios, for example:

Bubble size manipulation: using a tailored longitudinal density profile has been proved to be a good technique to tune the electron energy controlling the acceleration process [6]. The paper reports an experiment where they used a high density gas jet as an injector and a lower density capillary as an accelerator. Basically, in the first stage of acceleration the higher density corresponds to smaller group velocity of the laser and the electrons can be easily injected. The lower density of the second stage gives a longer dephasing length and higher electron energy can be reached. This idea could be used also to control the betatron oscillation and the synchrotron radiation properties. Controlling the bubble size and shape acting on the plasma density could lead to an increasing in the total number of oscillations that is to higher photon emission flux.

Laser-electron interaction in vacuum: when HBR occurs the electron beam is immersed in the laser pulse. It could be interesting to develop a scheme in which the electrons, after leaving the plasma, interact a second time with a laser pulse (that could be the same responsible for the acceleration or a second pulse synchronized and focused just after the plasma). With a second interaction the number of oscillation cycles and therefore the emission could be substantially improved.

Compact SASE FEL [7]: the interaction of the electrons with the betatron radiation can cause the micro-bunching of the electron beam at dephasing. This, in turn, can lead to coherent emission at the fundamental and harmonics of the betatron frequency [8] as in a SASE FEL.

In the eventuality of micro-bunching we can imagine that it will be possible to generate sub-femtosecond betatron x-ray pulses. This would be an important outcome, a useful tool for a further insight into the ultrafast world (i.e. nuclear processes) currently unapproachable with femtoseconds scale resolution.

It could be interesting to combine the HBR outcome with other techniques, for example coupling the betatron radiation with conventional undulators, sending the pre micro-bunched electron beam inside an insertion device, or using the betatron radiation to seed an FEL to produce an x-ray laser.

Many other ideas are formulated and investigated inside the ALPHA-X group that is moving forward to explore different possible enhancements and uses of the HBR source.

5.3 Summary of Bremsstrahlung Radiation Produced by LWFA Electrons

Bremsstrahlung radiation is just synchrotron radiation, but has different properties: broader bandwidth, longer pulse duration and a poorer brilliance. However, we have shown by simulation the possibility of tuning the bremsstrahlung emission to make it a useful tuneable tool for a variety of applications and currently the only ultra compact source with significant emission in the tens of MeV photon range. The main result of the study is the possibility, not available for the brighter LWFA driven synchrotron sources, to produce, by bremsstrahlung process, a converging gamma-ray beam. The conceptual idea to interact a converging electron beam with a radiator before the focal point to generate a converging gamma-ray beam, has been tested numerically giving excellent results and needs now to be proven experimentally. Once the proof of concept has been done then many improvements could be thought of, for example to increase the maximum target thickness. As already seen, this is limited by the focusing properties of the electron beam which in turn depends on the electron energy. A way of realising a converging gamma-beam using a thicker target to increase the photon emission could be to control the dispersion of the electromagnetic cascade by immersion of the radiator in a focusing magnetic field. This solution is worthwhile to be explored also for the possibility, using dispersing magnetic fields, of selecting gamma-ray looking at different angles that would add another degree of tuneability making the source even more attractive.

5.4 Understanding the Potential Market and Impact

One of the main attractive applications of a converging gamma-ray beam is for radiation therapy using it as a tool for a novel gamma-knife. To have an idea of the possible impact we can speculate on the market and impact of current gamma-knife technology. An interesting paper is available in the literature about the standard gamma knife economical advantages compared with standard surgical techniques written by Cho et al. in Ref. [9]. Cho studied 174 patients with benign cranial tumours, 94 of which underwent open surgery, whereas 80 underwent gamma knife radiosurgery to destroy the tumours. Direct and indirect costs are compared. Direct costs comprised of intensive care unit cost, ward cost, operating room cost and outpatient visit. Indirect costs included loss of working days and mortality. What they found is that most of the socioeconomic costs with open surgery come from indirect costs of workdays and mortality. From the study the gamma knife it emerges that it is a worthwhile treatment for reducing loss of workdays, complications and mortality, to achieve a better cost-effectiveness. A year after Cho's paper, Griffiths et al. [10] carried out a study on gamma knife costs and compared it to stereotactic radiosurgery (SRS) based on modified linacs. A modified linac is a linac equipped with hardware and software so that it can produce a collimated gamma beam (Cyberknife [4] is an example). The analysis takes into account capital purchase, annual maintenance charges, equipment life expectancy and refurbishment costs (the cobalt source reload for the Gamma knife). The result shows that the Gamma knife may be competitive with modified linacs only if the

demand for SRS is sufficiently high to fully use the equipment working time. This is due to the fact that a modified linac is much more versatile and can be used also for other radiation treatment, not only in the cranial area and stereotactic radiosurgery. Extracranial radiosurgery is still largely an emerging application but has enormous potential as a standard treatment option [11] as shown by results for treatment of liver [12], lung [13] and spine [14] tumours.

The tool that we are proposing here has the potential to be a third valid option with additional pros compared with the two SRS techniques. As in a modified linac, a LWFA based gamma knife is versatile and could be used to treat tumours not only localised in the cranial area, and it does not require external radioactive sources. Moreover, it can be used to generate either converging or diverging gamma ray beams, or just electron beams for different radiotherapy applications. In addition, it is more compact and flexible than a standard linac, since bending the laser light with mirrors is much easier than bending electrons with heavy magnets and the radiation source is just a small region of the interaction point with the plasma thus, the radiation shielding will be much simpler [15]. Moreover, LWFA based gamma knife can provide a much higher energy than medical linacs and therefore it could be used also just to drive very high energy electron cancer therapy [16], which is forecast as a promising future radiotherapy [16].

At the moment there are nearly 20,000 accelerators in operation worldwide, and ~12,000 are used for medical and industrial applications [17]. Their market has been estimated to exceed \$3.5 billion per year [18]. By comparing the price of a LWFA with

that of a medical linac, (around \$1 million), the LWFA has a very good chance of conquering the market and, with the potential decrease in the future of the cost of laser based therapy technology, to expand the market, becoming more available to smaller size medical centres. The decrease of the cost of the laser based therapy technology could arise either directly from a decrease of the laser cost, or from an enhancement in the repetition rate, i.e. with diode laser technology, that will allow driving a single laser independently, or simultaneously more than one therapy station, which means that more patients can be treated per year. This could significantly decrease the NHS costs, give rise to spin-off companies and create new markets. Most important the treatment potentially has a very low toxicity and, with the potential of decrease the waiting time, it could strongly improve the quality of life.

References

1. Rouse A., *et al.*, "Production of a keV X-ray Beam from Synchrotron Radiation in Relativistic Laser-Plasma Interaction", *Phys Rev Lett*, **93**(13), 135005 (2004)
2. Kneip S., *et al.*, "Bright Spatially Coherent Synchrotron X-rays from a Table-top Source", *Nat Phys*, **6**(12), 980 (2010)
3. Cipiccia S., *et al.*, "Gamma-Rays from Harmonically Resonant Betatron Oscillations in a Plasma Wake", *Nat Phys*, **7**(11), 867 (2011)
4. Available from:
http://hasylab.desy.de/facilities/sr_and_fel_basics/fel_basics/tdr_spectral_characteristics/index_eng.html
5. Miao J., Chapman H.N., Kirz J., Sayre D., and Hodgson K.O., "Taking X-ray Diffraction to the Limit: Macromolecular Structures from Femtosecond X-Ray

- Pulses and Diffraction Microscopy of Cells with Synchrotron Radiation", *Annual Review of Biophysics and Biomolecular Structure*, **33**, 157 (2004)
6. Gonsalves A.J., *et al.*, "Tunable laser plasma accelerator based on longitudinal density tailoring", *Nat Phys*, **advance online publication** (2011)
 7. Bonifacio R., De Salvo L., Pierini P., Piovella N., and Pellegrini C., "Spectrum, temporal structure, and fluctuations in a high-gain free-electron laser starting from noise", *Phys Rev Lett*, **73**(1), 70 (1994)
 8. Whittum D.H., Sessler A.M., and Dawson J.M., "Ion-channel laser", *Phys Rev Lett*, **64**(21), 2511 (1990)
 9. Cho D.Y., Tsao M., Lee W.Y., and Chang C.S., "Socioeconomic costs of open surgery and gamma knife radiosurgery for benign cranial base tumors.", *Neurosurgery*, **58**(5), 866 (2006)
 10. Griffiths A., Marinovich L., Barton M.B., and Lord S.J., "Cost analysis of Gamma Knife stereotactic radiosurgery", *International Journal of Technology Assessment in Health Care*, **23**(4), 488 (2007)
 11. Hoffelt S.C., "Gamma Knife vs. CyberKnife", *Oncology Issues*, **21**(5), 18 (2006)
 12. Katz W.A., Carey-Sampson M., Muhs A.G., Milano M.T., Schell M.C., and Okunieff P., "Hypofractionated stereotactic body radiation therapy (SBRT) for limited hepatic metastases", *International Journal of Radiation Oncology*Biophysics*, **67**(3), 793 (2007)
 13. Wulf J., Hädinger U., Oppitz U., Thiele W., Ness-Dourdoumas R., and Flentje M., "Stereotactic radiotherapy of targets in the lung and liver.", *Strahlenther Onkol.*, **177**(12), 645 (2001)
 14. Degen J.W., Gagnon G.J., Voyadzis J.M., McRae D.A., Lunsden M., Dieterich S., Molzahn I., and Henderson F.C., "Cyberknife stereotactic radiosurgical treatment of spinal tumors for pain control and quality of life", *J Neurosurg Spine*, **2**(5), 540 (2005)
 15. Kinoshita K., Hosokai T., Ohkubo T., Maekawa A., Zhidkov A., and Uesaka M., "Development of a laser-driven plasma cathode for medical applications", *Laser Physics*, **16**(4), 660 (2006)

16. DesRosiers C., Moskvina V., Cao M., Joshi C.J., and Langer M., "Laser-plasma generated very high energy electrons in radiation therapy of the prostate - art. no. 688109", *Commercial and Biomedical Applications of Ultrafast Lasers VIII*, **6881**, 88109 (2008)
17. Silari M., "applications of particle accelerators in medicine", *Radiation Protection Dosimetry*, **146**(4), 440 (2011)
18. Department of Energy W., D.C., "Accelerators for America's future", (2010)

Appendix:

Osiris:

Osiris [1] is a fully relativistic, multi-dimensional object oriented particle-in-cell (PIC) code. PIC codes model plasmas as particles which interact self-consistently with their own and external electromagnetic fields [2]. Computational limits are imposed by the limited number of particle can be followed, which is small compared with the huge number of particle encountered in laboratory plasmas [2]. For this reason each particle in the numerical simulation represents many particles in real plasma (superparticle).

PIC codes have three steps in the main iteration loop [3]. The first is the deposit of particles, where some particle quantity, such as a charge, is accumulated on a grid via interpolation to produce a source density. The second step is the field solver, which solves Maxwell's equations or a subset of them to obtain the electric and/or magnetic fields from the source densities. The fields are calculated at defined grid points. Finally, when the fields are obtained, the particle forces are found by interpolation from the grid, and the particle moved using Newton's second law and the Lorentz force.

PIC codes are used in almost all areas of plasma physics and also in cosmology, astrophysics, accelerator physics and semi-classical quantum simulations.

Osiris and in general PIC codes are powerful tools but have a number of weaknesses. For example it is challenging to model large ranges of timescales, as short

timescales require small time steps while long timescales require running many time steps. Similarly, large ranges of space scales present similar difficulties for the mesh size [4]. Finally, the PIC method requires significant memory and processor resources, and for the foreseeable future this will remain the case.

Geant4:

Geant4 is a C++ Monte Carlo code that models the interaction of particles with matter [5]. Geant is the acronym of GEometry ANd Tracking. The code is open source [6] and it is a simulations toolkit. Being a toolkit it means the developers provide classes to implement different processes and physics but it is up to the user to combine the necessary parts together to perform and customize the simulations. This provides a high degree of flexibility and it is the reason why Geant4 is used in many different areas: space, medicine [7], particle and nuclear physics [8].

Geant4 is a single particle tracker therefore it does not take into account space-charge effect. Recently the space-charge effects have been implemented in a program called G4beamline [9]. G4beamline is based on Geant4 toolkit however it loses some of the Geant4 capability. The major limitation is that at the present it does not simulate the performances of real-world detectors but implements “virtual” detectors.

Geant4 simulations results depend on the physical processes and the geometry implemented which needs to be carefully chosen and detailed. Moreover different models are available to describe the same process in different validity windows (i.e.

energy range). The user is required to understand first of all the physics that need to be implemented and then which model best suits the simulations requirements.

The physics and models implemented for the simulations performed in this thesis work are the following:

- Chapter 3 Timepix detector simulations and Chapter 4 bremsstrahlung radiation simulations:

Particles	Process	Model
Photons	<ul style="list-style-type: none"> - Photo-electric effect - Compton scattering - Pair production 	Standard Electromagnetic physics Validity range: >1 keV
Electron	<ul style="list-style-type: none"> - Multiple Scattering - Ionization - Bremsstrahlung 	
Positrons	<ul style="list-style-type: none"> - Multiple Scattering - Ionization - Bremsstrahlung - Annihilation 	

- Chapter 4: dose distribution simulations

Particles	Process	Model
Photons	<ul style="list-style-type: none"> - Photo-electric effect - Compton scattering - Pair production - Rayleigh scattering 	Low energy Livermore model. Validity range: 250 eV- 100 GeV
Electron	<ul style="list-style-type: none"> - Multiple scattering - Ionization - Bremsstrahlung 	
Positrons	<ul style="list-style-type: none"> - Multiple scattering - Ionization - Bremsstrahlung - Annihilation 	

References

1. Fonseca R.A., "Lectures Notes", *Comput. Sci.*, **2331**, 9 (2002)
2. Dawson J.M., "Particle simulation of plasmas", *Reviews of Modern Physics*, **55**(2), 403 (1983)
3. Available from: <http://plasmasim.physics.ucla.edu/codes>
4. Verboncoeur J.P., "Particle simulation of plasmas: review and advances", *Plasma Phys Contr F*, **47**(5A), A231 (2005)
5. Agostinelli S., *et al.*, "GEANT4-a Simulation Toolkit", *Nucl Instrum Meth A*, **506**(3), 250 (2003)
6. Available from: <http://geant4.cern.ch/>
7. Ivanchenko V.N., "Geant4: physics potential for instrumentation in space and medicine", *Nuclear Instruments and Methods in Physics Research Section A: Accelerators, Spectrometers, Detectors and Associated Equipment*, **525**(1–2), 402 (2004)
8. Moralles M., Guimarães C.C., Bonifácio D.A.B., Okuno E., Murata H.M., Bottaro M., Menezes M.O., and Guimarães V., "Applications of the Monte Carlo method in nuclear physics using the GEANT4 toolkit ", *AIP Conference Proceedings*, **1139**, 51 (2008)
9. Available from: <http://www.muonsinc.com/tiki-index.php?page=G4beamline>